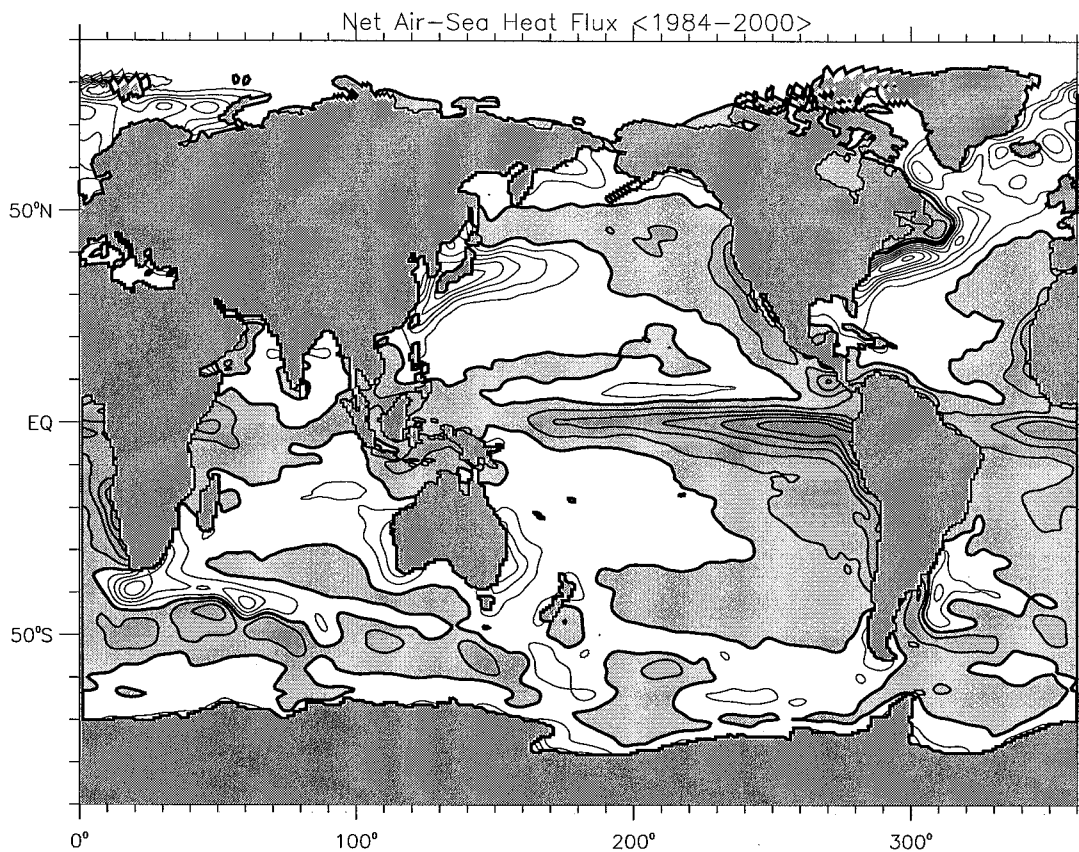May 2004

Diurnal to Decadal Global Forcing
For Ocean and Sea-Ice Models:
The Data Sets and Flux Climatologies

W. G. Large, S. G. Yeager

Net Air–Sea Heat Flux <1984–2000>

Diurnal to Decadal Global Forcing

For Ocean and Sea-Ice Models:

The Data Sets and Flux Climatologies

W. G. Large and S. G. Yeager

National Center for Atmospheric Research

P. O. Box 3000 Boulder, Colorado 80307

Contents

PREFACE

All aspects of the bulk forcing methodology are developed for two model config-
urations; a stand-alone Ocean General Circulation Model (OGCM) and an OGCM
coupled to a Sea-Ice Model (SIM). The air-sea and, for the latter, air-ice surface
boundary conditions are computed from the prognostic model surface temperatures,
combined with the specified near surface atmospheric state (wind, temperature and
humidity), downwelling radiation, precipitation and continental runoff. In the for-
mer, observed sea-ice concentration and specified ice-ocean fluxes effectively replace
the SIM, and eliminate the need for air-ice fluxes. In both cases, some restoring to
observed sea surface temperature and/or salinity is possible.

A complete collection of forcing data sets is chosen on the basis of global cov-
erage, spatial resolution, frequency duration and, to some extent, the needs and
behavior of the ocean and sea-ice components of the Communty Climate System
Model. The global NCEP/NCAR reanalysis gives the atmospheric state, the recent
ISCCP-FP product provides the radiation fields, the precipitation is a blend of mul-
tiple products, the continental runoff is derived from continental water budgets and
climatological river discharge, the sea-ice concentration comes from the National
Snow and Ice Data Center, historical SST is a reconstruction that has been made
compatible with sea-ice concentration, and ocean salinity is non-standard at high
latitudes. Other data sets are used to determine objective corrections to the forcing
data sets, with the major factors a general increase in the wind speed, a reduction
in the near surface humidity and a reduction in the solar insolation between $60°S$
and $40°N$. Further adjustments to high latitude air-temperatures and downwelling
longwave radiation are needed to improve water mass formation and sea-ice simula-
tions. The corrected/adjusted forcing is used in conjunction with observed SST to
produce an observationally based air-sea flux climatology over 43 years. A neces-
sary achievement of the exercise is to lower the global air-sea heat flux over 17 years

(1984–2000) from $31W/m^2$ heating to a more reasonable $1W/m^2$. A freshwater imbalance of $3.4mg/s/m^2$ is overcompensated by increased evaporation, so an overall increase in precipitation is used to give a nearly balanced $(-0.1mg/s/m^2)$ global mean budget.

The products based on 17 year mean fluxes include, global maps of the climatological heat, freshwater and momentum (wind stress) fluxes and their components, zonal averages of the fluxes and flux components, the implied northward transports of heat and freshwater in each ocean basin. The climatological seasonal cycle is examined with the first and second annual harmonics of net heat flux, net freshwater flux, zonal wind stress, and meridional wind stress. Annual mean fluxes are zonally averaged over the three ocean basins in order to display interannual variability over 43 years (1958–2000), which is then related to the observed variability of several large scale climate indices. Global and basin averages of annual average heat flux reveal decadal variability, with persistently warming heat fluxes from about 1975 to 1990, and numerous cooling years both before and after.

Finally, as an alternative to forcing with a full 43 year cycle and its interannual variability, a "Normal" Year Forcing (NYF) is developed. It consists of single annual cycles of all the data needed to force an OGCM and SIM. For a given SST it produces comparable fluxes as the full cycle, provided the same corrections are applied. NYF is constructed so that it can be repeated over and over without initiating spurious transients, while still retaining seasonal and propagating synoptic (weather) variability.

1 Introduction

Integration of a either a global Ocean General Circulation Model (OGCM), or an OGCM coupled to a Sea-Ice Model (SIM), places rigorous demands on the forcing data sets, not all of which can be entirely met. Foremost, is the need for global coverage, including the poorly sampled Southern Ocean and ice covered polar seas. Also, the forcing should vary across the important ocean timescales; from the 12-hour polar inertial period, to the decadal. Between these timescales are the diurnal solar cycle, the three to seven day synoptic cycle, the 30 to 60 day intra-seasonal oscillation, the twelve-month seasonal cycle, and the 2 - 10 year inter-annual ENSO (El Nino - Southern Oscillation) variability. Finally there are accuracy requirements, which are the most difficult to quantify and satisfy. Perhaps the most important consideration is that global, long term heat and freshwater fluxes into the ocean should both be near zero. Observations of long-term changes in ocean heat content suggest a heat flux of at most a few W/m^2. For example, Levitus et al. (2000) find that the temperature of the world's oceans increased from the 1950s to the 1990s at a rate equivalent to a surface heat flux imbalance of only $0.3W/m^2$. Similarly, the global ocean salinity record doesn't support a significantly non-zero global long-term freshwater flux.

In ocean modeling a common practice has been to restore, or relax surface temperature and salinity to observed values (Cox & Bryan 1984), which strongly limits errors in surface properties, but at the expense of very erroneous surface fluxes (Killworth et al. 2000), especially of freshwater (Large et al. 1997). Conversely, forcing with observed fluxes has resulted in poor representations of surface temperature and salinity (Rosati & Miyakoda 1988). The two approaches can be combined so that relaxation terms are added to prescribed heat and salt fluxes (Barnier et al. 1995). However, Nurser et al. (1999) find that the restoring term substantially modifies the

surface density flux of a North Atlantic model.

Here we continue the development of bulk forcing; an alternative, more physical approach. It follows Large et al. (1997), and an intermediate stage is described in Large & Nurser (2001). The methodology should be applicable to a wide range of models, even though our primary requirements are set by the ocean and sea-ice components of the Community Climate System Model (Kiehl & Gent 2004). Important features include the coupling of the heat and freshwater fluxes through the evaporation and latent heat flux, and the use of prognostic model sea surface temperature (SST) in the heat flux computation (Section 2). The latter provides a strong negative feedback to the warming/cooling of the ocean in a physical manner, however the fluxes become dependent on the model solution. A potential problem when forcing ocean models is that there is no similar physical feedback to retard drifts in surface salinity, so a weak restoring to observed salinity may sometimes be needed. Improvements to the forcing are possible because of new data sets. Some of these (Section 4) are used directly to improve the flux computations. Others, are not global and/ or too short for forcing OGCMs, but provide a means of more objectively determining corrections to the longer, global data sets that are used (Section 5).

The forcing of OGCMs is complicated by the presence of sea-ice at polar latitudes. Not only are ice-ocean fluxes (Section 2.2) needed, but the freezing of seawater also needs to be accounted for. An attractive, but complicated approach is to numerically couple the OGCM to a SIM, so that ice-ocean fluxes are explicitly computed and exchanged as part of the coupling. However, it is then necessary to force the SIM with air-ice fluxes of heat, freshwater and momentum (Section 3). This option places very high demands on flux accuracies, because of positive feedbacks associated with sea-ice. For example, the higher albedos expected if there is too much snow and ice would tend to reduce solar heating, which would lead to even

2

more ice and snow and even higher albedos. A simpler procedure is just to specify ice-ocean fluxes, which although not well known, apply to only a small fraction of the global ocean ($< 10\%$) and, at least in the case of the heat flux, are thought to be small.

With any set of forcing functions, it is possible to compute the surface air-sea fluxes using observed, rather than model prognostic, SST. The result is an observationally based global air-sea flux climatology (Section 6), that at least satisfies global constraints. It is used to examine the mean seasonal cycles of fluxes (Section 7) as well as some aspects of variability on interannual and longer timescales (Section 8). The differences between these "observed" fluxes and the fluxes from a model integration represent the effects of model SSTs that inevitably drift away from the observed temperatures due to a combination of model and forcing error. These effects are one-way in that they do not change the atmospheric forcing functions, as would be the case with two-way interaction in a fully coupled climate model. For many purposes it is very useful to compare these "observed" air-sea fluxes to existing climatologies. A number of these are intercompared by Beranger et al. (1999); including SOC (Southhampton Oceanography Centre; Josey et al. (1998)), COADS (University of Wisconsin-Milwaukee version of the Cooperative Ocean Atmosphere Data Set; (Silva et al. 1994)), NCEP (NCEP/NCAR reanalysis fluxes; Kalnay et al. (1996)) and ERA-15 (15 year ECMWF reanalysis fluxes, (Gibson et al. 1997)). Others can be found in Taylor(ed.) (2000). Unfortunately, the necessary ice data (eg. surface temperatures) are not available to similarly compute companion air-ice and ice-ocean flux climatologies.

2 Ocean Surface Fluxes

Forcing an OGCM amounts to specifying surface boundary conditions for the vertical diffusion terms of a model's prognostic equations for potential temperature, θ, salinity, S, and the orthogonal horizontal velocity components, u (zonal) and v (meridional). The respective boundary conditions are the surface kinematic fluxes of heat $< w\theta >_o$, salt, $< ws >_o$, and momentum $< wu >_o$ and $< wv >_o$, which are related to the surface fluxes of heat, Q, freshwater, F and momentum $\vec{\tau} = (\tau_u, \tau_v)$ through

$$< w\theta >_o = Q \, (\rho C_p)^{-1} \qquad (1a)$$

$$< ws >_o = F \, (\rho^{-1} S_o) \qquad (1b)$$

$$(< wu >_o, < wv >_o) = \vec{\tau} \, \rho^{-1} = (\tau_u, \tau_v) \, \rho^{-1} \qquad (1c)$$

where ρ is ocean density ($\approx 1027 \, \mathrm{kg/m3}$), C_p is ocean heat capacity ($\approx 4000 \, \mathrm{j/kg/K}$) and S_o is a reference ocean salinity. A constant $S_o \approx 35$ PSU is used in the virtual salt flux formulation (1b) to ensure that a freshwater loss followed by an equivalent gain results in no net change in ocean salinity. The resulting pathology is that rainfall onto freshwater produces a negative salinity to balance the increased salinity where the water vapor originally evaporated. This is not an issue in OGCMs configured to receive a true water flux (eg. in a fully prognostic free surface formulation). In either case, the surface forcing problem is transformed into one of specifying the global distribution of the surface fluxes. Additional forcing due to atmospheric pressure loading is a byproduct of bulk forcing (Section 4), while that due to tides is not considered here.

Nearly all aspects of the extensive and complicated subject of surface fluxes are comprehensively examined by the WCRP/SCOR Working Group on Air-Sea Fluxes (Taylor(ed.) 2000). Direct measurements of all the fluxes are difficult, expensive, and hence much too rare for forcing OGCMs. However, many of these measurements

4

have been used to develop bulk formulae through which the fluxes can be estimated more frequently and globally from more readily available data. Attempts have been made to develop algorithms and techniques to produce surface fluxes directly from satellite observations, and these have been most successful at estimating the radiative heat fluxes, precipitation and the wind stress. In the case of the latter and turbulent heat fluxes, satellite data are first converted to the intermediate parameters required by the bulk formulae, but not everything is amenable to remote sensing across the global oceans (Taylor(ed.) 2000). Therefore, we use different data sets for different components of the overall problem. Our choices reflect the above priorities of global coverage spanning a broad range of time scales. Other justifiable choices could have been made and most are discussed at length in Taylor(ed.) (2000).

In general a fraction, f_i, of an OGCM grid point can be covered by sea-ice, leaving a fraction, $f_o = 1 - f_i$, exposed to the atmosphere above. The ocean surface fluxes are, therefore, given by

$$Q = f_i \, Q_{io} + f_o \, Q_{as} \tag{2a}$$

$$F = f_i \, F_{io} + f_o \, F_{as} + R \tag{2b}$$

$$\vec{\tau} = f_i \, \vec{\tau}_{io} + f_o \, \vec{\tau}_{as} \tag{2c}$$

where the subcripts "as" and "io" denote air-sea and ice-ocean fluxes, respectively. Globally less than 10% of the ocean surface is covered by sea-ice, so Q_{io} and F_{io} contribute little to the global balances of heat and freshwater. In (2b), R is the continental runoff which can be specified as a positive water flux over the near shore ocean surface, regardless of ice cover.

2.1 Air-Sea Fluxes

The air-sea heat and freshwater fluxes are computed by summing estimates of their components, namely;

$$Q_{as} = Q_S + Q_L + Q_E + Q_H + Q_P \qquad (3a)$$

$$F_{as} = P + E \qquad (3b)$$

where all the fluxes and their components are defined to be positive down, such that fluxes, including momentum, into the ocean are positive. The heat flux has both radiative and turbulent components. The short wave, or solar radiation, Q_S, includes wavelengths between 0.3 and 3μ and is always positive. Longer wavelengths, up to 50μ, comprise the longwave radiation, Q_L, that is generally negative because the upwelling radiation from the surface is usually greater than the downwelling from the colder clear sky and clouds. The turbulent heat fluxes are the sensible, Q_H, and the latent, Q_E. The latter is directly related to the evaporative component of the freshwater flux, E, and both Q_E and E are usually negative. Positive values have been observed in the rare circumstances of very warm moist air over a cold sea. Precipitation, P, over the ocean is positive definite and accounts for about 90% of the evaporation from the ocean (Taylor(ed.) 2000), so continental runoff is neither negligible, nor a major term in the global balance (2b). The melting of frozen precipitation (snow) that falls onto the ocean surface leads to a negative precipitation heat flux, $Q_P < 0$, which can also include the temperature difference between precipitation and SST. The wind stress is also a turbulent flux which almost always has a component aligned with the ocean surface current, $\vec{U}_0$, so that kinetic energy $(\vec{\tau} \cdot \vec{U}_0)$ is usually transferred from the atmosphere to the ocean.

- Turbulent Fluxes : The turbulent fluxes can be estimated from bulk formulae (Roll 1965):

$$E = \rho_a \, C_E \, (q(z_q) - q_{sat}(SST)) \, |\Delta \vec{U}| \qquad (4a)$$

$$Q_E = \Lambda_v \, E \tag{4b}$$

$$Q_H = \rho_a \, c_p \, C_H \, (\theta(z_\theta) - SST) \, |\Delta \vec{U}| \tag{4c}$$

$$\vec{\tau} = \rho_a C_D |\,\Delta \vec{U}|\, \Delta \vec{U}, \tag{4d}$$

where $\Delta \vec{U} = \vec{U}(z_u) - \vec{U}_0$ is the vector difference between the wind at height z_u and the surface current, although the current is often neglected. The potential air temperature, $\theta(z_\theta)$, and specific humidity, $q(z_q)$, may be from different heights, z_θ and z_q, respectively. In (4), $\rho_a \approx 1.22 kg/m^3$ is a near surface air density that is defined more precisely in Section 4.1, $c_p \approx 1000.5 J/kg/K$ is the specific heat of the air, $\Lambda_v \approx 2.5 \times 10^6 J/kg$ is the latent heat of vaporization and SST is the sea surface temperature. The air at the surface is assumed to be saturated, with a specific humidity given by

$$q_{sat}(q_1, q_2, SST) = \rho_a^{-1} \, q_1 \, e^{(q_2/SST)}, \tag{5}$$

where the coefficents are $q_1 = 0.98 \times 640380 kg/m^3$ and $q_2 = -5107.4 K$ and the factor 0.98 applies only over sea-water. More accurate expressions than (5) are available, but not necessary given the uncertainties in the 0.98 factor, C_E and the saturation assumption, for example. Similarly, the order 1% effects of temperature on Λ_v and of humidity on c_p are ignored.

The drag coefficient, C_D and the transfer coefficents for evaporation, C_E, and sensible heat, C_H, are functions of height, atmospheric stability, ζ, and wind speed. Their neutral stability, 10m values are given by

$$1000 \, C_D = \frac{2.70(m/s)}{U_N(10m)} + .142 + \frac{U_N(10m)}{13.09(m/s)} \tag{6a}$$

$$1000 \, C_E = 34.6 \, \sqrt{C_D} \tag{6b}$$

$$1000 \, C_H = 18.0 \, \sqrt{C_D} \, , \qquad \textit{stable} \ \zeta > 0 \tag{6c}$$

$$= 32.7 \, \sqrt{C_D} \, , \qquad \textit{unstable} \ \zeta \le 0 \tag{6d}$$

7

and are plotted in Fig. 1 as a function of $U_N(10m)$, the equivalent neutral 10m wind speed relative to the surface current. The C_D formulation comes from a compilation of observations from 1m/s to more than 25m/s (E.E. Vera, unpublished manuscript, 1983), and its infinite value at zero wind is consistent with the theoretical behavior of wind over a smooth plate. The dependence of C_E and C_H on the square root of C_D is also theoretical, while the stability dependence of C_H is observed. Taylor(ed.) (2000) presents a number of alternative choices for these transfer coefficients.

The bulk formulae effectively transform the problem of specifying the turbulent surface fluxes into one of describing the near surface atmospheric state (wind, temperature and humidity). In forcing OGCMs, the SST and surface current are taken to be the prognostic upper layer temperature and velocity, respectively. If instead some measure of skin temperature is used, then these coefficients would not be approporiate, because the formulations (6) are fits to measurements using a bulk water temperature a meter or more beneath the surface. Three of the ways of computing the fluxes are: A) shift the wind, temperature and humidity to 10m and neutral stability so that neutral 10m coefficients can be used directly, B) shift the coefficients to the height, and stability of the atmospheric state variables. and C) shift the temperature and humidity to the height of the wind, z_u, then shift the coefficients to this height and to the atmospheric stability. In general, we choose (C). But, when the atmospheric state variables are given at the same height, as for example when there is a coupled atmopheric model configuration, (C) becomes equivalent to a particularly efficient version of (B). This efficiency can also be achieved by shifting the temperature and humidity to the wind height offline. The calculations are most efficient when the wind height, z_u, equals the 10m reference height of the transfer coefficients.

The iterative procedure for (C) is as follows: 1) Compute the virtual potential temperature, $\theta_v = \theta(z_\theta)(1. + .608q(z_q))$, where the factor .608 is the ratio of the

molecular weights of dry air and water vapor minus one. Then make a first guess of neutral stability and $U_N(10m) = |\Delta \vec{U}|$ to give the transfer coefficients from (6). The initial turbulent scales are then computed as:

$$u^* = \sqrt{\rho_a^{-1} \ |\vec{\tau}|} = \sqrt{C_D} \ |\Delta \vec{U}| \tag{7a}$$

$$t^* = \frac{Q_H}{\rho_a \ c_p \ u^*} = \frac{C_H}{\sqrt{C_D}} \ [\theta(z_\theta) - SST] \tag{7b}$$

$$q^* = \frac{E}{\rho_a u^*} = \frac{C_E}{\sqrt{C_D}} \ [q(z_q) - q_{sat}(q_1, q_2, SST)] \tag{7c}$$

2) Begin the iteration loop with estimates of the stability parameters $\zeta_u = z_u/L$, $\zeta_q = z_q/L$ and $\zeta_\theta = z_\theta/L$, where L is the Monin-Obukhov length. For each of the these, find the integrals of the dimensionless flux profiles of momentum, $\psi_m(\zeta)$, and of heat and moisture, $\psi_h(\zeta)$, which involve the von Karman constant $\kappa = 0.4$, and gravitational acceleration, g :

$$\zeta(z) = \frac{\kappa \ g \ z}{u^{*2}} [\frac{t^*}{\theta_v} + \frac{q^*}{(q(z_q) + 0.608^{-1})}] \tag{8a}$$

$$X = (1 - 16 \ \zeta)^{1/4} \tag{8b}$$

$$\psi_m(\zeta) = \psi_h(\zeta) = -5 \ \zeta, \qquad stable, \ \ \zeta \geq 0 \tag{8c}$$

$$\psi_m(\zeta) = 2 \ ln(\frac{1+X}{2}) + ln(\frac{1+X^2}{2}) - 2 \ tan^{-1}(X) + \frac{\pi}{2} \qquad unstable, \ \ \zeta < 0 \tag{8d}$$

$$\psi_h(\zeta) = 2 \ ln(\frac{1+X^2}{2}) \qquad unstable, \ \ \zeta < 0 \tag{8e}$$

3) Shift the wind speed to $10m$ and neutral stability, and the temperature and humidity to the wind height :

$$U_N(10m) = |\Delta \vec{U}| \ (1 + \frac{\sqrt{C_D}}{\kappa}[ln(z_u/10m) - \psi_m(\zeta_u)] \ )^{-1} \tag{9a}$$

$$\theta(z_u) = \theta(z_\theta) - \frac{\theta^*}{\kappa} \ [ln(\frac{z_\theta}{z_u}) + \psi_h(\zeta_u) - \psi_h(\zeta_\theta)] \tag{9b}$$

$$q(z_u) = q(z_q) - \frac{q^*}{\kappa} \ [ln(\frac{z_q}{z_u}) + \psi_h(\zeta_u) - \psi_h(\zeta_q)] \ . \tag{9c}$$

9

4) Update the neutral 10m transfer coefficients from (6), then shift them to the measurement height, z_u, and stability, ζ_u, using:

$$C_D(z_u, \zeta) = C_D(1 + \frac{\sqrt{C_D}}{\kappa} [ln(z_u/10m) - \psi_m(\zeta_u)])^{-2} \qquad (10a)$$

$$C_H(z_u, \zeta) = C_H \sqrt{\frac{C_D(z_u, \zeta)}{C_D}} (1 + \frac{C_H}{\kappa \sqrt{C_D}} [ln(z_u/10m) - \psi_h(\zeta_u)])^{-1} \qquad (10b)$$

$$C_E(z_u, \zeta) = C_E \sqrt{\frac{C_D(z_u, \zeta)}{C_D}} (1 + \frac{C_E}{\kappa \sqrt{C_D}} [ln(z_u/10m) - \psi_h(\zeta_u)])^{-1} \qquad (10c)$$

5) Using these transfer coefficients (10), and $\theta(z_u)$ and $q(z_u)$ from (9), recompute the virtual potential temperature, θ_v, and update the turbulent scales in (7). Then start the next iteration loop at step (2) above.

Over the ocean stability is usually near neutral, and 2 iterations are all that is necessary. Over sea-ice the atmosphere can be very stable and up to five iterations may be needed. After the last iteration the fluxes are computed from the last set of turbulence scales according to (7), which is just another form of (4).

- Radiative Heat Fluxes : The short-wave solar radiation that passes through the bottom of the atmosphere is the insolation, Q_I, incident on the surface below, and the surface albedo (α) is the fraction that is reflected back to the atmosphere. About 40% of this insolation is diffuse, with an albedo $\alpha_{df} = 0.06$ (Payne 1972). The albedo for the remaining direct solar radiation is higher and increases with the solar zenith angle, so that a reasonable approximation is to assume a constant $\alpha_{dr} = 0.07$. The solar energy transferred to the ocean is then given by

$$Q_S = Q_I [0.6 (1 - \alpha_{dr}) + 0.4 (1 - \alpha_{df})] = Q_I (1 - \alpha), \qquad (11)$$

with $\alpha = 0.066$.

At the temperature of the ocean surface and of the atmosphere above, blackbody radiation occurs at long wavelengths. The heat flux associated with the ocean surface

radiation is negative, because the ocean loses heat, and is given by $(-\epsilon\sigma(SST)^4$), where $\sigma = 5.67 \times 10^{-8} W/m^2/K^4$ is the Stefan-Boltzmann constant and ϵ is the surface emissivity. The ocean also receives longwave energy from the atmosphere Q_A, so that the net longwave flux is given by

$$Q_L = Q_A - \sigma\ (SST)^4 \tag{12}$$

where the emissivity is taken to be 1.0 to account for the small reflected fraction of Q_A (Lind & Katsaros 1986).

The radiative flux problem is thus reduced to one of specifying both the solar insolation, Q_I, and the downwelling longwave flux from the atmosphere, Q_A. Fortunately, both these fluxes have been derived from satellite observations over the ocean (Section 4), so that there is no need to use empirical formulae, such as those developed by Smith & Dobson (1984) and examined by Fung et al. (1984), respectively. Nonetheless, these expressions do show the first order effect of clouds on these fluxes. The presence of clouds decreases Q_I, but increases Q_A. Thus, there is a compensating effect on the total surface heat flux that can be nearly complete in some situations. Therefore, it is important to use consistent data sets for both radiation components, so that cloud errors are mimimized.

- Precipitation : The in situ measurement of marine precipitation is difficult (Knox 1991). Obtaining precipitation data for forcing OGCMs is further complicated by very serious sampling issues arising from its intermittency in both time and space. The sampling problem is less problematic in satellite derived estimates, but the lack of accurate in situ observations makes the development and validation of algorithms difficult. Therefore, as will be demonstrated in Section 4, available precipitation data sets must be regarded as highly uncertain. Also, problematic is the partitioning of precipitation into liquid, P_R (rain), and frozen, P_S (snow), because most data sets

11

just give the total,

$$P = P_R + P_S.$$ (13)

In such cases the precipitation is taken to be rain whenever the corresponding near surface air temperature is greater than a threshold value, $T_p = 0°C$. At colder air temperatures it is regarded as snow, which is then "melted" by cooling the surface ocean with a negative precipitation heat flux

$$Q_P = -\Lambda_f P_S,$$ (14)

where $\Lambda_f = 3.337 \times 10^5 j/kg$ is the latent heat of fusion.

- Runoff : Although globally a much smaller term than either precipitation or evaporation, runoff is concentrated near coastlines, especially at the mouths of large rivers, where it is responsible for low salinity surface waters, especially in the Arctic. We seek to capture this spatial distribution for our OGCM forcing, but a representation of wet/dry seasonality and the storage of snowfall over land may be more detail than is warranted. There are runoff data for approximately the largest 1000 of the world's rivers, but these gauged rivers account for only about 40 to 60% of the runoff from most continents, and none of the runoff from Antarctica. The remainder enters the ocean as ground water seepage, or in ungauged surface runoff. Therefore, it is necessary to have estimates of the net excess of precipitation over evaporation from each of the continents, and to distribute this excess as runoff into the bordering ocean basins (Section 4).

2.2 Ice-Ocean Fluxes

A comprehensive review of ice-ocean coupling is provided by Schmidt et al. (2004). Over much of the ice pack, especially in the Southern Ocean, the force balance of sea-ice is primarily between wind stress and ocean drag, which is referred to as free

drift. OGCMs are, therefore, forced reasonably well by assuming that the air-ice stress, $\vec{\tau}_{ai}$ (Section 3) passes unchanged to the ocean:

$$\vec{\tau}_{io} = \vec{\tau}_{ai} \tag{15}$$

In general the ocean gains heat and salt where ice is formed and is cooled and diluted where the ice melts. The heat and salt fluxes are given by :

$$Q_{io} = Q_M + Q_F + Q_B + Q_{PS} \tag{16a}$$

$$F_{io} = F_M + F_F + F_B. \tag{16b}$$

The fluxes associated with the melting of both sea-ice and accumulated snow are a cooling melt flux $Q_M < 0$ and positive freshwater flux $F_M > 0$. Solar radiation is able to penetrate thin ice to become an ocean surface flux, Q_{PS}, but any snow with its high albedo, or thick ice will make this term very small. The usually cold atmosphere above the ice produces basal ice and a freshwater flux, $F_B < 0$, from the ocean. The corresponding ocean surface heat flux, Q_B, is usually near zero, because the basal cooling is balanced by the latent heat of fusion of the basal ice. Direct air-sea cooling of the ocean allows the possibility for ocean temperatures to fall below freezing, T_f. The physical process that relieves this unphysical condition is the formation of frazil sea-ice. A heat flux $Q_F > 0$ effectively restores the ocean temperature to the freezing point. Most of the salt is left behind and is represented by a negative freshwater flux, $F_F < 0$. Frazil ice formation can be a dominant process along the coast of Antarctica where offshore winds can keep significant portions of the ocean surface ice-free.

Unfortunately, the data sets and bulk formulae that would allow all these exchanges to be specified as forcing for an OGCM do not exist. However, both Q_{io} and F_{io} can simply be specified, based on the output of some sea-ice model, or on budget estimates of ice packs.

13

Another simple approach is to revert back to restoring boundary conditions under sea-ice. Here the heat and salt fluxes are given by :

$$Q_{io} = C_Q \left(SST_o - T_1 \right) \tag{17a}$$

$$F_{io} = C_F \left(S_1 - SSS_o \right), \tag{17b}$$

where SST_o and SSS_o are observed sea surface temperature and salinity, respectively, and T_1 and S_1 are the model prognostic temperature and salinity of the upper model layer. Undesirable features of this forcing include the decoupling of the heat and freshwater fluxes, and the arbitrary restoring coefficients C_Q and C_F, which are chosen to relax model values back to observed on time scales ranging from days to years, and the paucity of observations especially of SSS_o in winter around Antarctica. The effective restoring of ocean grid points is given by f_i times these coefficients (2), so the relaxation becomes weaker as the ice fraction decreases.

An alternative approach uses ice melt and frazil ice formation to keep upper ocean temperatures near freezing in the presence of sea-ice ($f_i > 0$), with corresponding freshwater fluxes changing salinity. The frazil fluxes are computed within the ocean model. The heat flux required to raise the temperature, T_1, of the uppermost layer of thickness, Δ_1, to the freezing point in a timestep, Δt, is

$$Q_F = \rho \, C_p \left(T_f - T_1 \right) \Delta_1 \, \Delta t^{-1}. \tag{18}$$

The corresponding frazil ice formation in terms of a negative freshwater flux is

$$F_F = -Q_F \, \Lambda_f^{-1}. \tag{19}$$

In practice, it is simplest to warm the ocean back to freezing while increasing the surface salinity by an appropriate amount. The frazil ice can then be regarded as forming part of the local ice concentration, or as being advected away, depending on

14

the observed f_i. In warm ocean conditions $(T_1 > T_f)$ melt fluxes can be computed as

$$Q_M = f_i \, Q_F \ < 0 \tag{18a}$$

$$F_M = -Q_M \, \Lambda_f^{-1}. \tag{18b}$$

In the presence of sea-ice $(f_i > 0)$, Q_M represents the melt needed to cool the upper layer under the sea-ice back to the freezing point. These Q_F and Q_M terms represent a very effective restoring to freezing, with a physical coupling to the freshwater fluxes that do not necessarily restore the salinity. Therefore, the basal and penetrating shortwave fluxes can be neglected, even though they could be prescribed, from the output of a coupled ocean-ice model for example. Note that a complication arises if the model forms frazil ice where the observed concentration is zero. Since this should not be common, any reasonable solution is acceptable.

3   Air-Ice Fluxes

Coupling an OGCM to a sea-ice model eliminates the need to specify or compute any ice-ocean fluxes (Section 2.2), or sea-ice fraction, but requires data sets for computing all the air-ice fluxes. It also means that errors in these fluxes and defficiencies in the ocean and ice models will project in unpredictable ways onto the ice-ocean fluxes, and hence the ocean model solution. Nevertheless, such coupling is often a desirable choice, especially when a goal is to open up degrees of freedom to allow the generation of more realistic variability.

In general a sea-ice model has a number of ice categories. The air-ice heat and water fluxes for a particular ice category, n, are given by

$$Q_{ai}^n = Q_S^n + Q_L^n + Q_E^n + Q_H^n \tag{19a}$$

$$F_{ai}^n = P^n + E^n \tag{19b}$$

Ice models differentiate between snow and rain. The former becomes P^n in (19b), which accumulates in the snow layer atop ice category, n, while the rain is passed directly to the ocean below, as a contribution to F_{io} in (2b).

The turbulent fluxes are again computed from bulk formulae, but separate calculations are performed for each ice category, n. Using each category's ice/snow surface temperature, T_S^n, the turbulent fluxes can be computed from the same data sets as the air-sea fluxes (Section 2), namely; $\theta(z_\theta), q(z_q), \vec{U}(z_u)$:

$$E^n = \rho_a \; C_E^* \; (q(z_q) - q_{sat}^*(T_S^n)) \; |\vec{U}(z_u)| \tag{20a}$$

$$Q_E^n = \Lambda_s \; E^n \tag{20b}$$

$$Q_H^n = \rho_a \; c_p \; C_H^* \; (\theta(z_\theta) - T_S^n) \; |\vec{U}(z_u)| \tag{20c}$$

$$\vec{\tau}_{ai} = \rho_a \; C_D^* \; \vec{U}(z_u) \; |\vec{U}(z_u)|. \tag{20d}$$

Here, $\Lambda_s = \Lambda_v + \Lambda_f \approx 2.839 \times 10^6 J/kg$ is the latent heat of sublimation and the ice velocity is assumed to be much slower than the wind, and is neglected. Over snow and ice the coefficients of the q_{sat} function (5) are $q_1 = 11637800 kg/m^3$ and $q_2 = -5897.8K$. Unlike the ocean, the neutral 10m ice-ocean transfer coefficients are equal and constant

$$C_E^* = C_H^* = C_D^* = 1.63 \times 10^{-3}. \tag{21}$$

Given a shortwave insolation data set, ice models typically split this radiation into four components; visible (wavelengths from 0.3 to 0.7μ) direct, visible diffuse, near-infrared (0.7 to 3μ) direct and near-infrared diffuse. An ice model then must provide the respective albedos; α_{Vdr}^n, α_{Vdf}^n, α_{Ndr}^n and α_{Ndf}^n, for each ice category, n. In order to use Q_I data the respective fractions are needed, with .29, .24, .31, .16 an acceptable partitioning that is consistent with (11) :

$$Q_S^n = Q_I \; [.29(1 - \alpha_{Vdr}^n) + .31(1 - \alpha_{Vdf}^n) + .24(1 - \alpha_{Ndr}^n) + .16(1 - \alpha_{Ndf}^n)]. \tag{22}$$

It is less complicated to utilize downwelling long-wave radiation, because there is no need to do any partitioning. The net long-wave radiation is just :

$$Q_L^n = \epsilon_i \, Q_A - \epsilon_i \sigma (T_S^n)^4, \tag{23}$$

where $\epsilon_i = 0.95$, is the ice/snow emissivity. This emissivity is also used in the first term on the right-hand-side of (23) as 1 minus a longwave albedo.

4   Global Forcing Datasets

4.1   Atmospheric State

The turbulent air-sea and air-ice fluxes are based on atmospheric state data from the global NCEP/NCAR reanalysis, which extends from 1948 through 2002 (Kalnay et al. 1996). This 53 year period is the longest of any of our forcing data sets (Fig. 2) and has no gaps. The most important data are the atmospheric fields of near surface wind $\vec{U}(10m)$, temperature ($\approx$ potential temperature $= \theta(2m)$) and specific humidity $q(2m)$. Sea level pressure, SLP, is also used, but a constant $SLP = 100kPa$ would often suffice. These fields are available at 6 hour intervals on a T62 (209km) horizontal grid. The potential temperature and specific humidity are shifted according to (9) from the reanalysis height of 2m to match the wind height: $z_u = z_\theta = z_q = 10m$ in (4). The air density is then computed as:

$$\rho_a = \frac{SLP}{R_{gas} \, \theta(z_\theta) \, (1. + .608 \, q(z_q))}, \tag{24}$$

where $R_{gas} = 287.04 J/kg/K$ is the gas constant for dry air. A constant $\rho_a \approx 1.22 kg/m^3$ would be adequate for many purposes.

These atmospheric state variables $\vec{U}(10m)$, $\theta(10m)$, $q(10m)$, ρ_a when combined with a sea surface temperature in the iterative procedure of Section 2.2 are sufficient to calculate the air-sea turbulent fluxes(4). When they are combined with ice/snow

surface temperatures (T_s^n), a similar iterative procedure yields the air-ice turbulent fluxes (20), for each ice category, n.

4.2 Radiation

Recent ISCCP (International Satellite Cloud Climatology Project) global radiative flux data products have been created by integrating the NASA Goddard Institute for Space Studies climate GCM radiative transfer model with a collection of global atmospheric datasets, including ISCCP cloud and surface properties (Zhang et al. 2004). Most importantly, this ISCPP-FP data set provides fields of short-wave insolation, Q_I and downwelling long-wave radiation, Q_A, required by equations (11) and (12) to compute the air-sea radiative fluxes. The calculation of air-ice radiative fluxes is more complicated, because in addition to these fields, equations (22) and (23) also require four albedos and the surface temperature for each ice thickness category.

Since the Q_I and Q_A fields have been derived in concert from the same input they should derive full advantage of any cancellation of cloud error. In addition, reflected short-wave and outgoing surface long-wave radiation are also provided, but these will not, in general, be consistent with our calculations depending on the surface temperatures and on the distribution of ocean, ice and land within each grid box. The data resolution is 3-hourly on a 2.5 deg latitude-longitude grid, but it is difficult to properly remap the diurnal cycle. Therefore, for our purposes, the data are averaged into both daily and monthly means, then mapped to the NCEP reanalysis T62 grid for compatibility with the atmospheric state data. The data set is ongoing from mid-1983, and while it is more than than twice as long as previous ISCCP products we have used to force OGCMs, (eg. Bishop & Rossow (1991)), the radiation flux time series is still the shortest of the forcing dataset collection (Fig.

18

2). In order to force a model over more of the reanalysis period, the radiation data
are extended back in time using the climatological annual cycle of monthly/daily
means derived from the available dataset. However, an OGCM forced in this way
will necessarily lack variability associated with any modulations of the radiation
prior to mid-1983.

4.3 Precipitation

Freshwater fluxes change sea surface salinity (1b), but because these fluxes (2b)
do not depend on the salinity, there is no direct negative feedback to retard the
accululation of flux error, as there is in the case of the heat flux dependance on
SST (4b, 4c, 12). Therefore, the large uncertainties in precipitation estimates are
particularly problematic. The comparison of zonal averages from four precipitation
data sets in Fig. 3 illustrates the problem, even though large regional differences
are lost, because of compensatating differences along latitude circles. There is good
agreement in all four data sets only around 30° latitude in both hemispheres. Ideally,
one data set would be applicable globally, but this does not appear to be a practical
option. Therefore, we choose different precipitation forcing in each of five zones; the
Antarctic (poleward of $65°S$), the Southern (between $65°S$ and $30°S$), the Equatorial
(between $30°S$ and $30°N$), the Northern , and the Arctic (poleward of $70°N$).

Several available precipitation data sets do not meet the requirements of global
coverage, spanning at least a decade with monthly or higher frequency. Nonethe-
less, these data sets are useful for comparison purposes and perhaps regional ap-
plication. The SOC data (Josey et al. 1998) is a ship based monthly climatology,
with inadequate sampling particularly in the southern hemisphere and Arctic. The
MSU satellite dataset was constructed purely from Microwave Sounding Unit data
(Spencer 1993). Its major drawbacks are the lack of data poleward of about 55°

and the short record, 1983-1991. Similarly, data from the Tropical Rainfall Measuring Mission (TRMM, not shown) started in late 1997 and is confined to within about 40° of the equator. There is also the "Serreze" monthly Arctic data set that combines the climatology used by Serreze & Hurst (2000) and the gauge-corrected (Yang 1999) monthly precipitation over the Arctic Ocean from the Russian North Pole drifting station and a larger set of coastal stations. The climatology covers latitudes north of $50°N$ from 1979 through 2000.

Two particular data sets better satisfy our ocean forcing requirements. The Xie & Arkin (1996) data set is the product of a merging algorithm which combines satellite observations, gauge measurements and model predictions. The result is a continuous, global record on a 2.5 degree grid since 1979, that we have used to force OGCMs. Unfortunately, this experience has shown that the model solutions become much too fresh in the western tropical Pacific (eg. Doney et al. (2003)), though model error could be a contributing factor. However, another indication of excess tropical rainfall in this product is that it is significantly larger than the others between $15°S$ and $5°N$ (Fig. 3). In the extratropics, in particular the southern zone, Xie-Arkin precipitation does result in realistic vertical distributions of ocean salinity (Yeager & Large 2004). The GPCP satellite-gauge precipitation product, made available through the Global Precipitation Climatology Project of WCRP (Huffman et al. 1997), represents a state-of-the-art reconstruction of monthly precipitation flux from 1979 to the present, again on a global 2.5 degree grid.

The cause of the systematically higher Xie & Arkin (1996) precipitation in the tropics and lower values in the Northern and Southern zones is unclear. In the Equatorial zone we choose GPCP over Xie-Arkin based on model behavior, and over MSU, because of the length of record. However, we do choose Xie-Arkin in the Northern region, because of its general agreement with the independent SOC climatology where SOC sampling is best, and in the Southern region, mainly because

20

of better agreement between model and observed upper ocean salinities, with the agreement with SOC only a small factor due to the sampling issues. In practice, the Xie-Arkin and GPCP data sets are linearly blended between 25 and 35 degrees latitude in both hemispheres.

Unfortunately, the Xie-Arkin blend appears to become dominated at high latitudes by the NCEP model analyses, because precipitation of both datasets displays variability associated with the spectral topography extending away from from Greenland and from the Antarctic Peninsula. These patterns are mostly over sea-ice and are not particularly problematic for forcing the ocean. However, when used to force sea-ice the precipitation bands become snowfall bands, which lead to thicker ice under high snow bands. In the Antarctic the only practical alternative is to blend back into GPCP between $65°S$ and $60°S$. In the Arctic we prefer to blend into the Serreze data between $65°N$ and $70°N$. We refer to the complete blended result as the GXGXS precipitation data set. As with the radiation data, the GXGXS fields are mapped to the NCEP reanalysis T62 grid, and extended back in time with the climatological annual cycle of monthly means.

4.4 Continental Runoff

The climatological runoff of freshwater from the continents to the oceans and seas has been estimated from continental imbalances between precipitation, evaporation and storage (eg. Baumgartner & Reichel (1975)). Furthermore, this runoff has been partitioned among bordering ocean basins, using river routing schemes and flow estimates (eg. Fekete et al. (1999)). To these we have added Antarctica, then defined the 19 continental drainage basins of Table 1, and estimated the climatological runoff from each. About half of the total $1.26 \times 10^6 m^3/s$ comes from only three of these basins; South America – Atlantic, Asia – Pacific and Eurasia – Arctic.

Climatological gauge estimates of the mean flow and variance from about 1000 of the world's largest rivers have been compiled by Perry et al. (1996). We distribute the mean runoff of 275 of these rivers into the OGCM as near as possible to where they truely discharge into the sea. This "gauged" river runoff accounts for as much as 95 % of the runoff from both South America and Europe into the Atlantic Ocean, but about 50 % is more typical. The remaining "coastal runoff" (Table 1) is distributed evenly along the coast of each basin. This includes all the runoff from Antarctica where there are no gauged rivers, but which should be mostly an ice flux from ice shelves.

The river and coastal runoffs are then converted to a surface freshwater flux, on an OGCM grid. The river runoff is spread over the ocean grid-cells that fall within a prescribed latitude-longitude box centered at the mouth of each river. A Gaussian distribution within the box effectively smooths the runoff to give an ocean surface salinity signature that is similar to that seen in salinity climatologies (eg. World Ocean Atlas 98 (Levitus et al. 1998)). This procedure mimics the flow of fresh estuarine water over the salty coastal sea-water and avoids excessively low salinities at OGCM grid-points near the mouths of large rivers. The "coastal runoff" is spread evenly across coastal grid-cells.

The resulting global runoff flux distribution, R in (3b), is shown in Figure 4. The signatures of the major rivers are clearly evident, and as designed, their spatial extent roughly matches the observed surface salinity features. Some of these rivers, such as the Amazon, Ganges/Brahmaputra, Zaire, Yenisei/Ob and Yangtze, contribute to the surface density flux in an major way. They each give local freshwater fluxes in excess of $100 mg/m^2/s$ ($1 mg/m^2/s \approx 31 mm/year$), which produces a density flux approximately equivalent to that of a $100 W/m^2$ heat flux. Averaged over the entire ocean area of $3.523 \times 10^8 km^2$ the equivalent freshwater flux is $3.57 mg/m^2/s$, or about 11 cm/year.

22

For many purposes it is sufficient to regard the runoff flux as constant at the climatological values in Fig. 4. However, seasonal runoff associated with wet/dry seasons of the tropics, and snow melt in higher latitudes can easily be implemented by applying seasonal variations to the runoff values in Table 1, that preserve the means. In this way extratropical runoff can be made to peak in late spring, and the Amazon in February, for example (UNESCO 1985).

4.5 Ice Fraction

Daily satellite-derived sea-ice concentration, c_i, for both the Arctic and Antarctic are available from late 1978 to the present courtesy of the National Snow and Ice Data Center (NSIDC). We use the bootstrap algorithm data product which is based on the Nimbus-7 Scanning Multichannel Microwave Radiometer (SMMR) prior to 1988, and the Special Sensor Microwave/Imager (SSM/I) from 1988 to present (Comiso 1999)). Days missing in the raw data are filled using linear interpolation, and the dataset is mapped from the original 25x25km SSM/I grid to the OGCM grid prior to integration. Since the satellite orbit inclination prevents coverage poleward of about $85°N$, a polar fill algorithm is also executed. Although the data are now available through 2001, we presently use the observed ice fraction only through 1999. Later and earlier years are filled with the climatological annual cycle of daily means over the 21 years.

The climatological mean distribution of observed sea-ice is shown in Fig. 5. In the northern hemisphere ice concentrations tend to be greater, extend farther equatorward, and generally increase monotonically from regions of permanently open ocean to regions of high concentration. In contrast, in the Antarctic's Ross Sea sector, for example, the maximum mean ice concentration is found well equatorward of the continent. Mean concentrations of around 50% are also found in other near

23

shore sectors (eg. south of Australia and of the Indian Ocean). These distribution features are caused by strong offshore katabatic winds flowing down off continental topography then out to sea.

Whenever the observed ice fraction is non-zero, it is used as the sea-ice fraction, f_i, in (2). However, if frazil ice (18, 19) accumulates in regions of $c_i = 0$, then the accumulated water content of the frazil ice, W_F is used to compute a grid cell fraction

$$f_i = W_F / W_1, \tag{25}$$

where W_1 is the water content required to cover a grid cell with 1 meter of ice. Thus, as frazil ice is formed where it is not observed, the ocean fraction (f_o) is reduced, presumably reducing the air-sea heat loss and reducing the frazil ice formation. If at any time there is non-zero observed ice ($c_i > 0$), the accumulated ice is reset to zero, so that the forcing can be governed by observations using $f_i = c_i$.

4.6 Observed Sea Surface Temperature

The ensemble of forcing datasets is intended for use with an active OGCM whose evolving SST is used to compute the air-sea fluxes, as described in Section 2. However, an SST data set is required for the purpose of calibrating and validating the forcing ensemble (Sections 5,6 and 7), and for completeness in cases where the restoring boundary condition (17a) is used. We make use of a new SST data set that has been made compatible with historical sea-ice distributions (Hurrell et al. 2003). It is based on a merger of an SST analyses of satellite and in situ data (Reynolds et al. 2002) from 1982, with historical SSTs reconstructed from ship observations beginning in 1871 (Rayner et al. 2003). Using these SSTs in conjunction with the NCEP/NCAR reanalysed atmospheric state allows the reconstruction of the turbulent fluxes from the bulk formulae (4) and the outgoing longwave part of Q_L (8),

from 1948 to the present.

4.7 Observed Sea Surface Salinity

The restoring boundary condition (17b) requires a sea surface salinity data set in sea-ice regions. A global data set would enable some restoring to observed salinity everywhere. Although such forcing is not physical, it may be necessary in the absence of a natural negative feedback to prevent uncontrolled drifts in model salinity in response to very inaccurate freshwater forcing (eg. precipitation). In order to better represent the Arctic Ocean and neighboring seas, we use the Polar science center Hydrographic Climatology (PHC) ocean salinity (Steele et al. 2001). This dataset merges the World Ocean Atlas 98 (Levitus et al. 1998) with the regional Arctic Ocean Atlas (Timokhov & Tanis (1997); Timokhov & Tanis (1998). The result is a 1 degree global climatology of monthly mean ocean temperature and salinity.

Unfortunately, a similar effort cannot be mounted in the Antarctic, because the data do not exist. There is concern about a bias sampling to fresh summer conditions due to sea-ice melt around Antarctica. Doney & Hecht (2002) attribute inadequate formation of dense, cold, and relatively saline shelf water, the precursors of AABW, to this problem. Therefore, we have adopted their simple modification. The restoring SSS of (10) becomes the highest salinity found with a potential temperature less than $1.5°C$ and within within the uppermost 300m, based on the argument that those water properties are more representative of surface winter shelf water.

5 Corrections and Adjustments

Any collection of ocean forcing datasets represents a choice from among a number of different atmospheric data products, each with advantages and disadvantages. For reasons advanced in Section 4, we choose the NCEP/NCAR reanalyses of the

atmospheric state, the ISCCP-FP radiation, the GXGXS precipitation blend, the NSIDC ice concentration, and the continental runoff of Fig. 4. In any such ensemble of datasets errors and biases are inevitable. Therefore, some procedure is needed to determine objective corrections that should, at least in principle, result in a globally balanced forcing ensemble for uncoupled OGCM experiments, ocean hindcasts and hopefully OGCM-SIM coupled integrations.

We have adopted the following procedure. The fluxes are computed using the annually varying reconstructed SST fields, over the 17 years (1984-2000) spanned by all the data sets (Fig. 2). Not surprisingly, neither the heat, nor freshwater fluxes are close enough to zero in the global, 17-year mean to be consistent with ocean observations. The heat budget is attacked first, by finding corrections to the elements of the shortwave radiation and latent (evaporative) heat fluxes; namely, Q_I, the wind speed and the specific humidity. The sensible heat flux plays a more minor in the global budget, and there is insufficient comparative data to allow an objective adjustment to the longwave radiation. Then, the only way to significantly alter the freshwater budget is to change the precipitation, since the evaporation is fixed by the latent heat flux, and runoff is too small a term in (3b). Forcing with the altered datasets at least allows the possibility for an OGCM to successfully reproduce historical SSTs with reasonable fluxes.

The corrected datasets are then used to force a coupled OGCM-SIM system for several decades. If needed, further adjustments are then applied in the Arctic and Antarctic to give acceptable ice simulations in both hemispheres. The main criteria involved in this judgement are the hemispheric seasonal cycles of ice area, ice volume and snow accumulation, as well as the annual mean sea-ice thickness in the central Arctic. Ice extent is not considered even though it can dramatically alter air-sea fluxes near important sites of deep convection. These forcing modifications potentially involve the air temperature and radiation data sets, as well as the rain/snow

26

threshold temperature and the snow and ice albedos. However, little open ocean area is involved, so there is little effect on global balances.

The initial computations with no corrections resulted in a 17-year (1984–2000) global mean air-sea heat imbalance of $+31W/m^2$ and global mean air-sea freshwater plus runoff imbalance of $3.4mg/s/m^2$. The breakdown into components is shown in Table 2. With all corrections implemented, these global imbalances are reduced to $1.0W/m^2$ and $-0.1mg/s/m^2$, respectively.

5.1 Wind Speed Correction

A recent comparison of NCEP reanalysis fields with research vessel observations shows evidence of a consistent low bias in NCEP wind speeds at all latitudes (Smith et al. 2001). The bias is more pronounced the higher the wind speed and is attributed to weak pressure gradients in the NCEP reanalysis. The advent of satellite wind speed products makes a more global assessment possible. Physically, these speeds should best correspond to $|\Delta \vec{U}(10m)|$ and are a more straightforward scatterometer measurement than the wind direction. We utilize the QSCAT (QuikScat scatterometer) wind fields over a two-year period (2000-2001). These are constructed 6-hourly on a half degree grid following Chin et al. (1998). The problem of missing satellite data (eg. near sea-ice and during satellite down times) is handled by blending with with NCEP reanalysis winds, so this should not contribute to differences between the QSCAT product and our wind forcing. These QSCAT winds would be ideal for forcing OGCMs, but for the short record.

Figure 6 shows the ratio of the two year mean QSCAT speed to that from NCEP. A low bias is again evident in the NCEP winds, with this ratio greater than 1 everywhere except a few isolated regions off the coasts of South America and Africa. The QSCAT winds are between 5 and 10 % higher than NCEP winds over most of

27

the mid-latitude ocean, and the ratio is considerably higher in select regions near the equator and the poles. To correct the NCEP wind speed bias, we multiply both reanalysis vector wind components $u(10m)$ and $v(10m)$ by the spatially-dependent factor plotted in Fig. 6. The overall effect is to make the evaportation and turbulent heat fluxes more negative, thereby improving the global heat balance by $8W/m^2$, and the freshwater balance by $2.9mg/m^2/s$ (Table 2). There is no attempt to correct wind direction, despite known problems, because the ambiguity removal complicates scatterometer wind direction retrievals.

5.2 Relative Humidity

The near surface humidity in the NCEP reanalysis is too high. The relative humidity, γ, is seldom less than 80%. In many extratropical regions this minimum is greater than the observed average. Large et al. (1997) were able to match the Kent et al. (1993) observed annual cycle of latent heat flux in the North Atlantic only after reducing the NCEP specific humidity by a factor of 0.93. In the western tropical Pacific, a comparison of NCEP relative humidity to TAO mooring data in the equatorial Pacific shows a year-round positive bias of $\approx 2 - 3\%$ (Wang & McPhaden 2001). Plausible reasons for this bias are that ship based ocean humidity measurements that are assimilated into the reanalysis are more likely too wet than too dry (Kent et al. 1993), and that the NCEP model evaporates too much (Smith et al. 2001) and transports too little vertically out of the boundary layer. The excess evaporation is accomplished despite the low wind speeds and moist near surface by an excessively large transfer coefficient, C_E (Smith et al. 2001).

We attempt to improve upon the uniform drying correction of Large et al. (1997) by utilizing the TAO results and the relative humidity from the SOC surface climatology. The former suggests reducing NCEP relative humidity by 3% in the tropics

and this is used as a minimum correction at all latitudes. Figure 7 shows that NCEP relative humidity exceeds the SOC climatology almost everywhere outside the tropical band $20°S$ to $30°N$, with local differences exceeding 14%. The SOC humidities should be most reliable in the northern Hemisphere, because of the greater number of ship reports and the extensive work of Kent et al. (1993) in the North Atlantic. Therefore, in the north we use a smoothed version of the zonally averaged difference as a correction, wherever it exceeds the minimum 3%. This is more than 7% around $60°N$. In the absence of any further information, and because of the rough symmetry in Fig. 7 about the equator, we use a similar correction in the south, but with much less confidence. It is a maximum of about 6% at $50°S$. The net result is the NCEP bias $\delta\gamma$ shown as a function of latitude by the dashed line in Fig. 7.

The correction added to the NCEP specific humidity before use in the bulk formulae (4a) and (7c) is given by:

$$\delta q = -(\delta\gamma \ / \ 100\%) \quad qsat(\theta(10m)) \ , \quad < 0, \tag{26}$$

The fractional correction, $(\delta q/q)$ is always $(\delta\gamma/\gamma)$. Over the ocean, $qsat$ varies from $0.004kg/kg$ at $0°C$ to 0.010 at $15°C$ and to 0.025 at $30°C$. Thus the 3% smaller relative humidity in the tropics can become a bigger specific humidity reduction than the 7% change at $60°N$. Over ice and snow, $qsat$ monotonically decreases from about $0.004kg/kg$ at $0°C$ to 0.0003 at $-30°C$, so δq is small, ranging between about 0.0001 and 0.00001, and has little effect on the surface heat flux. Overall, lowering the relative humidity increases the latent heat flux loss by $13W/m^2$ (Table 2), which is less than the Large et al. (1997) uniform reduction of near surface specific humidity.

5.3 Air Temperature

Over most of the globe NCEP surface air temperatures are not corrected, because ship measurements, especially at night, are not so biased as humidity, and it would only effect the sensible heat flux, which is not a large term in the global heat budget. However, comparison of NCEP temperatures with weather station and drifting buoy data from Antarctica reveals that a persistent very cold bias exists in the reanalysis product at extreme southern latitudes, especially in the winter. This results in excessive surface cooling and potential water mass formation rate errors in a critical region supplying water to the deeper reaches of the world ocean. Potential sources of the problem are a lack of open water near the Antarctic coast, because the NCEP atmospheric boundary condition does not allow partial ice cover, and the height of the land stations. In any case, it does not appear as if the much warmer station and buoy data are influencing the reanalysed air temperatures.

Figure 8 (top panel) shows the minimum air temperature that we permit as a function of latitude and day of the year. These temperatures are sinusoidal fits to observed monthly minimum temperatures at each latitude (F.O. Bryan, personal communication, 2002). Colder NCEP temperatures are set to this minimum, at all latitudes south of $60°S$. In winter it is not uncommon to find $-60°C$ NCEP air temperature that this procedure warms to $-30°C$. Figure 8 (bottom panel) also shows the seasonal cycle of the mean difference between corrected minus uncorrected air temperatures zonally averaged over only ocean/sea-ice areas at each latitude. These differences reach $12°C$ over a range of latitudes over several months. The effects have largely diminished by $60°S$, where the corrections cease. Although the air temperature corrections significantly reduce the sensible heat flux from the Antarctic in winter, there is a negligible effect of the global heat budget because of the small ocean area involved.

The POLES (Polar Exchange at the Sea Surface) project has produced gridded air temperatures for the Arctic north of $60°N$ from 1979 through 1997 (Rigor et al. 1999). The product combines buoy and land station data within an optimum interpolation scheme. Over the Arctic cap north of $70°N$, the annual average POLES and NCEP air temperatures differ randomly by only about $\pm0.5°C$, so no overall NCEP correction is warranted. However, Fig. 9 shows that there are systematic seasonal differences, with NCEP being warmer in spring and summer, but colder in fall. Since seasonal temperatures can effect snow melt and albedo, NCEP air-temperatures are corrected monthly by the mean monthly climatological difference between POLES and NCEP. From Fig. 9, the 12 monthly corrections (January through December) are 0.49, 0.06, -0.73, -0.89, -0.77, -1.02, -1.99, -0.91, 1.72, 2.30, 1.81 and $1.06°C$.

5.4 Radiation

Shortwave radiation is a major term in the global heat budget. Also, it is large at latitudes where there is a lot of ocean. Therefore, small tropical and sub-tropical errors in this field can significantly impact the global heat balance. A comparison (not shown) of the climatological zonal mean net shortwave flux, Q_S (11), from the ISCCP-FP dataset with a variety of other zonal means (eg. Beranger et al. (1999) and Taylor(ed.) (2000)) reveals that it exceeds all other datasets between about $50°S$ and $40°N$. These other data sets include SOC, COADS, NASA Langley Research Center (Darnell et al. 1996), NCEP/NCAR reanalyses and the ERA-15 reanalyses (Gibson et al. 1997).

For consistency and to achieve a better global heat balance, we reduce the ISCCP-FP shortwave insolation, Q_I by 5% for all latitudes from $50°S$ to $40°N$ and 30N. This correction is within the uncertainties of the ISCCP-FP product (W. Rossow, personal communication, 2003). For smoothness, we linearly diminish the

31

correction between $50°S$ and $60°S$ and between $30°N$ and $40°N$. No correction is applied poleward of $60°S$ and $40°N$. For ease of comparison, Fig. 10 shows the resulting net shortwave, Q_S, as a climatological zonal mean flux before and after the correction. The reduced zonal means are within the range of other products in the tropical band. The global mean is lower by only $8W/m^2$ (Table 2).

Our CCSM coupled OGCM/SIM simulations tend to produce Arctic sea-ice that is too thin. In order to produce thicker sea-ice, a constant offset of $-5W/m^2$ is applied to the ISCCP-FP downwelling longwave radiation over the Arctic cap poleward of $70°N$. For smoothness, this adjustment is linearly reduced to zero between $70°N$ and $60°N$. There is negligible impact on the global air-sea heat flux, because very little open ocean is involved.

5.5 Precipitation

With the above wind and humidity corrections and uncorrected GXGXS precipitation, the freshwater budget (2b) over the global ocean is about $-5mg/s/m^2$. To better balance the global oceanic water budget, both a gain (1.1417) and bias ($0.7mg/m^2/s$) are applied to the GXGXS precipitation fields. The global mean freshwater flux then becomes $-0.1mg/s/m^2$ (Table 2). This correction is designed to shift the GPCP curve of Fig. 3 into agreement with SOC and MSU at the 7°N peak in precipitation. By chance, the improved SOC agreement holds equatorward of about 35°. However, farther poleward the increase in Xie & Arkin (1996) precipitation to values higher than SOC, is minimized by the gain plus bias correction. The corrected values are still less than GPCP in both latitudes, as favored by ocean model salinity results. It would be possible to make regional adjustments, but the uncertainties in all the data sets and the computed evaporation make it difficult to justify such fine tuning.

6 Climatological Air-Sea Fluxes

The ensemble of corrected forcing datasets is primarily intended to force OGCMs with or without a coupled sea-ice model. However, an obvious, straightforward variant is to use observed SST in the OGCM forcing scheme. In section 5 the resulting heat and freshwater fluxes were used to check the effects of various corrections on the global budgets. Such fluxes can also be used as observationally based estimates of the air-sea fluxes, because they are not dependent on an ocean model solution. They differ from many such flux products in that they are based on a variety of data sources, primarly satellite and re-analysis, but with objective corrections that utilize additional observations. The specific flux products produced by this procedure are $f_o Q_{as}$ from (2a), neglecting the small Q_P term of (3a), $f_o F_{as} + R$ from (2b) and $f_o \vec{\tau}_{as}$ from (2c). Over the ice free ocean these fluxes are the same as the total ocean forcing fluxes Q, F and $\vec{\tau}$. In the presence of sea-ice they differ from these totals by the $f_i Q_{io}$, $f_i F_{io}$ and $f_i \vec{\tau}_{io}$ terms of (2).

Our OGCM forcing machinery interpolates the atmospheric state variables from the T62 NCEP grid onto an ocean model grid where the fluxes are computed. In order to mimic OGCM output, the SSTs are interpolated onto the ocean model grid too. In contrast, the remapping of fluxes like radiation and precipitation must be conservative, and this is accomplished by keeping the fluxes constant over all the ocean area under a T62 NCEP grid. Since the ocean grid is finer (nominally 1.2° in longitude, 0.3 to 1.0° in latitude), grid points at neighboring latitudes can receive the same flux with the result that radiation and precipitation fields have steps that ramp across the boundaries of the T62 grid. This behavior is removed in two-dimensional maps by spatial smoothing. However, it is retained in zonal averages, where it is further complicated at high northern latitudes where numerical considerations have lead to a displacement of the model "North Pole" into Greenland.

6.1 Air-Sea Heat Flux

The climatological mean air-sea heat flux $(f_o \ Q_{as})$ computed from 1984 through 2000 is shown in Fig. 11. All the expected features are evident; strong heating along the equator with a maximum in the eastern Pacific in excess of $125W/m^2$, a band of predominant heating along $50°S$, heating along the eastern boundaries of the subtropical gyres of the Pacific and Atlantic, strong cooling in the Nordic seas between Greenland and Europe and between Greenland and Labrador, and strong cooling over the western boundary currents and their extensions, including the Agulhas retroflection. The uncertainties in these fluxes and in other climatologies means that there are always similarities and differences in the details of all global climatologies. However, one large scale difference between Fig. 11 and the SOC climatology is the much greater SOC heating in the tropics from Africa east to the dateline. The area is great enough to factor significantly in the SOC global heat imbalance of $30W/m^2$. It includes the TOGA COARE region of the western Pacific where SOC shows $60W/m^2$ heating compared to less than $25W/m^2$ in Fig. 11. Observational and ocean budget estimates (eg. Gent (1991)) place the net heat flux at between 10 and $20W/m^2$.

Climatologies of the air-sea heat flux components are shown in Fig. 12. Over most of the ocean the net (Fig. 11) is a balance between the absorbed solar heating (Fig. 12a) and the latent (Fig. 12b) plus longwave cooling (Fig.12 d). However, the sensible heat flux (Fig. 12c) is a significant contribution to the cooling over western boundary currents and their extensions, in the Nordic and Labrador seas and along the coasts of Antarctica and Alaska. The relatively small net longwave cooling is an important factor in the net heating along the eastern boundaries of the South Atlantic and South Pacific oceans.

The primary balances are clearly evident in Fig. 13, which shows the zonal

averages of the net heat flux (Fig. 11) and of its components (Fig. 12). At least in ice free regions, these Figures are directly comparable to any climatology that includes all the components, including those in Beranger et al. (1999) (eg. SOC, NCEP, ERA-15 and COADS). Of these, SOC heating is much the strongest between about $40°N$ and $40°S$. Other comparative examples are shown in Taylor(ed.) (2000). In the presence of sea-ice the observed ice fraction (Fig. 5) has been used to give an estimate of the actual air-sea fluxes, but the zonal averaging is over all the non-land fraction. The sharp increase in flux magnitudes south of $70°S$ is due both to an increasing ocean fraction in the Ross Sea (Fig. 5) and an increasing land fraction, which respectively, increase the numerator and decrease the denominator of the zonal averages in Fig. 13. High latitude comparisons are only valid with climatologies that have a similar treatment of sea ice. Therefore, the strong net cooling poleward of $70°S$ is not always evident in climatologies. It is confined to nearshore regions of the Weddell and Ross seas and so has little effect on the global surface heat budget. However, this localized cooling is believed to play a major role in the formation of dense shelf waters, which spill over the continental slope as Antarctic Bottom Water.

The relative humidity reductions (Fig. 7) are not overly objective, but essential to achieving a global heat balance by increasing the latent cooling. Between 30 and 60 degrees latitude in both hemispheres, the large reductions are based on the SOC climatology and as a result there is very good agreement in the zonal mean latent heat flux between Fig. 11 and SOC. However, the Fig. 13 flux in the tropics is much more negative than SOC, because of the lower air humidity, but not very different from some of the climatologies shown in Taylor(ed.) (2000). The solar insolation corrections of Section 5 force the the net solar flux values in Fig. 13 to be well within the scatter of other climatologies. At all latitudes the zonal average sensible heat flux cools more than SOC, but only by less than $5W/m^2$. There is better agreement with other climatologies shown in Taylor(ed.) (2000). The zonal mean net longwave

radiation is well within the scatter of other climatologies at all ice-free latitudes. Over the Arctic cap poleward of $70°N$ the ISCPP-FP downwelling longwave averages $236W/m^2$ compared to only $213W/m^2$ from ERA-15. This difference is much more than the $-5W/m^2$ correction applied to improve sea-ice simulations.

Figure 14 shows the northward heat transport (global and by basin) implied by the air-sea heat fluxes of Fig. 11. In such a plot, the zonal average heat flux gives the slope of the curves (positive for heating, negative for cooling), while the value at a particular latitude represents the integrated heat flux from all ocean areas farther north, or equivalently in a balanced system, minus the integrated heat flux from all ocean areas farther south. The missing ocean heat loss via ice-ocean fluxes are believed to be only few W/m^2, but these would steepen the negative slopes at high latitudes and give larger poleward maxima in both hemispheres. Figure 14 suggests that the heating around $50°S$ is approximately equal to all the heat loss farther poleward, so that very little heat is transported across $40°S$. Similarly, there is little transport across $10°S$, but a large northward transport of nearly 1PW across the equatorial Atlantic. Although the sum of Indian plus Pacific transport gives the correct Indo-Pacific implied transport, partitioning between the two basins assumes no heat transport via the Indonesian Throughflow, which is not correct.

Bryden & Imawaki (2001) have compiled a number of ocean heat transport estimates that can be compared to Fig. 14. Unfortunately these estimates are so scattered that Fig. 14 nearly always agrees with some other estimate, but could not possibly agree with all. For example, consider $24°N$ in the Pacific where the heat transport in Fig. 14 is about $0.4PW$, compared to an ocean section analysis of $0.76PW$ and a global ocean inverse analysis of $0.45PW$ (MacDonald 1998). Since there is also good agreement with the inverse analysis at $24°N$ in the Atlantic, there is very good agreement in the total ($1.4PW$ versus $1.5PW$), but section analysis gives a higher total of $2.0PW$.

6.2 Air-Sea Water Flux

Figure 15 shows the mean (1984 – 2000) global distribution of air-sea freshwater flux (1984 – 2000), plus the climatological continental runoff from Fig. 4. The precipitation (Fig. 16a) differs from the component GXGXS data sets (Fig. 2) by the balancing correction (Section 5) and by a factor f_o in the presence of sea-ice, which is why it tends to zero at high latitudes. From Eq. 4b, the evaporation component (Fig. 16b) is just Λ_v times the latent heat flux (Fig. 12b). The obvious freshwater source regions (unshaded in Fig. 15) are the intertropical convergence zones (ITCZs), the midlatitude storm tracks of both hemispheres, and the mouths of large rivers (Fig. 4). There is net water loss (evaporation) from the Arabian Sea and the subtropical gyres of each ocean basin. These features are common to all freshwater flux climatologies, although the magnitudes of the precipitation and evaporation differ substantially, with no way of determining reality.

The zonal averages of the freshwater flux and its components are shown in Fig. 17. The variability in runoff south of $60°S$ reflects changes in the fraction of ocean that is near the Antarctic coast, since Antarctic runoff is distributed equally across OGCM coastal grid boxes. By construction, all the most southerly ocean grid boxes are coastal, and so receive Antarctic runoff (Fig. 4), which dominates the freshwater budget at the most southerly model latitude (Fig. 17). However, the small area means the freshwater input is not large. The runoff from Siberian rivers is the dominant component between 60 and $70°N$. Runoff also becomes a significant fraction of the total flux at latitudes where where precipitation and evaporation are in close balance.

Integration of fluxes in Fig. 15 gives the implied northward transport of freshwater shown in Fig. 18. Again partitioning between the Indian and Pacific incorrectly assumes no transport through the Indonesian Throughflow. The total transport can

be compared to several other estimates and direct observations given by Wijffels (2001). In general there is better agreement with the direct observations in the northern Hemisphere than in the southern.

6.3 Wind Stress

Climatologies (1984 – 2000) of the zonal and meridional wind stress components are shown in Fig. 19 as maps and in Fig. 20 as zonal averges. The pattern and magnitudes of both components are remarkably similar to the SOC climatology, which has generally larger stress magnitudes than the COADS (Beranger et al. 1999). Since the SOC and COADS are based on essentially the same ship observations this difference is likely due to use of a different drag coefficient formulation. It also appears that NCEP reanalysis employs a larger drag coefficient than Eq. (6a) (Fig. 1), because a comparison (not shown) of NCEP stress and Fig. 19 does not show the differences implied by the wind speed correction of Fig. 6.

7 Climatological Seasonal Cycles

For each of the air-sea fluxes computed from 1984 through 2000, there are a total of 204 monthly means. The 17 values from each month are averaged to give a climatological annual cycle of 12 monthly means. This cycle is partitioned into its first (12 month period) and second (six month period) harmonics plus a residual. Each harmonic is described in terms of three quantities; amplitude, phase (the month of its first peak), and the percent of the seasonal variance that it explains. There is no contribution to any freshwater flux variability from the constant runoff data set.

38

7.1 Air-Sea Heat Flux

The results from the air-sea heat flux calculations are shown in Fig. 21a (first harmonic) and Fig. 21b (second harmonic). Away from the tropics and regions of seasonal ice cover, the first harmonic dominates; accounting for at least 60% of the variance and in most places more than 80%. This signal reflects the solar cycle in Q_S. Accordingly, the annual cyle of heat flux peaks in June/July in the northern Hemisphere and in Dec/Jan in the southern. However, the amplitude of the first harmonic, A_1, is much larger in the northern hemisphere, most likely due to seasonal heating of neighboring continents. In the regions associated with the western boundary currents and their extentions the mean cooling (Fig. 11) is generally less than A_1, implying that there is net heating at least in June and July. Similarly, A_1 is much greater than the mean heating along $50°S$, so that there is cooling over nearly half the year. In such regions uniform sampling over the annual cycle is particularly important in establishing the annual mean heat flux.

Along the equator in all basins the second harmonic (Fig. 21b) becomes a significant contributor to the annual cycle, explaining at least 60% of the variance at most longitudes. The phase corresponds to the twice yearly overhead passage of the sun in late March and September. However, the amplitude, A_2, is usually less than $25W/m^2$ and too small to change the sign of the heating. The exception is the Asian monsoon regions of the Arabian Sea, Bay of Bengal and East China Sea, where A_2 can exceed $50W/m^2$

At some high latitudes in both hemispheres the annual cycle of air-sea heat flux is not well described by the first and second harmonics. This likely reflects the fact that two large contributors, solar heating and sea-ice concentration are roughly 2–3 months out of phase, with the latter lagging.

39

7.2 Air-Sea Freshwater Flux

There are only a few distinct regions where the first harmonic of freshwater flux (Fig.22a) is both large ($> 25mg/m^2/s$) and explains a significant fraction of the variance ($> 60\%$). These include the ITCZs and areas effected by the Asian monsoon, where there is a large positive freshwater flux (Fig. 15) due to exessive precipitation (Fig.16a). There are some areas of net evaporation, such as the south Indian Ocean and much of the north Pacific subtropical gyre, where the first harmonic explains most of the variance even though the amplitude is small. In all these areas of both net precipitation and net evaporation, the amplitude of the first harmonic tends to be smaller than the magnitude of the climatological mean freshwater flux, so regions of net precipitation, or of net evaporation tend to remain so throughout the year. The maximum freshwater flux occurs in August-September in the northern ITCZs, in January in the South Pacific convergence zone, and in June-July over the Asian monsoon regions.

The second harmonic of freshwater flux (Fig.22b) contributes little to the seasonal cycle. The amplitude exceeds $25mg/m^2/s$ and explains more than $> 60\%$ of the variance only in small regions of the eastern equatorial Atlantic and the Arabian Sea.

7.3 Wind Stress

The harmonic analyses of the zonal and meridional wind stress components are displayed in Fig. 23 and Fig. 24, respectively. The polar easterlies show large annual variability especially off the Indian Ocean coast of Antarctica, where it accounts for in excess of 60% of the annual variance in both stress components. Here, the maximum easterly (negative τ_u) and southerly (positive τ_v) stresses occur in June.

The annual and semi-annual variability in Southern Hemisphere westerlies have been described by van Loon & Rogers (1984b) and van Loon & Rogers (1984a), respectively. In accord with the latter, there is a circumpolar band of relatively high zonal wind second harmonic amplitude ($> 0.02 N/m^2$), with relative peaks in each ocean basin, and a distinct phase shift from equinoxial peaks south of about $50°S$ to solstitial peaks farther north (Fig. 23b). However, signal north of $50°S$ appears much reduced in this 43 year mean, than in the 1979 picture from van Loon & Rogers (1984a). The only other significant signal in this region is the strong first harmonic variability in zonal stress found in the Indian ocean sector (August peak) that weakens in the Pacific (July peak) and is weaker still in the Atlantic (Fig. 23a).

The Asian monsoon stands out as a large amplitude (as much as 1 N/m^2) first harmonic, peaking in June/July in both components, with centers of action in the Arabian Sea, the Bay of Bengal and the East China Sea. Elsewhere in the tropics there is significant annual variability along $15°N$ in both components, that gives maximum easterly stress in February/March, and along $10°S$ in the Indian and east Pacific regions, that is maximum easterly in August.

The Northern Hemisphere westerlies are characterized by a strong annual harmonic, that accounts for as much as 80% of the variance. In the Pacific there is a gradual phase shift going north toward the polar easterlies.

8   Interannual to Decadal Variability

Much of the observed interannual to decadal variability is displayed in Fig. 25 , as time series of several large scale climate indices from 1950 - 2000. The North Atlantic Oscillation (NAO) and North Pacific (NP) indices are winter averages of December through March and November through March, respectively, but are plotted at mid-year. The El Nino - Southern Oscillation (ENSO) signals are the SST Anomaly

from the Nino 3.4 region and the Southern Oscillation Index. These values and the Antarctic Oscillation are 5 month running means of monthly values. All the indices display significant interannual and longer variability, and we now explore how these signals are captured by our cycle of multi-year forcing.

For this purpose, annual means of all the fluxes have been computed for the 43 years from 1958 through 2000. On these time scales, different air-sea interaction processes may be at work in the different ocean basins, so after removal of the climatological means, zonal averages of the air-sea flux anomalies were constructed for the Indian, Pacific and Atlantic Oceans. An important caveat is that only the atmospheric state and SST datasets vary throughout the 43 years (Fig. 2). Other dataset have been extended back in time using climatological annual cycles of monthly means from the period of time for which they are available. Again, there is no variability in runoff.

The zonally averaged annual air-sea heat flux anomalies are shown for each ocean basin in Fig. 26. The full variability represented after 1983 is not noticably different than the partial variablity resulting from the variable atmospheric state and SST. This observation suggests that the radiation and in particular the solar component doesn't contribute much to interannual variability even though it dominates the seasonal cycle (Section 7). This notion is confirmed by Fig. 27, where the annual anomalies of Q_S are displayed. The maximum anomaly is only $-10W/m^2$. It is evident in 1992 between the equator and $20°S$ in the Pacific and Atlantic Oceans, and to a lesser extent in the Indian. This signal is almost certainly a reponse to the Pinatubo volcanic eruption of late 1991. However, in the Pacific there may be a some contribution to this negative Q_S anomaly from the 1992-93 ENSO warm event, because the warm events of both 1986–87 and 1997-98, for example (Fig. 26), correspond to small negative anomalies.

The interannual variability of the air-sea freshwater flux is dominated by fluctuations in tropical precipitation (Fig. 28). These are so strong that the contour interval becomes too large to show much of either extratropical precipitation anomalies, or the evaporation anomalies associated with the latent heat flux variability that are so evident in Fig. 26. Therefore, the interannual variability of freshwater forcing prior to the satellite era and datasets such as GPCP, remains obscure, because the dominant signal is missing.

The interannual variability of the Antarctic Oscillation (AAO) is most clearly reflected in the zonal wind stress anomalies (Fig. 29) south of $40°S$ in all three basins, but especially the Indian ocean. In particular, weaker eastward stress in the 1960s corresponds to negative AAO, while the large positive AAO peaks in 1979, 1985, 1989, 1993 and 1998 are all associated with positive wind stress anomalies. Meridional anomalies are weaker, but positive northward wind stress anomalies tend to be associated with negative AAO (eg. the 1960s). Interestingly, the changing winds are not consistently reflected in the heat flux anomalies of Fig. 26, as might otherwise be assumed from (4).

El Nino/Southern Oscillation (ENSO) variability is reflected in the dominant tropical precipitation signals, with annual mean anomalies from years following warm events being strongly positive in the Pacific, weakly positive in the Indian, and negative in the Atlantic. The heat fluxes have a corresponding signal only in the Pacific where they respond directly to warmer SST by becoming more upward (negative), according to (16). Thus, they retard ENSO warming and cooling, as they do in a forced OGCM (eg. Doney et al. (2003)).

Zonal wind stress anomalies, and to a lesser extent meridional anomalies (Fig. 30), in the North Atlantic poleward of about $40°N$ reflect the North Atlantic Oscillation (NAO), with positive stress when the NAO index is high. Corresponding negative

heat flux anomalies (more latent and sensible cooling when the westerly winds are stronger) are evident in Fig. 26. However, these are less pronounced during the period of generally high NAO index during the 1990s.

Neither the heat flux, nor wind stress anomalies in the North Pacific appear to be directly related to the North Pacific Index (NPI). Low values of the index correspond to both positive (eg. 1970) and negative (eg. 1981 and 1983) zonal stress variations. The heat flux anomalies tend to follow the wind and are, therefore, of the opposite sign. There is no persistent anomaly in either the heat flux, or zonal stress throught the period of high NPI from 1989 through 1991.

The most prominent decadal variability is seen in the heat flux anomalies of Fig. 26. Negative anomalies are prevalent in the 1960s and 1990s in all three basins, with positive anomalies more evident in the 1980s. Thus, the geographical extent of decadal variability appears to be much more global in extent than any of the regional indices of Fig. 25. This variability is shown more clearly in the time series of global and basin average heat flux shown in Fig. 31. The calculated global averaged heat flux into the ocean is clearly greatest, by about $5W/m^2$, between about 1975 and 1990. The relative cooling of the 1960s and the late 1990s is a consequence of less Pacific heating, and Atlantic cooling, with the Indian and Southern oceans contributing mainly to the 1990s signal. The relative warming of 1980s appears in all the basins.

Unfortunately, the corrections to the flux products (Section 5) change the heat flux by more than the magnitude of these decadal variations. Therefore, the decadal signals have considerable uncertainty and can at best be considered a measure of relative change, since the same corrections are applied each year. The 1984 to 2000 period used in the balancing of Section 5 includes years of both relatively large and small global heating. Therefore, the $1.02W/m^2$ imbalance is similar to the $1.6W/m^2$

global imbalance over the 43 period of Fig. 31. However, the danger in determining corrections based on balances over short periods, such as 1979 to 1985 for example, is clearly shown in Fig. 31. The difference compared to a period such as 1992 to 2000 is more than $5W/m^2$.

9 "Normal" Year Forcing

For many purposes the interannual variability explored in Section 8 obscures the signals of interest, so this section describes the construction of an alternative "normal" year of forcing data. Normal-Year-Forcing (NYF) consists of single annual cycles of all the data needed to force an OGCM and SIM. These data are representative of climatological conditions over decades and can be applied repeatedly for as many years of model integration as necessary. Such forcing is well suited for studying certain aspects of OGCM behavior, such as initial trends, the approach to equilibrium and internally generated ocean variability on interannual and longer timescales. It is also useful for sensitivity studies. A practical advantage is that only the data from a single year need be made available to the model.

There are several criteria which we would like the NYF to satisfy, but practical considerations mean that not all the forcing satisfies them all. The specific criteria guiding the formulation of the NYF are :

1: The forcing infrastructure can remain unaltered, with the normal year data sets restricted to four times daily atmospheric state data (U', V', θ', q'), daily incoming shortwave and longwave radiation, monthly precipitation and daily sea-ice concentration.

2: The seasonal cycle of forcing is to be retained.

3: There should be realistic propagation of weather over the oceans throughout the "normal" year, so that the ocean can be excited by realistic high frequency forcing, particularly the tubulent fluxes associated with storms.

4: The climatological average fluxes obtained from coupling the "normal" year to observed SST should be as close as possible to the 'observed' climatological average fluxes (Section 6), so that the mean OGCM solution is meaningful.

5: There should be a smooth transition from December of the year to its beginning in January, so that the year can be repeated without initiating spurious transients.

6: The "normal" year should not be overly weighted to any individual year, and hence the state of the atmosphere during that year.

Simply repeating the forcing of any single year doesn't satisfy (4) and (6) above, even if there is some blending to satisfy (5).

The climatological annual cycles used to extend the precipitation, radiation and ice concentration data back in time are ensemble averages over all the years each data set is available (Fig. 2). These are used as the "normal" year forcing for these variables, even though criteria (3) is not satisfied. This is not a serious detriment to these monthly and even the daily data sets, because the precipitation and radiation fluxes themselves are averaged and vector fields are not involved. Such averaging is also used to produce a "normal" year of sea surface temperature (θ_o') and from this, a "normal" year of sea surface humidity (q_o') according to equation (6). However, ensemble averaging is not an option for the atmospheric state variables, because the resulting turbulent fluxes would neither reproduce storm forcing, nor preserve mean fluxes. If required, climatological surface salinity is used for all types of forcing.

9.1 The Atmospheric State Variables

Start with a Y-year time series of NCEP/NCAR high frequency ($\Delta t = 6$ hours; N = 365 * 4 = 1460 samples per year) U, V, θ, and q. From an SST data set, construct a Y-year time series of 1460 samples per year, θ_o, and a corresponding sea surface humidity, $q_o = qsat(\theta_o)$, then the air-sea differences, $\Delta\theta = \theta - \theta_o$ and $\Delta q = q - q_o$. Compute a Y-year time series of wind speed $S = (U^2 + V^2)^{1/2}$. Construct the pseudo stress components (S U) and (S V), and the pseudo heat fluxes (S $\Delta\theta$) and (S Δq), then Fourier transform each pseudo flux time series as well as the θ and q time series, then form the power spectra with a bandwidth of $(N \cdot Y \Delta t)^{-1}$. Average these spectra over Y sequential bands, beginning with $(Y + 1)/2$. For Y an odd integer the first average is centered at frequency $(N\Delta t)^{-1}$ (period = 1 year) and the bandwidth of the averages is also $(N\Delta t)^{-1}$, so that the averages correspond to the power spectra of a single year and they preserve the variance of the original Y-year time series at frequencies greater than $(2N\Delta t)^{-1}$ (period = 2 years).

Let the kth band average of amplitude^2 be denoted as, ϕ_k. In order to determine the associated Fourier coefficients (a_k, b_k) a phase, Ω_k, is required :

$$\phi_k = a_k^2 + b_k^2 \qquad (27a)$$

$$\Omega_k = tan^{-1}(b_k/a_k). \qquad (27b)$$

The phase for each k and each time series is taken as the corresponding phase from the time series over a single "moderate" year. Inspection of Fig. 25 over the time period after 1983 when there is full data availability (Fig. 2), reveals that 1995 is perhaps the most moderate year, with none of the major climate indices (NAO, NP, ENSO and AAO) at an extreme. Therefore, the phases, Ω_k, are taken from the Fourier transforms of corresponding 1995 time series, after they have been modified to give a smooth transition from December back to January. Specifically, values

between 15 and 31 December 1995 become linear combinations of December 1994 and December 1995, with weight of the former linearly increasing from 0 to 1. The phases that set the seasonal cycle (criteria 2) should not change with choice of year, so there is no issue with criteria 6 in this regard. There is such an issue with the phases of higher frequencies that determine the propagation of weather (criteria 3), because storm patterns will tend to follow those of 1995, but their magnitudes will be be representative of the entire Y years. Once Eqs.(27) have been solved for the $k = 1,730$ Fourier coefficients, an inverse transform with the addition of the original mean produces an annual cycle of 6-hourly pseudo flux components, denoted as $(\widetilde{SU})$, $(\widetilde{SV})$, $(\widetilde{S\Delta\theta})$,$(\widetilde{S\Delta q})$, and of variables $(\tilde{\theta})$ and $(\tilde{q})$.

In order to satisfy criterion 1 the "normal" year wind components, (U', V'), are computed every 6 hours throughout the year as:

$$U' = \frac{(\widetilde{SU})}{[(\widetilde{SU})^2 + (\widetilde{SV})^2]^{\frac{1}{4}}} \tag{28a}$$

$$V' = \frac{(\widetilde{SV})}{[(\widetilde{SU})^2 + (\widetilde{SV})^2]^{\frac{1}{4}}} \tag{28b}$$

It can be shown that at each time the pseudo stress, $(S'U', S'V')$, with $S' = (U'^2 + V'^2)^{\frac{1}{2}}$, equals the transformed $(\widetilde{SU}, \widetilde{SV})$. Since the transformed pseudo stress components are constructed to maintain both the mean and variance at annual and higher frequencies of the original Y-year forcing, so must the $(S'\,U', S'\,V')$ that are used to force an OGCM. Thus, criteria (2), (4) and (6) are also satisfied. However, the means of the normal year wind components and the wind speed are not equal to the Y year averages, but these are not the quantities that force an OGCM.

Let a mean over the Y-years and a mean over the normal year be donoted as $< >_Y$ and $< >_N$, respectively. The mean sensible $(X = \theta)$ or latent/evaporative $(X = q)$ heat flux over Y-years is (neglecting the effect of varying transfer coefficients):

$$< H_X >_Y \equiv < S\,(X - X_o) >_Y = < S\,(\Delta X) >_Y \tag{29}$$

Criterion (4) is adequately satisfied if

$$< S \ (X - X_o) >_Y \quad \approx \quad < S' \ (X' - X_o) >_Y \tag{30}$$

We have explored two methods of generating θ' and q' so that climatological mean fluxes are preserved in this sense, under the assumption that an OGCM reproduces the Y year time series of surface properties X_o. Method 1 follows the route used for U' and V': a transform of the pseudo-stress yields X' at each time that makes $(S' \ (X' - X_o'))$ identically equal to $(\widetilde{S\Delta X})$:

$$X' \ = \ X_o' + \frac{(\widetilde{S\Delta X})}{(S')} \ . \tag{31}$$

Since the transform construction ensures that

$$< \widetilde{S\Delta X} >_N \ = \ < S \ (\Delta X) >_Y, \tag{32}$$

this method satisfies criterion (4) (equation 30) insofar as

$$< S \ (\Delta X) >_Y \ = \ < (S' \ (X' - X_o') >_N \ \approx \ < S' \ (X' - X_o) >_Y \tag{33}$$

Thus, all the criteria are reasonably satisfied. However, X' computed in this fashion can become unphysically different from its neighbors in both time and space; a phenomenon which we attribute to the low correlation between S and ΔX. Therefore, Method 1 has been abandoned until this "noise" issue is resolved.

Method 2 places more emphasis on criteria (4), the average of the fluxes and on retaining the spatial and temporal smoothness of the NYF fields, $\tilde{X}$, than on preserving the flux variance (criteria 2 and 3). An offset, b_X, is added to the filtered time series at each spatial point:

$$X' = \tilde{X} \ + \ b_X \tag{34a}$$

$$< S' \ (\tilde{X} + b_X - X_o') >_N \ = \ < H_X >_Y \tag{34b}$$

49

$$b_X = \frac{<H_X>_Y - <S'\,(\tilde{X} - X'_o)>_N}{<S'>_N},\qquad (34c)$$

where b_X is constant in time over the normal year. In practice, the b_X fields (not shown) are found to have little spatial variability, and to be small compared to the uncertainty in NCEP air temperatures and humidities ($|b| < 0.2°$ C equatorward of $\approx 60°$ latitude). The presence of sea-ice greatly complicated the construction of the equivalences in Eq. 43. Therefore, uncertainty and simplicity dictate that we take $b_X = 0$ everywhere. By computing q' and θ' with this form of Method 2, preservation of flux variance cannot be claimed, but the resulting fields are spatially smooth and adequately satisfy criterion 4, as will be demonstrated below.

Since the inverse transform assumes annual periodicity there is a pointwise smooth transition from the end of the year to its beginning in transformed variables such as $(\widetilde{SU})$ and $(\widetilde{SV})$, and in their derivatives, such as U' and V'. Then the blending of the phase year used to specify Eq. 27b should produce a smooth propagation of synoptic variability across the January 1 temporal boundary of the NYF dataset.

9.2 NYF Corrections

In our forcing infrastructure the system receives uncorrected data sets then forcing corrections are made online. In this way the number of data sets does not proliferate as different corrections and combinations are tested, which is what would happen if corrected versions of all the data sets had to be constructed. Although this is a much greater problem with 43 year datasets, we wish to maintain the advantages of online correction with NYF (criteria 1). There is no issue with forcing that is ensemble averaged and corrected with multiplicative gain factors and offsets that are constant in time. In such cases, like radiation and precipitation, correcting then averaging is equivalent to averaging then correcting.

This equivalence is also true for the wind speed components, though not so obvious. Suppose a constant correction factor g is to be applied to both components, as in Section 5. If this is applied directly to the data sets then the speed S changes by a factor g, while the transformed $(\widetilde{SU})$ and $(\widetilde{SV})$ both change by a factor g^2. Therefore, the NYF components given by Eq. 28 would be altered by the factor g, which is the same as correcting U' and V' after they have been computed from uncorrected data.

Equivalence holds for time varying additive corrections, only in the limit that they can be fully represented by a finite Fourier series with frequencies between the annual and 6 hourly periods of NYF. This limit is not realized by the air temperature corrections, because of the step function nature of the Antarctic limit, and the monthly Arctic correction. For the latter, equivalence could easily be achieved by specifying the correction in terms of a few discrete harmonics, but since only the high Arctic is involved we have not done so. This option is not available for the Antarctic limits. Since both the Antarctic and Arctic corrections, are based on climatological observations, it is not inappropriate to apply them to transformed uncorrected temperatures. This would seem preferable to transforming corrected temperatures and having the step function nature leak throughout the spectrum.

The two options for corrected NYF humidity, with $b_q = 0$, are

$$q' = q(1 - \widetilde{\frac{\delta\gamma}{\gamma}}) \quad and \tag{35a}$$

$$q' = \tilde{q}\,(1 - \frac{\delta\gamma}{\tilde{\gamma}}), \tag{35b}$$

where the whole right hand side of (33a) is transformed, $\delta\gamma$ is the constant in time relative humidity correction (Fig. 7), the uncorrected NCEP humidity and temperature gives γ, and the transformed humidity and temperature gives $\tilde{\gamma}$. Since relative humidity is not constant, the humidity correction is time variable and multiplicative,

51

so there is no equivalence between correction then transforming and transforming then correcting. We still choose the latter (33b), for consistency and convenience, but need to demonstrate that the differences, at least in the mean, are not important.

9.3 Verification

Above, NYF is constructed without considering variations in the transfer coefficients, which depend on wind speed (Fig. 1), and atmospheric stability. Thus, model solutions forced with the full 43 cycle of forcing will differ, even in the mean, from NYF solutions. If the "best" solutions are required we recommend using the former, and reserving NYF for specific applications where its advantages outweigh the disadvantages. However, the diagnostic NYF fluxes should not be too different from the fluxes of Sections 6 and 7.

These differences are quantified in Fig. 32. Each panel shows a comparison of climatological fluxes obtained using NYF state variables and the fully varying state variables used for the climatologies of Section 6 (hereafter denoted as 43F). Both sets of forcing data are coupled to 43-years of observed monthly SST, with interannually-varying daily sea ice fractions. A relative difference is computed from the absolute value of the difference between NYF and 43F turbulent fluxes, as a percentage of the 43-year flux. In each case this difference is less than 5% over the vast majority of the ice-free ocean, and less than 1% in many places, as expected.

The difference in mean latent heat flux is less than 5 % over most of the ocean, less than 1 % over large regions of the Tropics, with larger differences mostly confined to high latitude regions. Differences near the ice edge can be attributed in part to the fact that the NYF was not designed to preserve mean fluxes in the presence of nonzero sea ice, as well as to the low value of $< Q_x^{43F} >_Y$ at these latitudes (Fig. 12b). The same holds for the sensible flux at high latitudes, with differences

in the Southern Hemisphere exacerbated by corrections to NCEP air temperatures (section 5.3) which are not taken into account in NYF construction. Large percentage differences in sensible flux at the equator are related to very low mean fluxes at this latitude (Fig.12c). In the wind stress components there are high percentage, but small absolute, differences following the zero contours of Fig. 19, and in the low stress (small f_o) Arctic.

Differences in both latent and sensible at high latitudes are partly due to the fact that b_θ and b_q, which are non-negligible poleward of $\approx 60°$ latitude, have been neglected in Eq. 34a for simplicity. Fortunately, the resulting error is minimal over most of the global ocean relative to the uncertainties in temperature and humidity at these latitudes as well as to the neglect of varying transfer coefficients in Eqs. 34. By far the more important turbulent heat flux is the latent (top panel), and as hoped the flux difference is less than 5% throughout the ice-free ocean with the exception of only a few small regions. The largest differences are confined to high latitudes where the flux is small (Fig. 12b), so that even the 40% difference in the Weddell Sea represents less than a $10W/m^2$ absolute difference. A similar pattern is evident in the sensible heat flux where the somewhat larger percent differences are tolerable, because of the generally much smaller flux magnitudes (Fig. 12c). In the cold tongue of the equatorial Pacific, for example, a 40% difference corresponds to only about $2W/m^2$.

Figure 33 demonstrates the success of NYF in propagating weather systems (criterion 3), with a smooth transition from mid December to the beginning of January (criterion 4). In this example the zonal wind is contoured as a function of time and longitude across the Pacific Ocean along $41°N$. Uncorrected NCEP winds are shown in the lower panel from Dec 15, 1994 to January 15, 1995. The upper panel shows two segments of normal year winds; December 15 to 31, and January 1 to 15. The normal year has been wrapped so that these two segments join at

53

the horizontal black line at January 1. The prevailing westerly winds ($U_{10} > 0$) and eastward propagation are evident in both panels. Since the NYF is constructed using Fourier phases (27b) from 1995, differences during January and other months to December 15 reflect departures of 1995 Fourier amplitudes from the NYF averages (27a). Large departures are not expected, because 1995 is such a moderate year (Fig. 25). Therefore, 1995 and NYF winds are quite similar. However, during the blending window from December 15 to January 1, the phases become increasingly weighted toward 1994, so the winds in Fig. 33 become less alike as time goes back from December 31 to December 15, and the NYF winds become more like December 1995 winds. Nevertheless, eastward propagation of weather is evident throughout the transition window and across the wrap at January 1. Likewise, animations show that the transition is indiscernible to the eye, although this smoothness is achieved by the two week phase blending period, during which synoptic variability is somewhat degraded.

10   Discussion

Bulk forcing is only one way of forcing either an OGCM or a coupled OGCM–SIM. Instead of fully coupling a climate system model, prescribed data sets replace coupled atmospheric model output such as the near surface atmospheric state, the incident surface radiation, and the precipitation. Similarly, prescribed continental runoff takes the place of a land model. Therefore, coupled model infrastructure can be used unaltered for bulk forcing. OGCM forcing also requires observed sea-ice concentration and possibly some estimates of the poorly known, but presumed small, ice-ocean heat, salt and water fluxes. These fields are internally generated in a coupled OGCM–SIM, but their fidelity depends strongly on the quality of the high latitude atmospheric forcing, as well as of the models themselves. The

atmospheric datasets can be taken from the output of an atmospheric model, forced with observed SST for example. However, the main purpose for developing bulk forcing is to provide more realistic forcing, which is achieved by using observed data sets.

Unfortunately, there is no complete set of ideal data, so choices and compromises must be made. Global coverage and record length are the primary advangages behind our choices of NCEP/NCAR reanalysis of the atmospheric state, ISCCP-FP radiation and NSIDC ice coverage. Comparisons with other data sets lead to objective corrections to the wind speed and solar insolation. Although it is clear that NCEP humidities are too high, the applied corrections are less objective, especially over the Southern Ocean, being driven in part by a desire to obtain a near zero global heat imbalance. The decision to blend multiple precipitation data sets into GXGXS, is primarily based on OGCM behavior in the western equatorial Pacific and subtropical gyres, and on SIM simulations of sea-ice. The final bias correction to precipitation is subjective and justified by the desire for a near-zero freshwater imbalance and by the scatter in available products.

Sea-ice in a coupled OGCM-SIM is also very sensitive to SIM parameters, especially the snow and ice albedos and their functional dependencies. Different parameter choices and different SIM models may respond differently to high latitude corrections, such as the ad hoc reduction of downwelling longwave radiation by $5W/m^2$. In some cases it may be better to not to apply the overall precitation increase where it leads to more snowfall and to the positive feedback associated with a corresponding increase in effective albedo. It is to be expected that a thorough exploration of such issues in a variety of models would suggest modification of our high latitude bulk forcing. It is also likely that as new data sets emerge, other aspects of the forcing should also change. Therefore, the bulk forcing data sets and the proposed corrections should be regarded as temporary choices waiting for

demonstrations of shortcomings and improvements.

It is extremely unlikely that prognostic model SST will match the observations, so global heat and freshwater imbalances should be expected. The negative feedback provided by the heat fluxes (4b, 4c and 12) should control the heat budget. In many situations, such as very long integrations, artificial control of the freshwater budget may be required. A common practice is to apply a local restoring flux, F_w, of the form (17b) to the terms of Eq. 2b. Large et al. (1997) use a very small coefficient, $C_F = 23mg/m^2/s/psu$, corresponding to about a 2 year restoring times scale over 50 meters, and a coefficeint a factor two or more smaller may suffice. They choose to use this weak restoring as a local precipitation correction, and so remove the global mean. Global mean salinity drift is then controlled by multiplying the precipitation by a factor that would exactly compensate the measured change in mean ocean salinity over the previous year.

The air-sea flux climatologies produced by the corrected bulk forcing and observed monthly SST, which is held constant over each month, are estimates of what model fluxes would be if an OGCM produced the observed SSTs. Further corrections could give a global imbalance closer to zero, but these would be purely subjective and it is uncertain what this imbalance should be. Clearly it needs to be positive to account for the observed ocean warming, and for the loss of heat expected through ice-ocean fluxes. Also, the imbalance depends on the climatological years (Fig. 31). Therefore, we choose to leave small imbalances both in heat and freshwater, but remove them from calculations like the implied transports (Fig. 14 and Fig. 18) where balance is assumed.

The total heat flux must be considered a highly uncertain small difference between large, not very well known numbers, given the scatter between climatologies and the effects of the corrections (Table 2). Nonetheless, when zonally averaged

along ice-free latitudes, the Fig. 13 values are quite consistent with other climatologies, including the local positive maxima at $50°S$ and $45°N$. The exception is the SOC, which has much larger positive heat flux in the tropics, because of the greater solar heating and the reduced latent cooling.

Acknowledgments

References

Barnier, B., Siefridt, L. & Marchesiello, P. 1995 Thermal forcing for a global ocean circulation model using a three-year climatology of ECMWF analyses, *J. Marine Res.* **6**, 363–380.

Baumgartner, A. & Reichel, E. 1975 The world water balance, Elsevier, New York 180pp.

Beranger, K., Viau, K., Barnier, B., Garnier, E., Molines, J. M. & Siefridt, L. 1999 An Atlas of Climatic Estimates of Air-Sea Fluxes 19pp plus figures.

Bishop, J. & Rossow, W. 1991 Spatial and temporal variability of global surface solar irradiance, *J. Geophys. Res.* **96**, 16839–16858.

Bryden, H. & Imawaki, S. (2001) Ocean heat transport, *Ocean Circulation and Climate*, G. Siedler, J. Church & J. Gould (eds), number 77 in *International Geophysics Series*, Academic Press, pp. 317–336.

Chin, T., Milliff, R. & Large, W. 1998 Basin-scale High-wavenumber Sea Surface Wind Fields from Multiresolution Analysis of Scatterometer Data, *J. Atmos. Oceanic Technol.* **15**, 741–763.

Comiso, J. 1999 Bootstrap sea ice concentrations for NIMBUS-7 SMMR and DMSP SSM/I, Digital Media, National Snow and Ice Data Center.

Cox, M. & Bryan, K. 1984 A Numerical model of the ventilated thermocline, *J. Phys. Oceanogr.* **14**, 674–687.

Darnell, W., Staylor, W., Richey, N., Gupta, S. & Wilber, A. 1996 A climatology of surface radiation budget derived from satellite data, *J. Geophys. Res.*.

Doney, S. C., Yeager, S. G., Danabasoglu, G., Large, W. G. & McWilliams, J. C. 2003 Modeling Global Oceanic Interannual Variability (1958-1997): Simulation Design and Model-Data Evaluation, *Technical Report TN-452+STR*, NCAR 48pp.

Doney, S. & Hecht, M. 2002 Antarctic bottom water formation and deep water chlorofluorocarbon distributions in a global ocean climate model, *J. Phys. Oceanogr.* **32**, 1642–1666.

Fekete, B., Vorosmarty, C. & Grabs, W. (1999) An improved spatially distributed runoff data set based on observed river discharge and simulated water balance, Complex Systems Research Center, U. New Hampshire.

Fung, I., Harrison, D. & Lacis, A. 1984 On the variability of the net longwave radiation at the ocean surface, *Rev. Geophys.* **22**, 177–193.

Gent, P. 1991 The heat budget of the TOGA-COARE domain in an ocean model, *J. Geophys. Res.* **96**, 3323–3330.

Gibson, J., Kallberg, P., Uppala, S., Hernandez, A., Nomura, A. & Serrano, E. 1997 ECMWF re-analysis project, 1. ERA description, *Project report series*, ECMWF.

Huffman, G., Adler, R., Arkin, P., Chang, A., Ferraro, R., Gruber, R., Janowiak, J., McNab, A., Rudolf, B. & Schneider, U. 1997 The global precipitation climatology project (GPCP) combined precipitation data set, *Bull. Amer. Meteor. Soc.* **78**, 5–20.

Hurrell, J., Caron, J., Hack, J. & Shea, D. 2003 A new sea surface temperature and sea ice boundary data set for the Community Atmosphere Model, *Geophys. Res. Lett.* pp. 0–999.

Josey, S., Kent, C. & Taylor, P. 1998 The Southampton Oceanography Centre (SOC) ocean-atmosphere heat, momentum and freshwater flux atlas, *Technical Report Report No.6*, Southampton Oceanography Centre 30pp.

Kalnay, E., Kanamitsu, M., Kistler, R., Collins, W., Deaven, D., Gandin, L., Iredell, M., Saha, S., White, G., Woollen, J., Zhu, Y., Chelliah, M., Ebisuzaki, W., Higgins, W., Janowiak, J., Mo, K., Ropelewski, C., Leetmaa, A., Reynolds, R. & Jenne, R. 1996 The NCEP/NCAR 40-Year Reanalysis Project, *Bull. Amer. Meteor. Soc.* **77**, 437–471.

Kent, E., Taylor, P., Truscott, B. & Hopkins, J. 1993 The Accuracy of Voluntary Observing Ships' Meteorological Observations–Results of the VSOP-NA, *J. Atmos. Oceanic Technol.* **10**, 591–608.

Kiehl, J. & Gent, P. 2004 The Community Climate System Model, Version Two, *J. of Climate* **17**, In Press.

Killworth, P., Smeed, D. & Nurser, A. 2000 The effects on ocean models of relaxation towards observations at the surface, *J. Phys. Oceanogr.* **30**, 160–174.

Knox, J. 1991 An assessment of the 27-year record of measured precipitation at ocean weather station "P" in the northeast Pacific Ocean, *Clim. Bull. Canadian. Met. Ocean. Soc.* **25**, 65–80.

Large, W. G., Danabasoglu, G., Doney, S. C. & McWilliams, J. C. 1997 Sensitivity to Surface Forcing and Boundary Layer Mixing in a Global Ocean Model: Annual-Mean Climatology, *J. Phys. Oceanogr.* **27**, 2418–2447.

Large, W. & Nurser, A. (2001) Ocean surface water mass transformation, *Ocean Circulation and Climate*, G. Siedler, J. Church & J. Gould (eds), number 77 in *International Geophysics Series*, Academic Press, pp. 317–336.

Levitus, S., Antonov, J. I., Boyer, T. P. & Stephens, C. 2000 Warming of the World Ocean, *Science* **287**, 2225–2229.

Levitus, S., Boyer, T., Conkright, M., Johnson, D., O'Brien, T., J.Antonov, Stephens, C. & Gelfeld, R. 1998 World Ocean Database 1998, *Atlas NES-DIS 18*, NOAA.

Lind, R. & Katsaros, K. 1986 Radiation measurements and model results from R/V Oceanographer during STREX 1980, *J. Geophys. Res.* **91**, 13308–13314.

MacDonald, A. 1998 The global ocean circulation: a hydrographic estimate and regional analysis, *Prog. Oceanogr.* **41**, 281–382.

Nurser, A., Marsh, R. & Williams, R. 1999 Diagnosing water mass formation rates from air-sea fluxes and surface mixing, *J. Phys. Oceanogr.* **29**, 1468–1487.

Payne, R. 1972 Albedo of the sea surface, *J. Atmos. Sci.* **29**, 959–970.

Perry, G., Duffy, P. & Miller, N. 1996 An extended data set of river discharges for validation of general circulation models, *J. Geophys. Res.* **101**, 21339–21349.

Rayner, N., Parker, D., Horton, E., Folland, C., Alexander, L. & Powell, D. 2003 Global analyses of SST, sea ice and night marine air temperature since the late nineteenth century, *J. Geophys. Res.* **108**, In Press.

Reynolds, R., Rayner, N., Smith, T., Stokes, D. & W.Wang 2002 An improved in situ and satellite SST analysis for climate, *J. of Climate* **15**, 1609–1625.

Rigor, I., Colony, R. & Martin, S. 1999 Variations in Surface Air Temperature Observations in the Arctic, 1979 - 1997, *J. of Climate* **12**, xx–yy.

Roll, H. V. 1965 Physics of the Marine Atmosphere, Academic Press, New York 426pp.

Rosati, A. & Miyakoda, K. 1988 A general circulation model for upper ocean simulation, *J. Phys. Oceanogr.* **18**, 1601–1626.

Schmidt, G., Bitz, C. M., Mikolajewicz, U. & Tremblay, L. 2004 Ice-ocean boundary conditions for coupled models, *Ocean Modelling* **7**, 59–74.

Serreze, M. & Hurst, C. 2000 Representation of mean Arctic precipitation from NCEP-NCAR and ERA reanalyses, *J. of Climate* **13**, 182–201.

Silva, A. D., Young, C. & Levitus, S. 1994 Atlas of surface marine data 1994, *NOAA Atlas NESDIS 6. (6 volumes)* pp. U.S. Dept. of Commerce, NODC, User services branch, NOAA/NESDIS/ E/OC21.

Smith, S. & Dobson, F. 1984 The heat budget at Ocean Weather Station Bravo, *Atmos. Oceans* **22**, 1–22.

Smith, S. R., Legler, D. M. & Verzone, K. V. 2001 Quantifying Uncertainties in NCEP Reanalyses Using High-Quality Research Vessel Observations, *J. of Climate* **14**, 4062–4072.

Spencer, R. W. 1993 Global Oceanic Precipitation from the MSU during 1979-91 and Comparisons to Other Climatologies, *J. of Climate* **6**, 1301–1326.

Steele, M., Morley, R. & Ermold, W. 2001 PHC: A global ocean hydrography with a high quality Arctic Ocean, *J. of Climate* **14**, 2079–2087.

Taylor(ed.), P. 2000 Final Report of the Joint WCRP/SCOR Working Group on Air-Sea Fluxes: Intercomparison and validation of ocean-atmosphere energy flux fields, *WCRP-112, WMO/TD-No.1036*, World Climate Research Programme 303pp.

Timokhov, L. & Tanis, F. 1997 Environmental Working Group Joint U.S.-Russian Atlas of the Arctic Ocean - Winter Period, *Technical report*, Environmental Research Institute of Michigan in association with the National Snow and Ice Data Center, Ann Arbor, MI CD-ROM.

Timokhov, L. & Tanis, F. 1998 Environmental Working Group Joint U.S.-Russian Atlas of the Arctic Ocean - Summer Period, *Technical report*, Environmental Research Institute of Michigan in association with the National Snow and Ice Data Center, Ann Arbor, MI CD-ROM.

UNESCO 1985 Discharge of selected rivers of the world, vol. I, II, III (parts I, II, III, IV), UNESCO, Paris.

van Loon, H. & Rogers, J. 1984a Interannual variations in the half-yearly cycle of pressure gradients and zonal wind at sea level on the Southern Hemisphere, *Tellus* **36**, 76–86.

van Loon, H. & Rogers, J. 1984b The yearly wave in pressure and zonal geostrophic wind at sea level on the Southern Hemisphere and its interannual variability, *Tellus* **36**, 348–354.

Wang, W. & McPhaden, M. J. 2001 What is the mean seasonal cycle of surface heat flux in the equatorial Pacific?, *J. Geophys. Res.* **106**, 837–857.

Wijffels, S. (2001) Ocean transport of freshwater, *Ocean Circulation and Climate*, G. Siedler, J. Church & J. Gould (eds), number 77 in *International Geophysics Series*, Academic Press, pp. 475–488.

Xie, P. & Arkin, P. A. 1996 Analyses of Global Monthly Precipitation Using Gauge Observations, Satellite Estimates, and Numerical Model Predictions, *J. of Climate* **9**, 840–858.

Yang, D. 1999 An improved precipitation climatology for the Arctic Ocean, *Geophys. Res. Lett.* **26**, 1625–1628.

Yeager, S. & Large, W. 2004 Late winter generation of spiciness on subducted isopycnals, *J. Phys. Oceanogr.* **24**, In Press.

Zhang, Y. C., Rossow, W. B., Lacis, A. A., Oinas, V. & Mishchenko, M. I. 2004 Calculation of radiative flux profiles from the surface to top-of-atmosphere based on ISCCP and other global datasets: Refinements of the radiative transfer model and the input data, *J. Geophys. Res.* **27**, submitted.
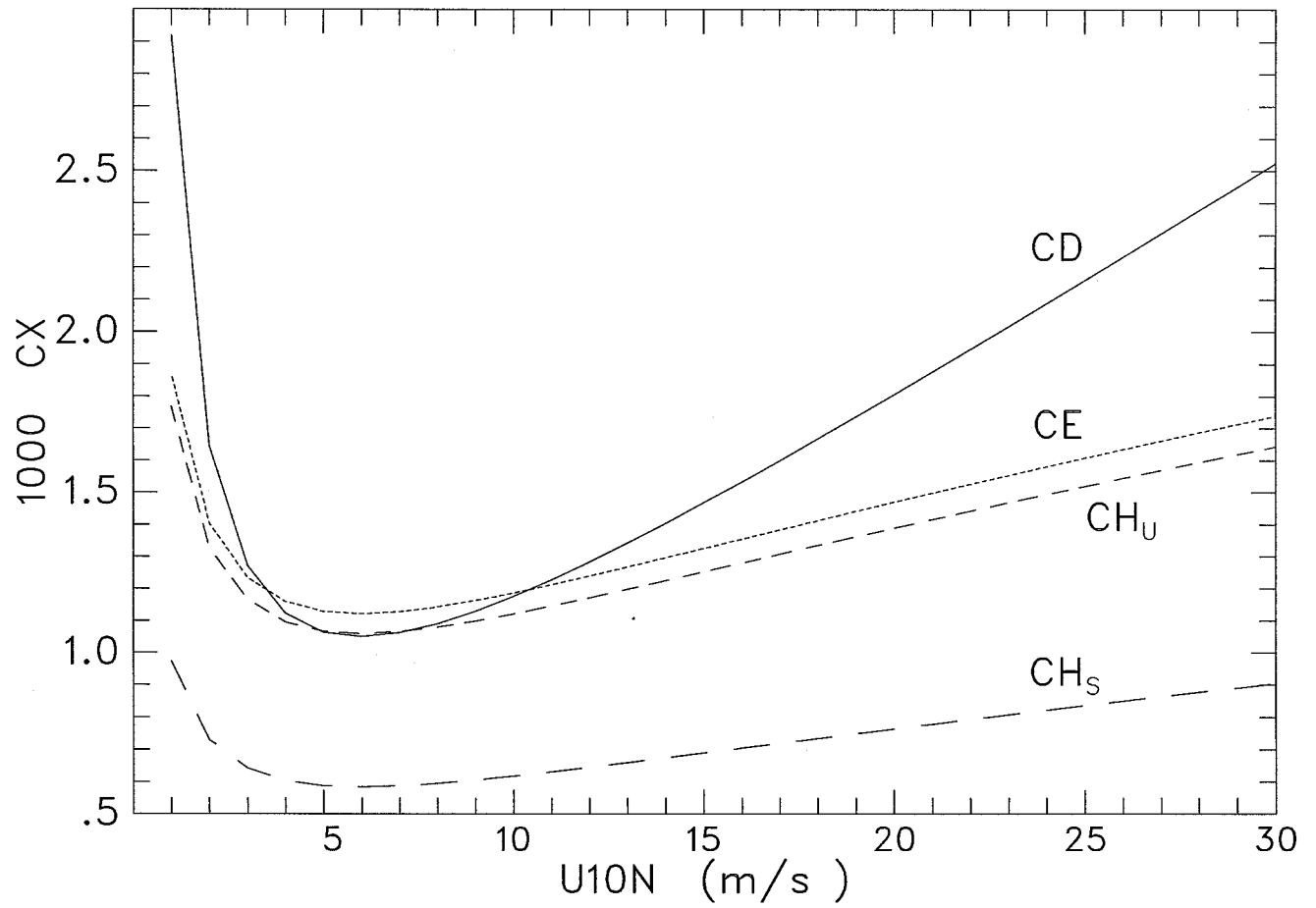
Figure 1: Bulk transfer coefficients as function of neutral 10 meter wind speed for drag, C_D, evaporation, CE, and sensible heat both in unstable, CH_U, and stable, CH_S, atmospheric stratification.
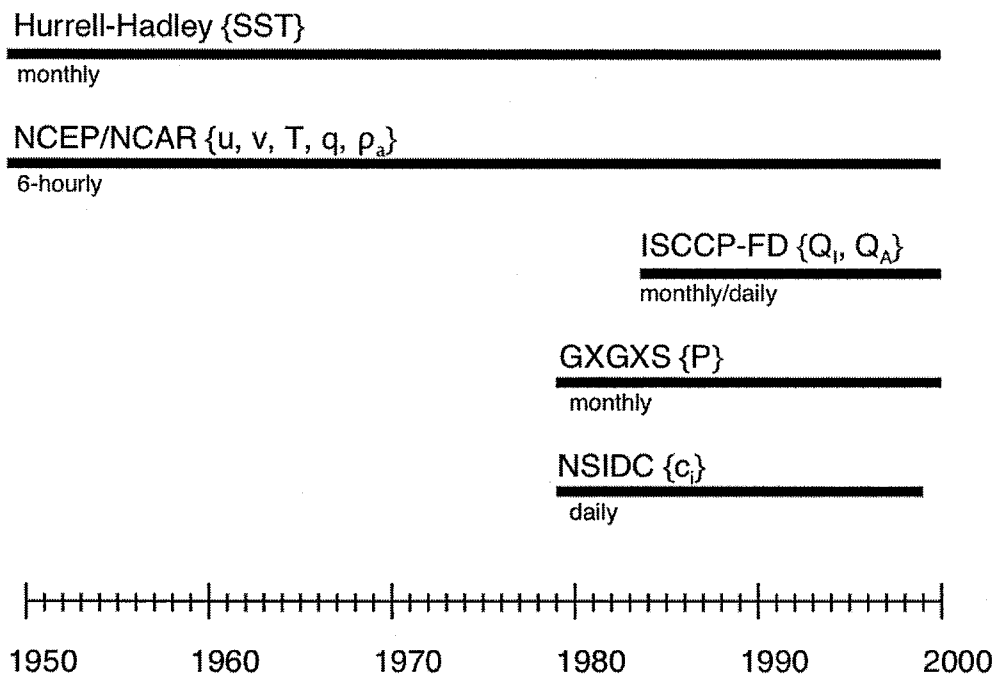
Figure 2: Timeline showing the availability forcing data sets and their frequency. Various precipitation data sets are available from 1979 to 2000.
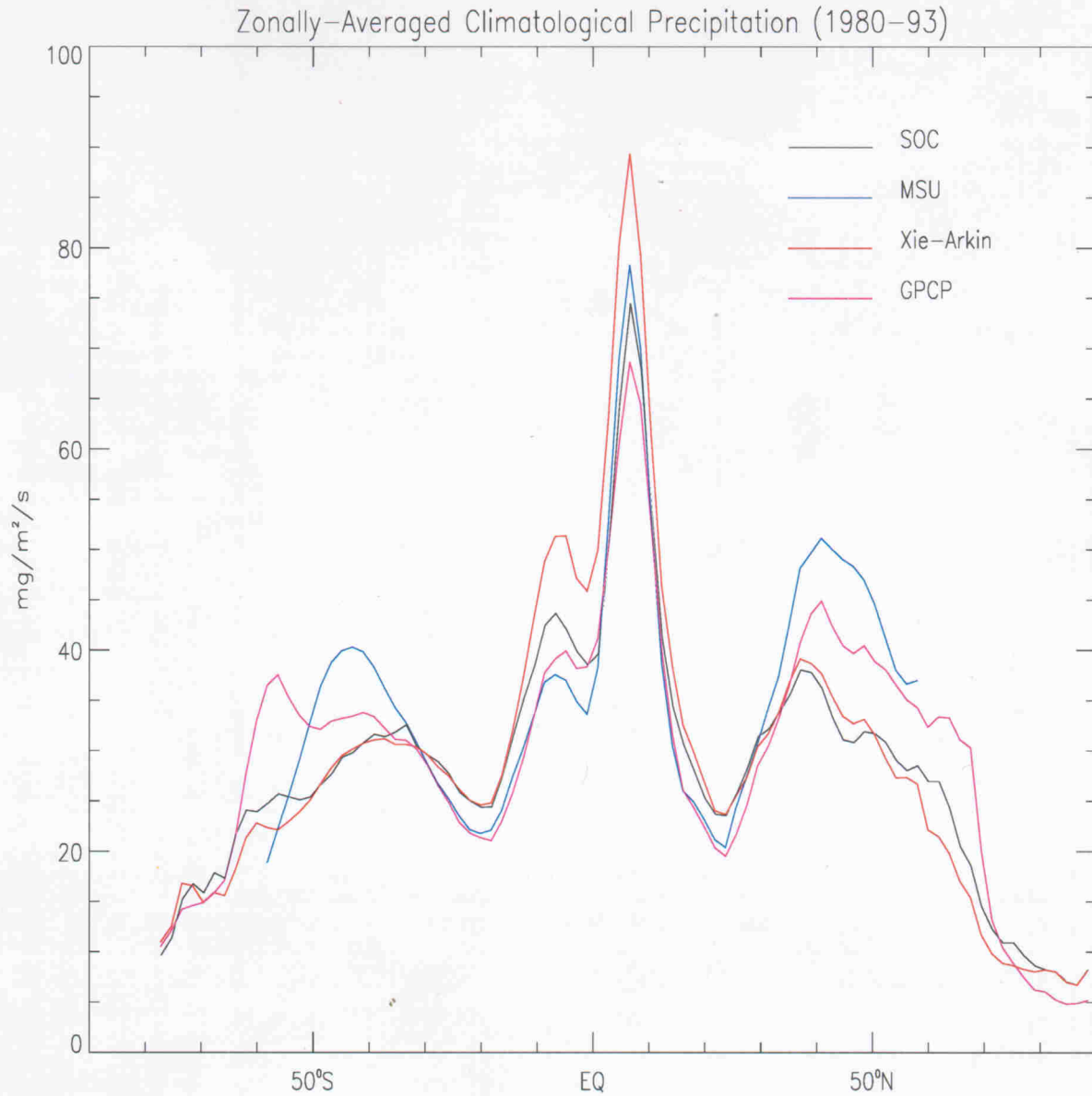
Figure 3: Comparison of climatological zonal mean precipitation over the ocean from four data sets; MSU, Xie-Arkin, SOC and GPCP, on their original grids.
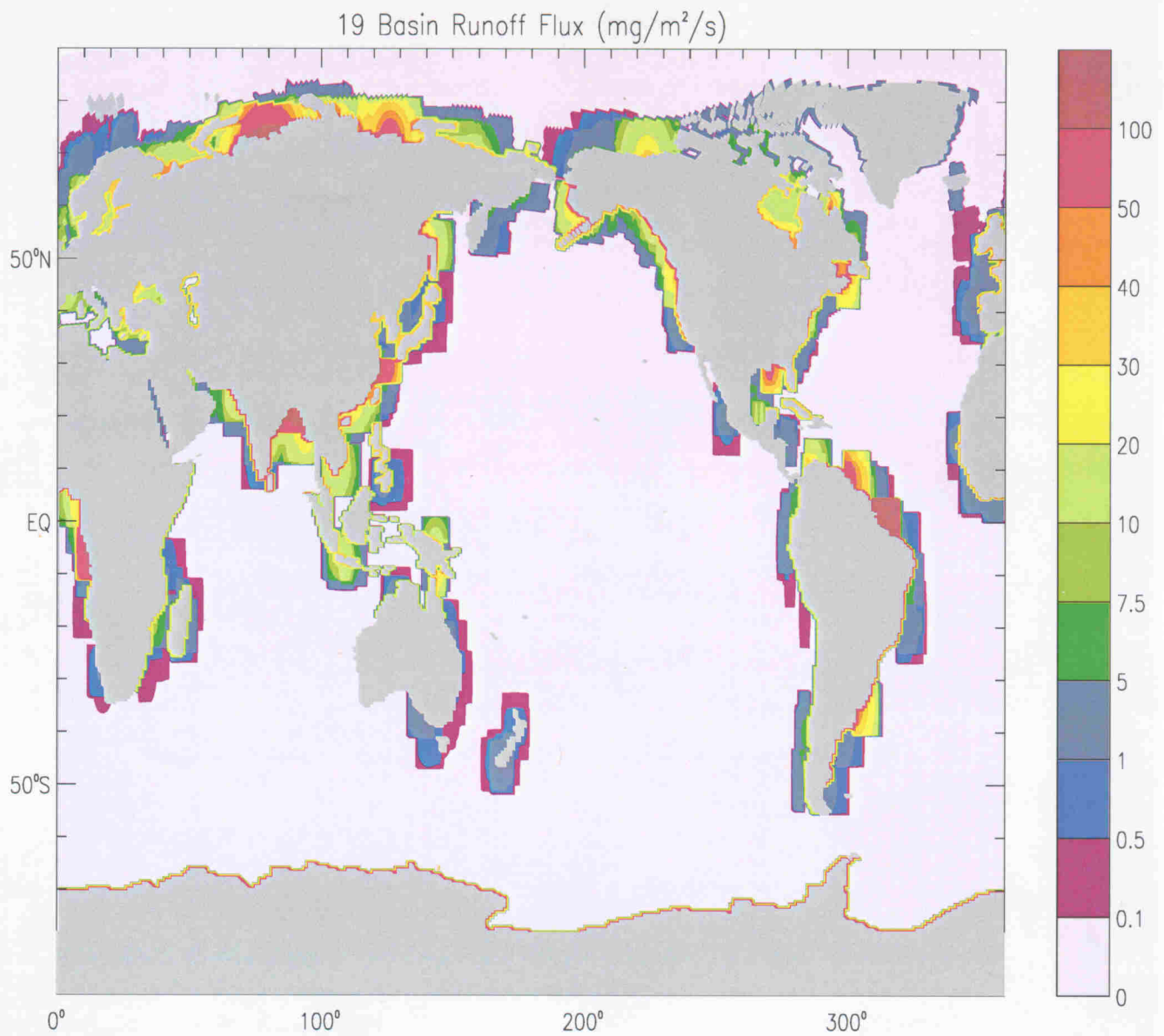
Figure 4: Distribution of the freshwater flux due to climatological runoff from continents and islands. The flux unit of $1mg/m^2/s$ ($0.0864mm/day \approx 31mm/year$) is used, because it contributes to the surface density flux an amount approximately equivalent to a heat flux of 1 W/m^2.
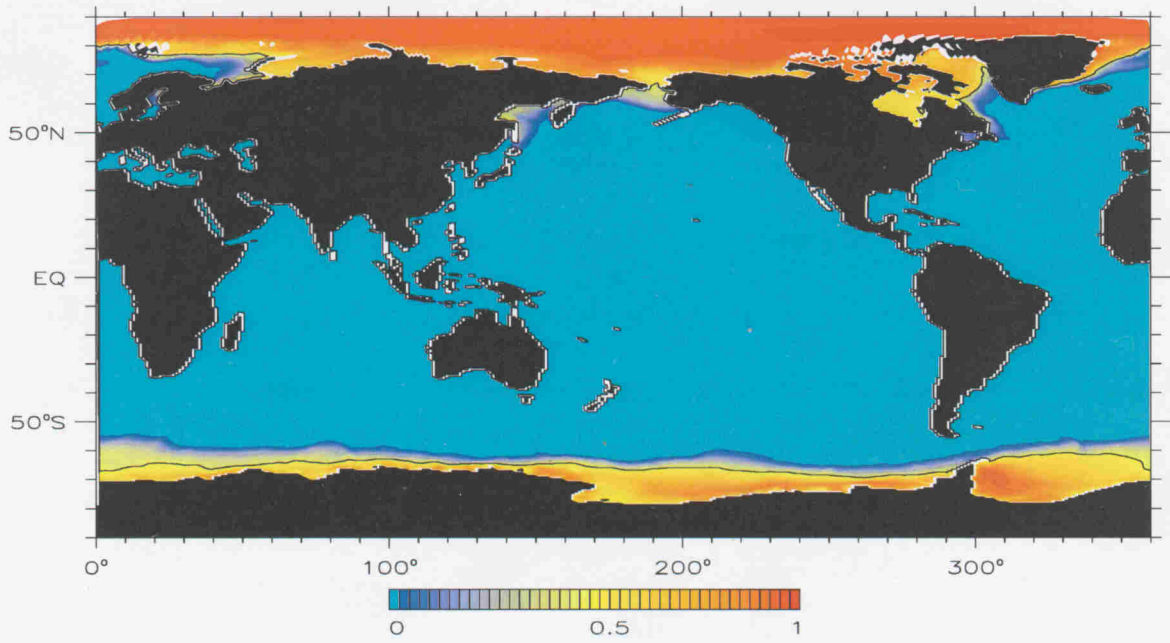
Figure 5: Climatological distribution of annual mean NSIDC sea-ice concentration, 1979–1999, as a fraction of the non-land area.
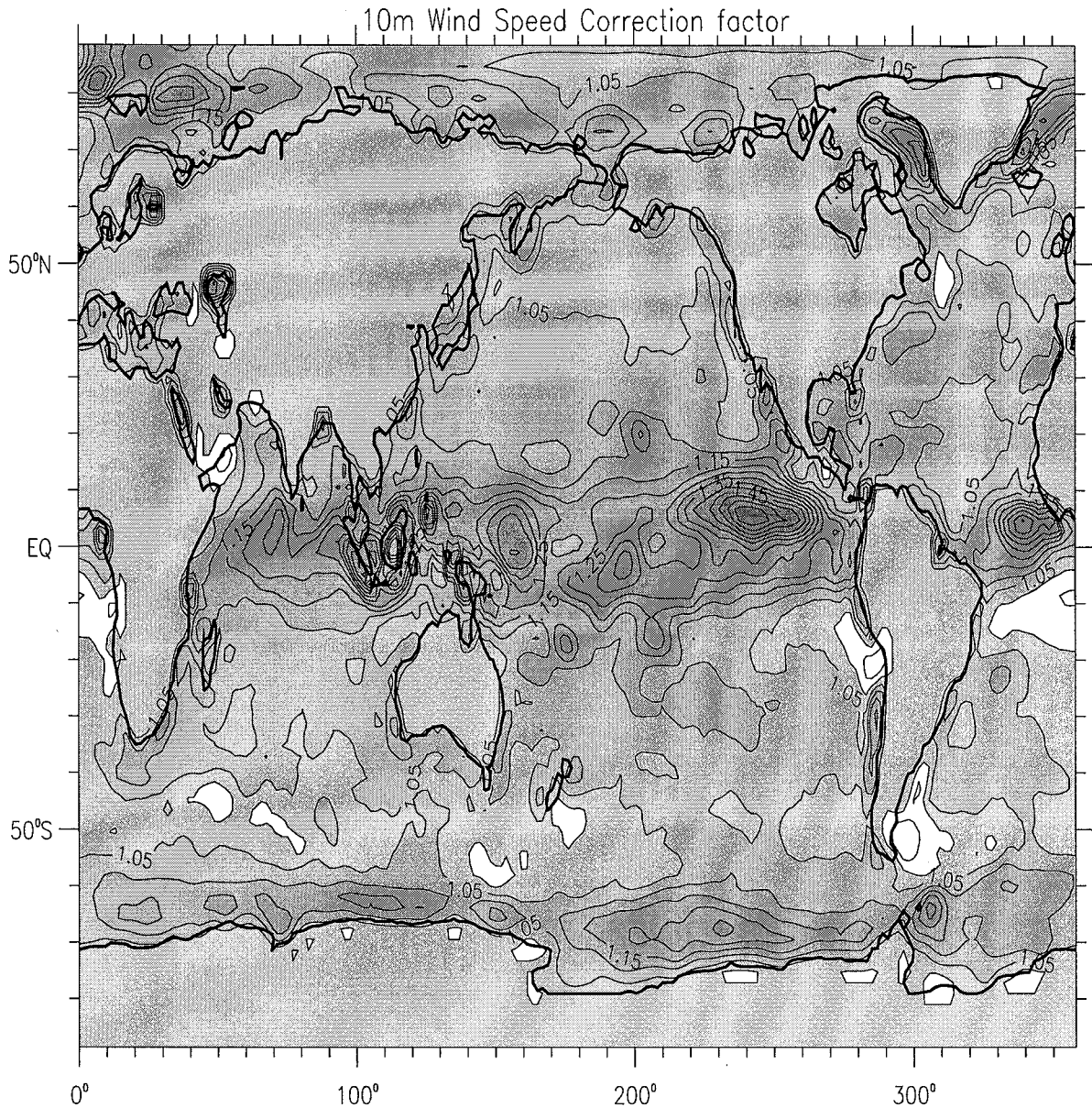
Figure 6: Ratio of two-year (2000-2001) mean QSCAT and NCEPR wind speeds. Contour interval is 0.05. The ratio has been smoothed once with a 3x3 box filter. Values above 1 are shaded.

NCEP $\langle\gamma\rangle_{1984-2000}$ — SOC $\langle\gamma\rangle_{clim}$

contoured by 2%
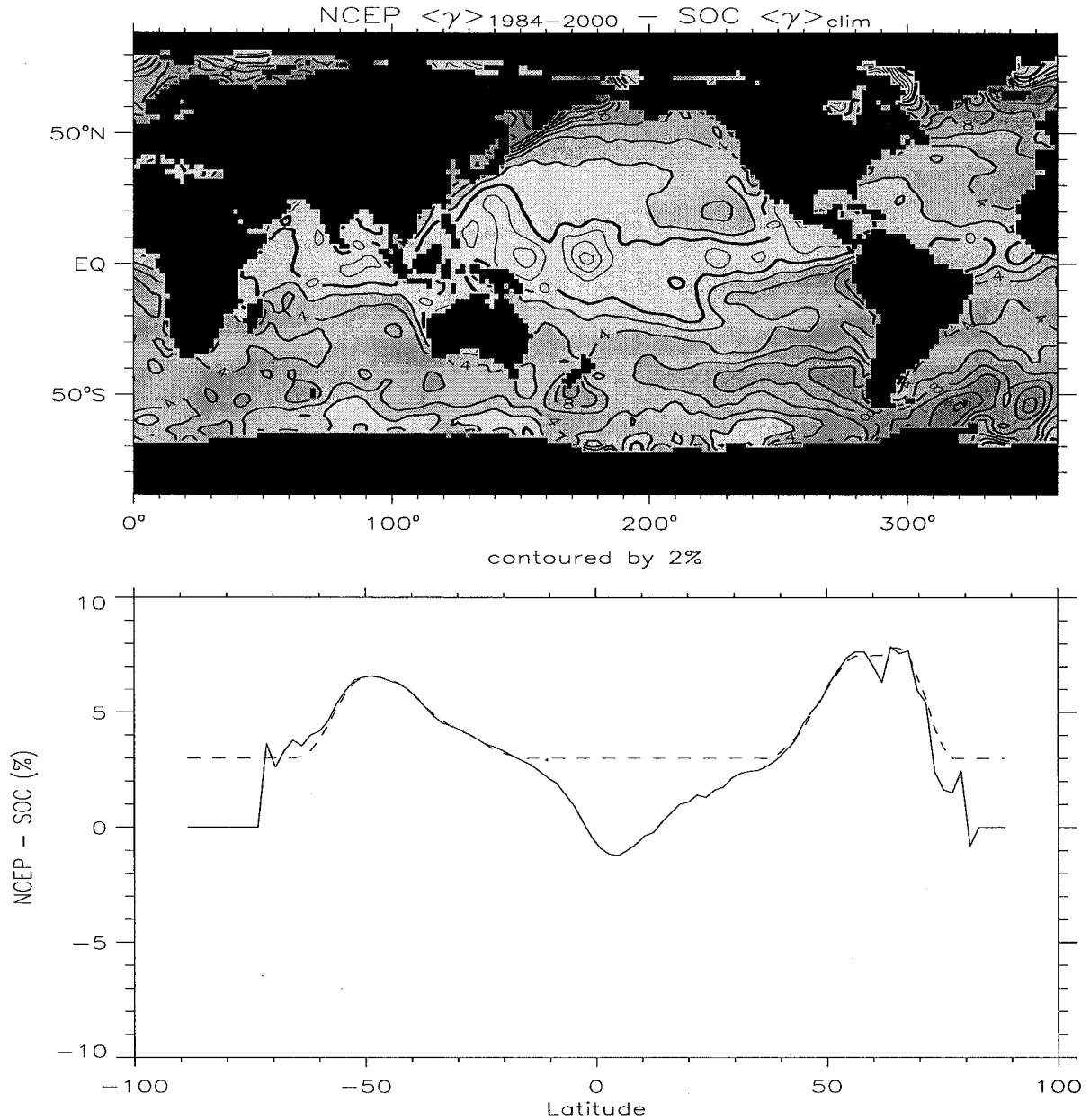
Figure 7: Comparison of NCEP/NCAR Reanalysis relative humidity with Southampton Oceanography Center (SOC) climatology as a mean difference (top panel) and as a zonally-averaged mean difference (bottom panel). Humidity values and differences are in %. The dashed line in the bottom panel shows the modified, smoothed version of the zonal-average difference used for correcting NCEP relative humidity as a function of latitude.

69
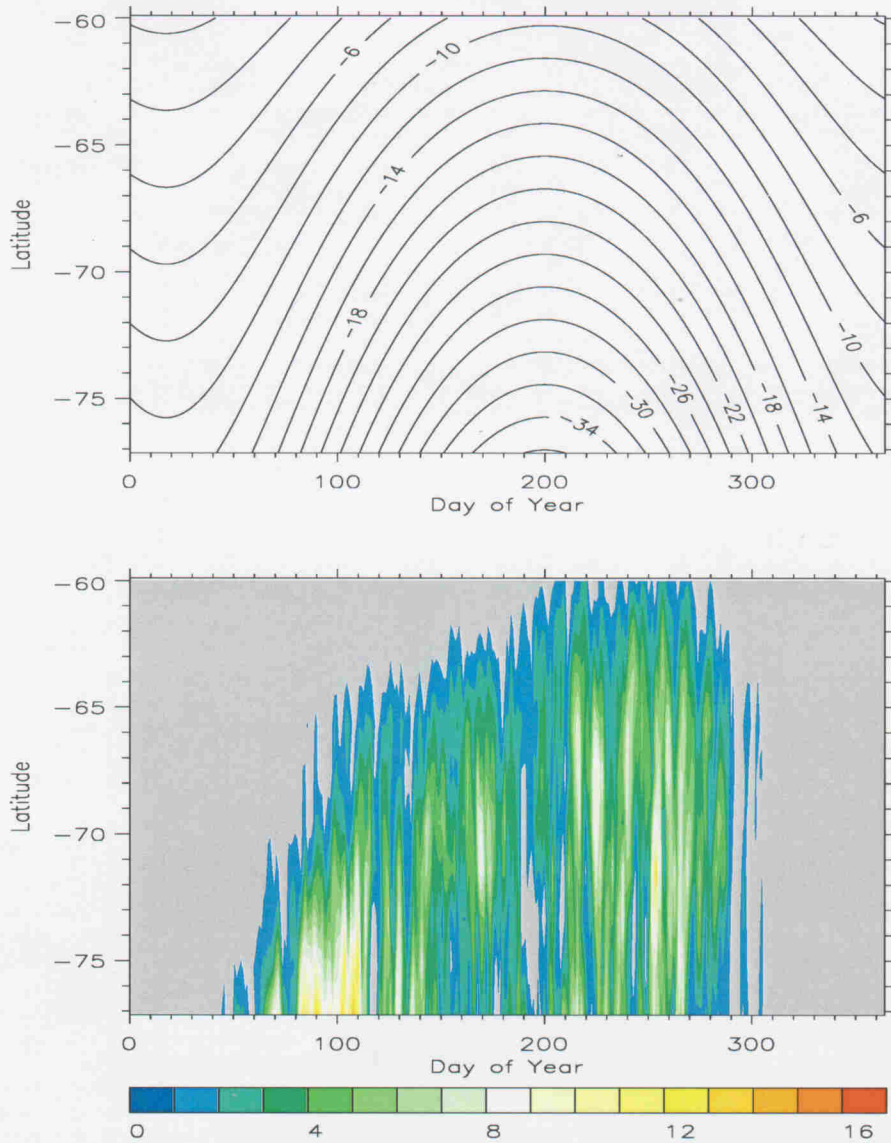
Figure 8: Top panel: Seasonal fit to station air temperature data ($^\circ C$) for the Antarctic that is used a lower limit of NCEP air temperatures. Bottom Panel : An example from 1990 of the zonally-averaged correction ($^\circ C$) applied to NCEP air temperature throughout a year.

70
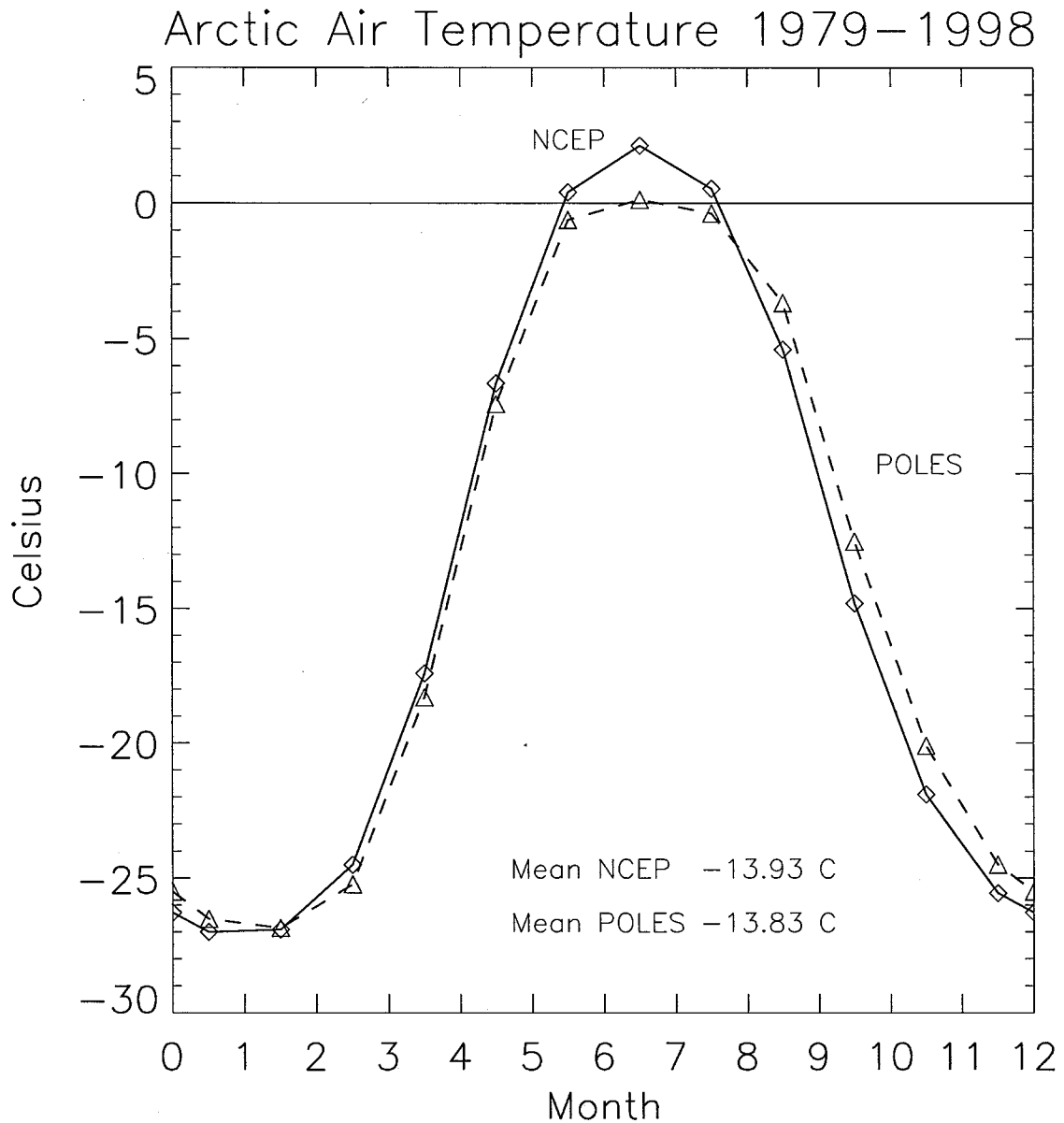
Figure 9: Climatological (1979–1998) seasonal cycle of monthly mean air temperature over the Arctic cap north of $70°N$ from NCEP/NCAR reanalysis (solid) and POLES (dashed). The annual means are $-13.93°C$ and $-13.83°C$, respectively.

71
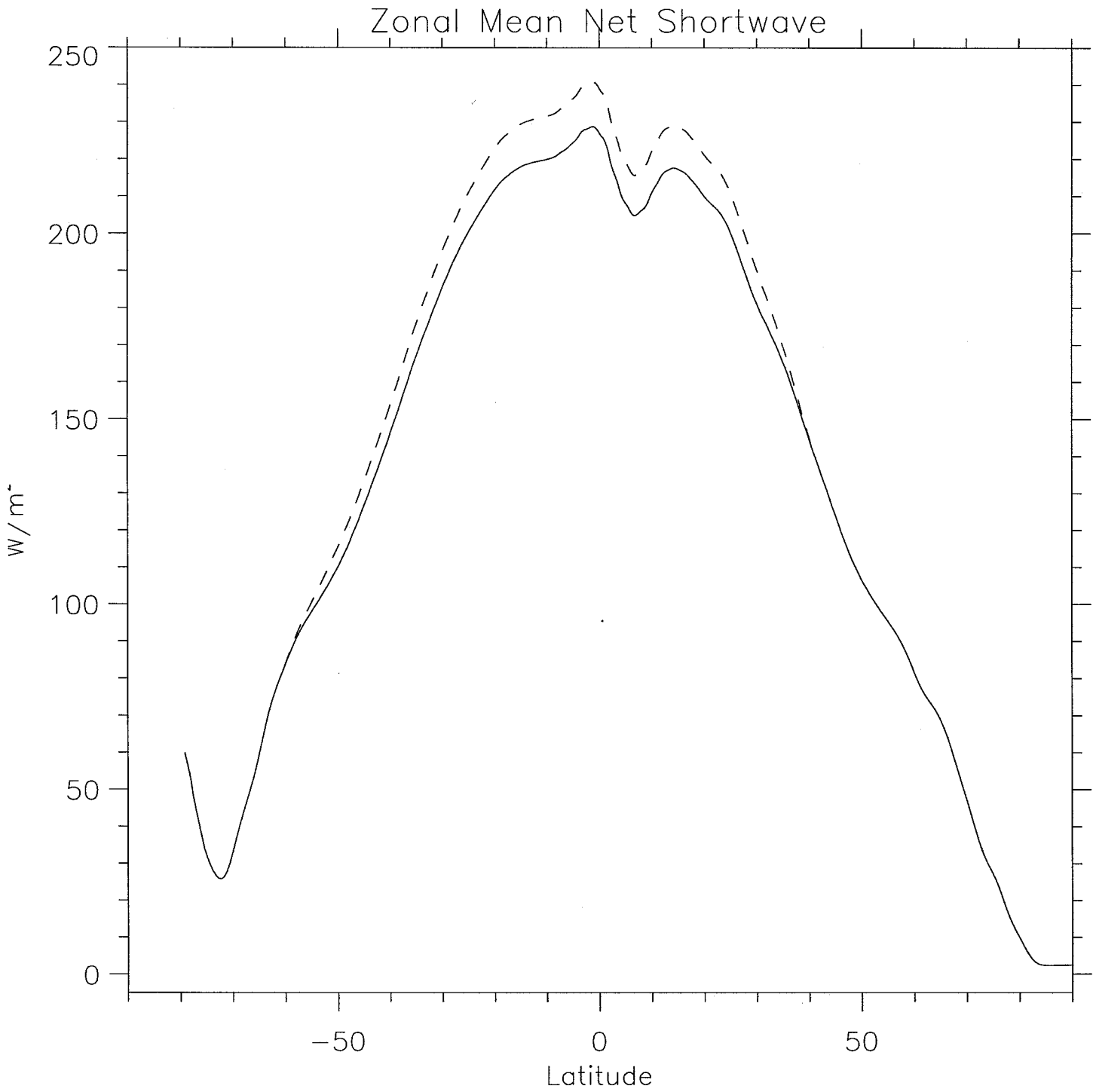
Figure 10: Climatological (1984-2000) zonal mean net shortwave radiation from the GISS dataset before (dashed) and after (black) correcting.
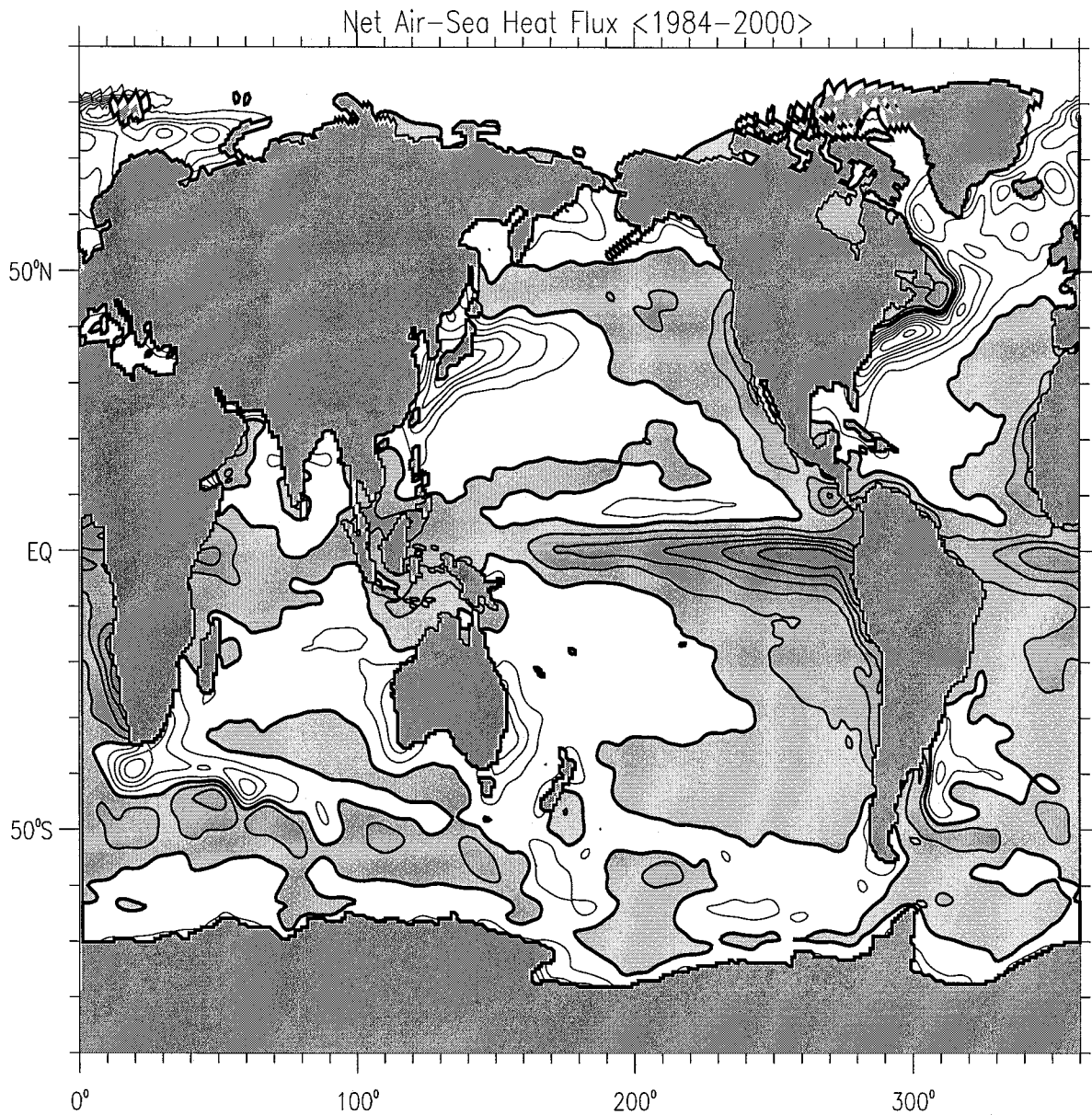
Figure 11: Climatological (1984-2000) mean net air-sea heat flux contoured at 25 W/m^2 intervals. A 5x5-point boxcar smoother has been applied twice. Shaded regions indicate positive net flux into the ocean. The net global area-averaged heat flux imbalance is 1.02 W/m^2.
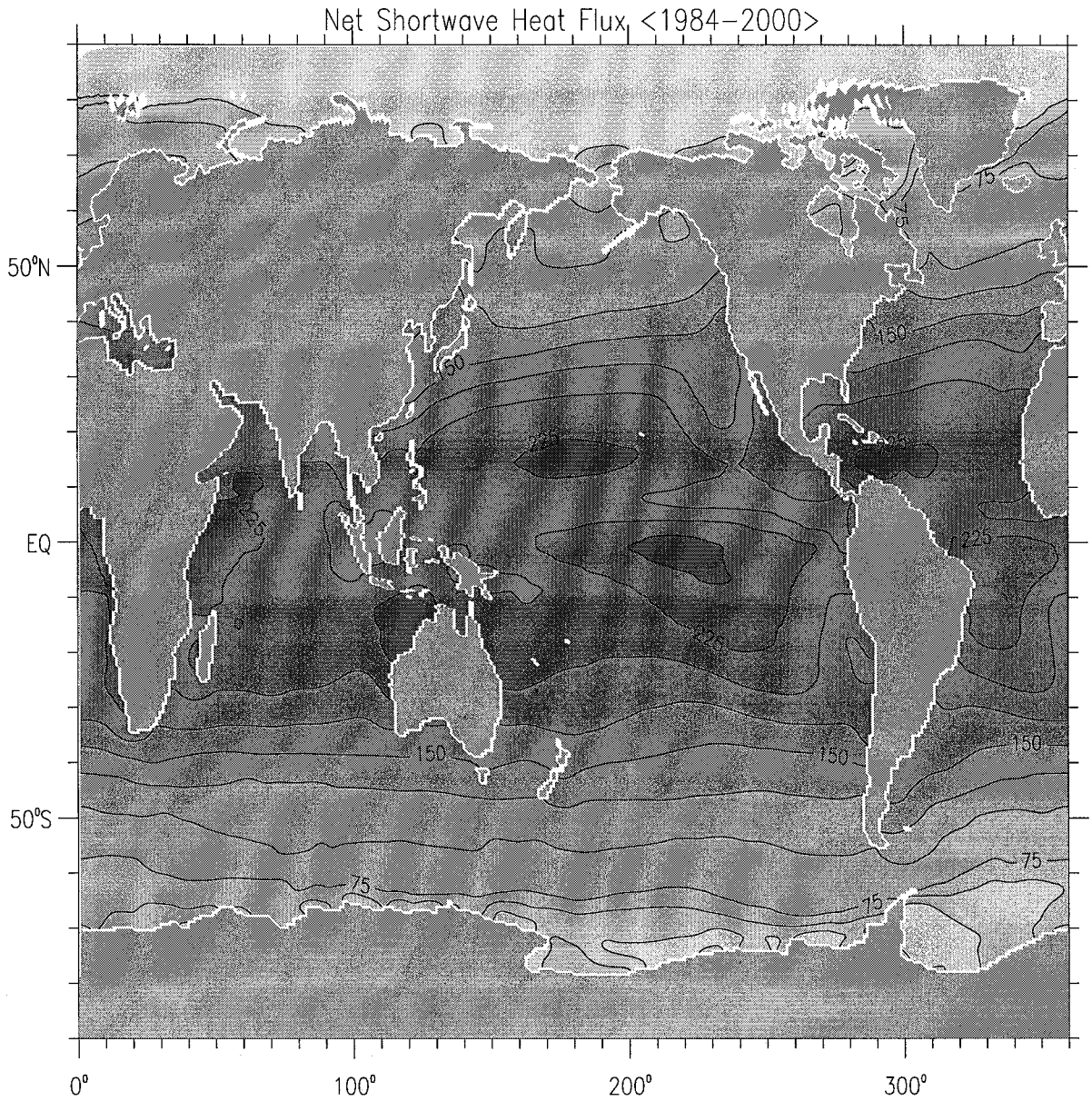
Figure 12: a) Climatological (1984-2000) mean net shortwave heat flux contoured at 25 W/m^2. A 5x5-point boxcar smoother has been applied twice.
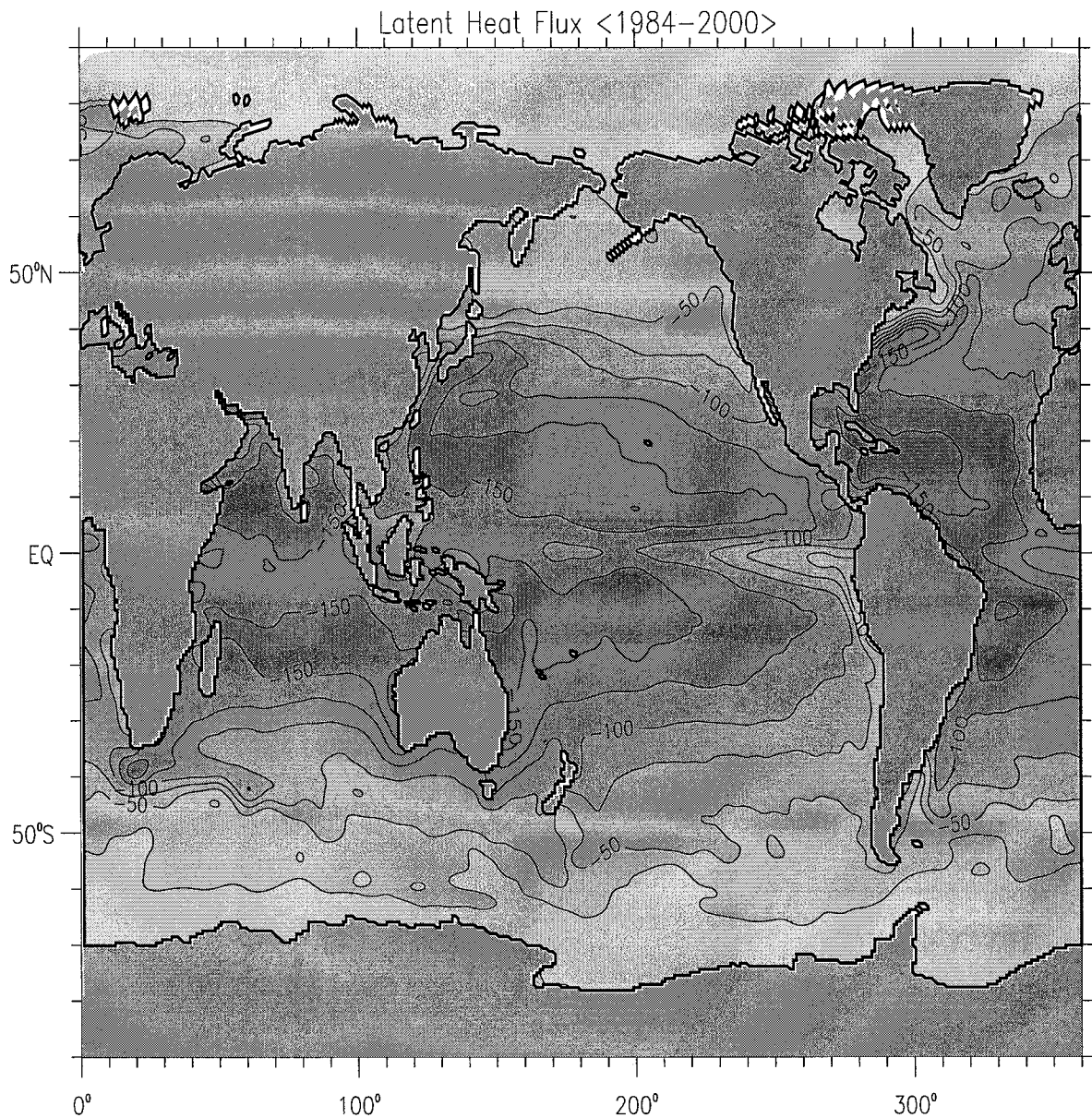
Figure 12: b) Climatological (1984-2000) mean latent heat flux contoured at 25 W/m^2. A 5x5-point boxcar smoother has been applied twice. (Darker shader indicates more negative values).
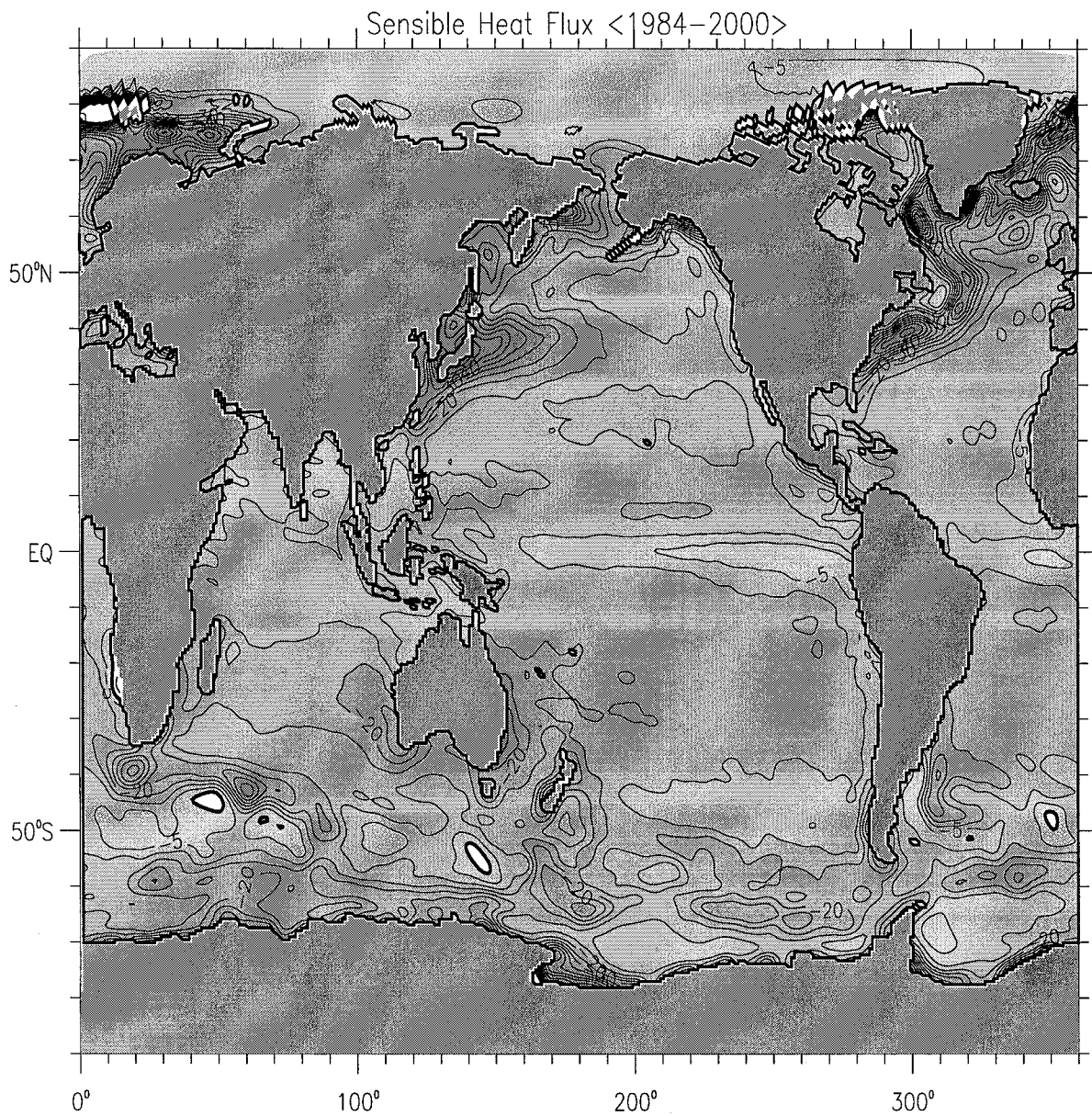
Figure 12: c) Climatological (1984-2000) mean sensible heat flux contoured at 5 W/m^2. A 5x5-point boxcar smoother has been applied twice. (Darker shading indicates more negative values).
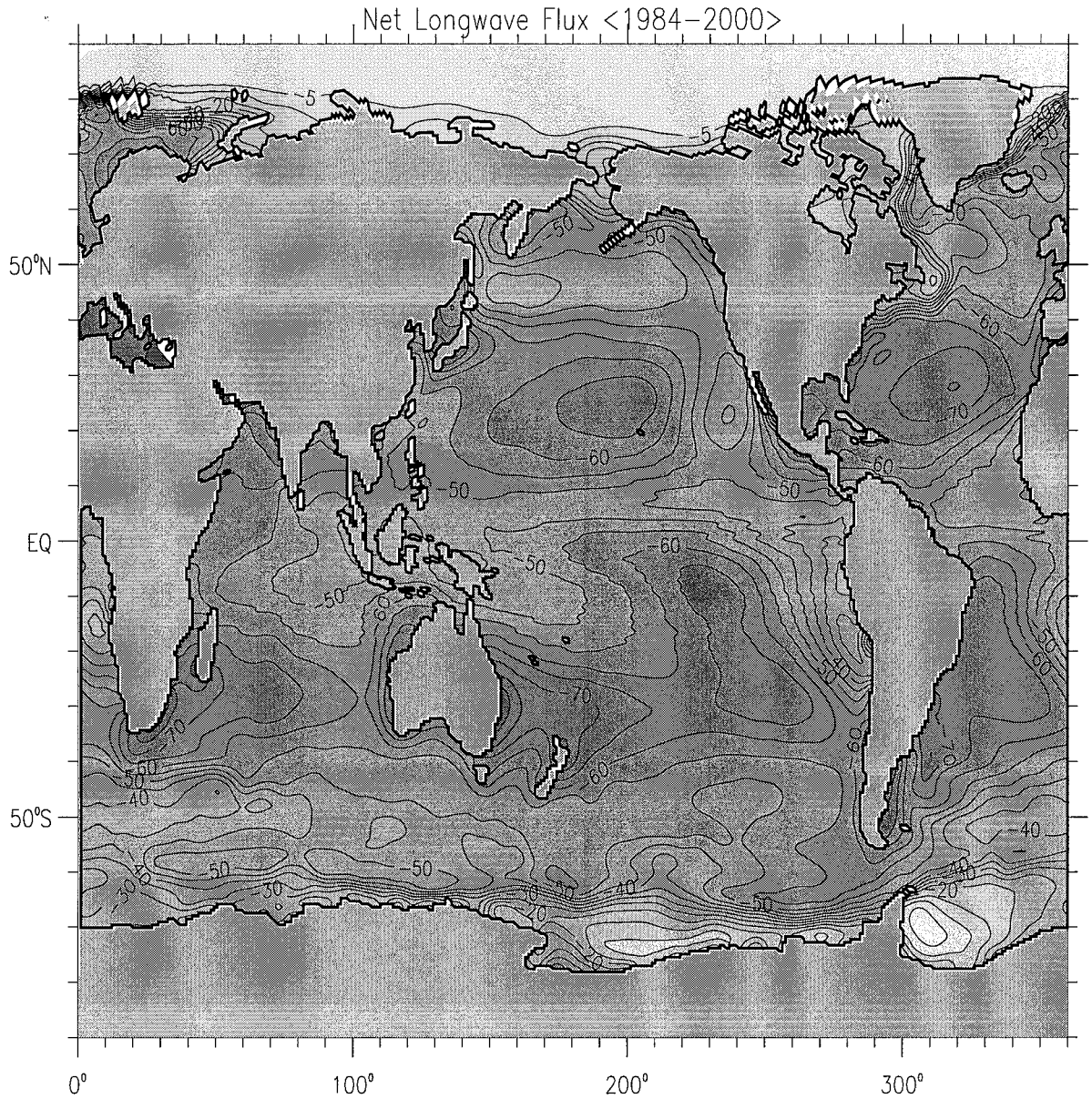
Figure 12: d) Climatological (1984-2000) mean net longwave heat flux contoured at 5 W/m^2. A 5x5-point boxcar smoother has been applied twice. (Darker shader indicates more negative values).
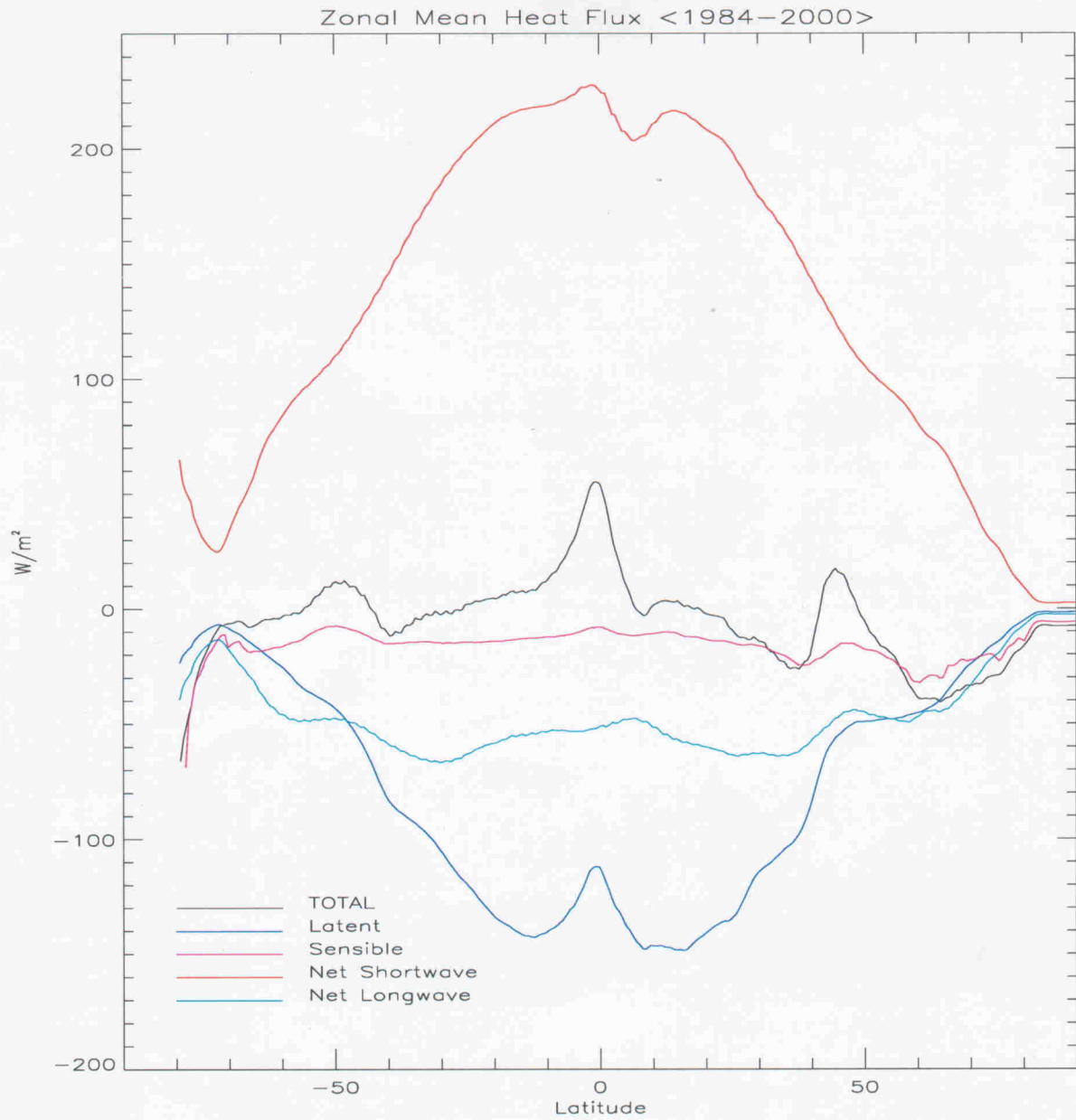
Figure 13: Climatological (1984-2000) zonal mean of the total heat flux (W/m^2), and its turbulent and radiative components, from the ocean model grid.
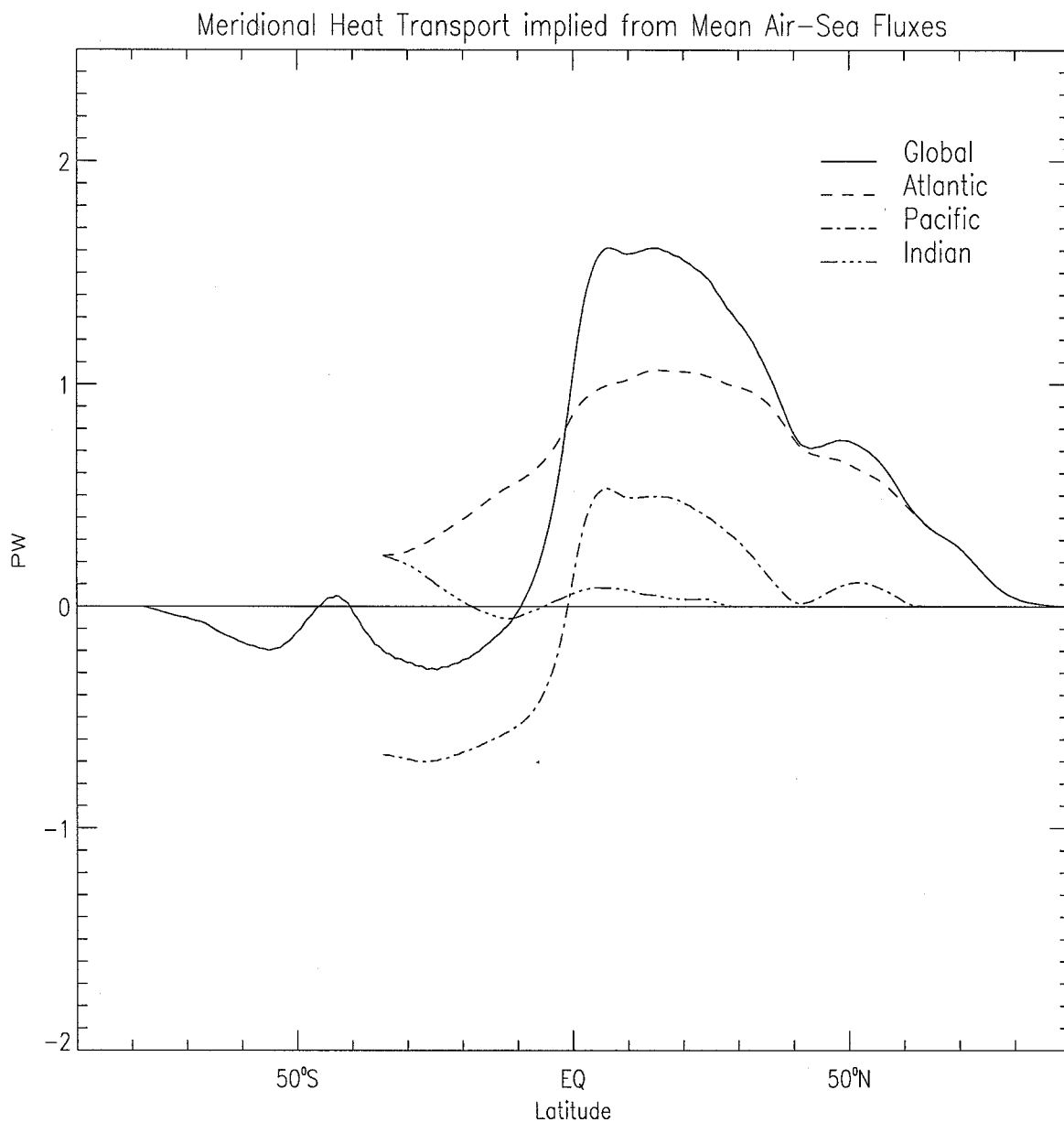
Figure 14: Climatological (1984-2000) meridional heat transport implied from mean air-sea fluxes (assuming zero ocean heat storage). Adjustment for the global heat flux imbalance is applied prior to calculation, so that the transports at the North Pole and the Antarctic coast are both zero.
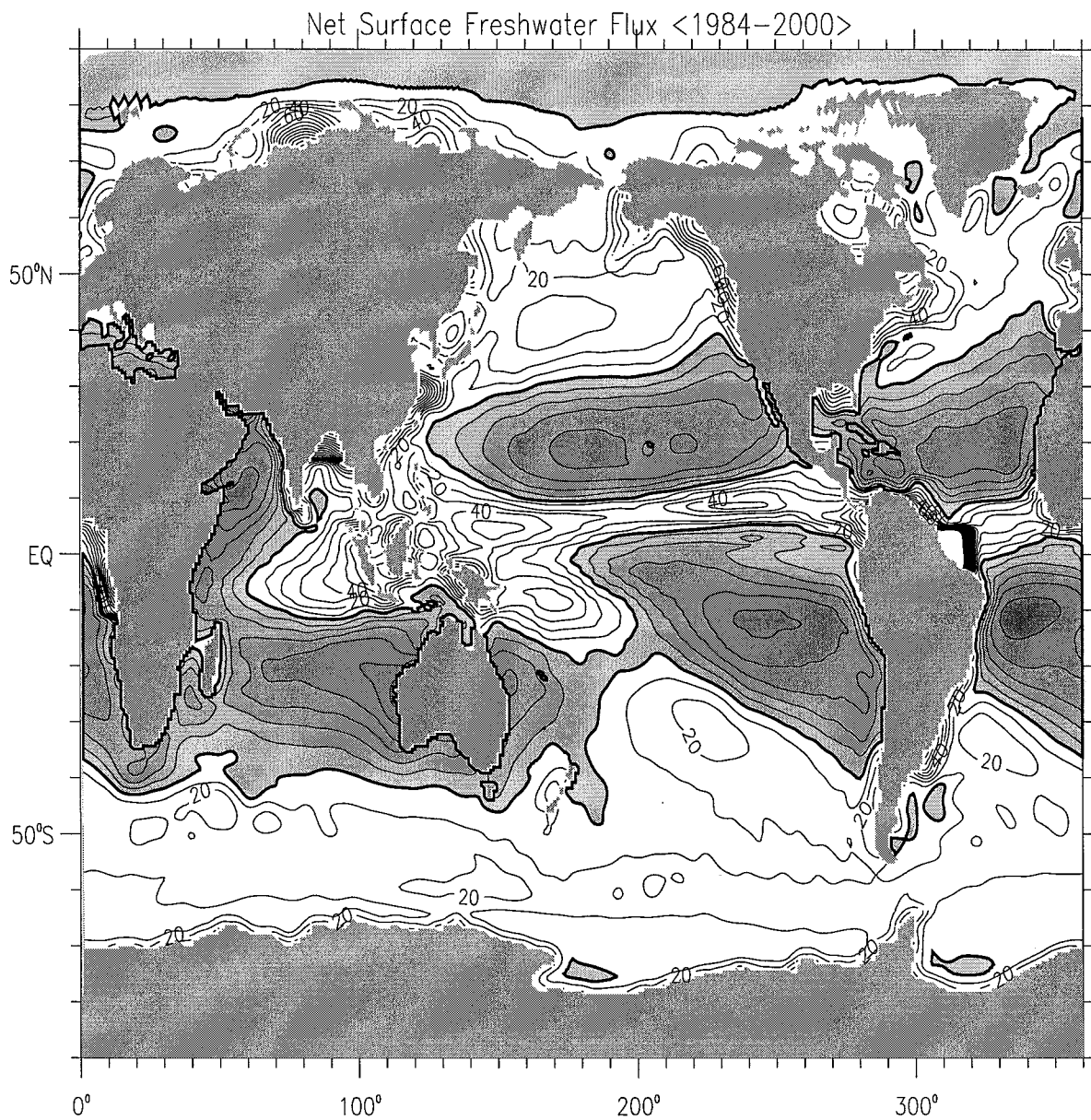
Figure 15: Climatological (1984-2000) mean net freshwater flux (precip+evap+runoff). Contour interval is 10 $mg/s/m^2$, up to abs(100). Shaded regions indicate negative net flux into the ocean. A boxcar smoother has been applied twice.
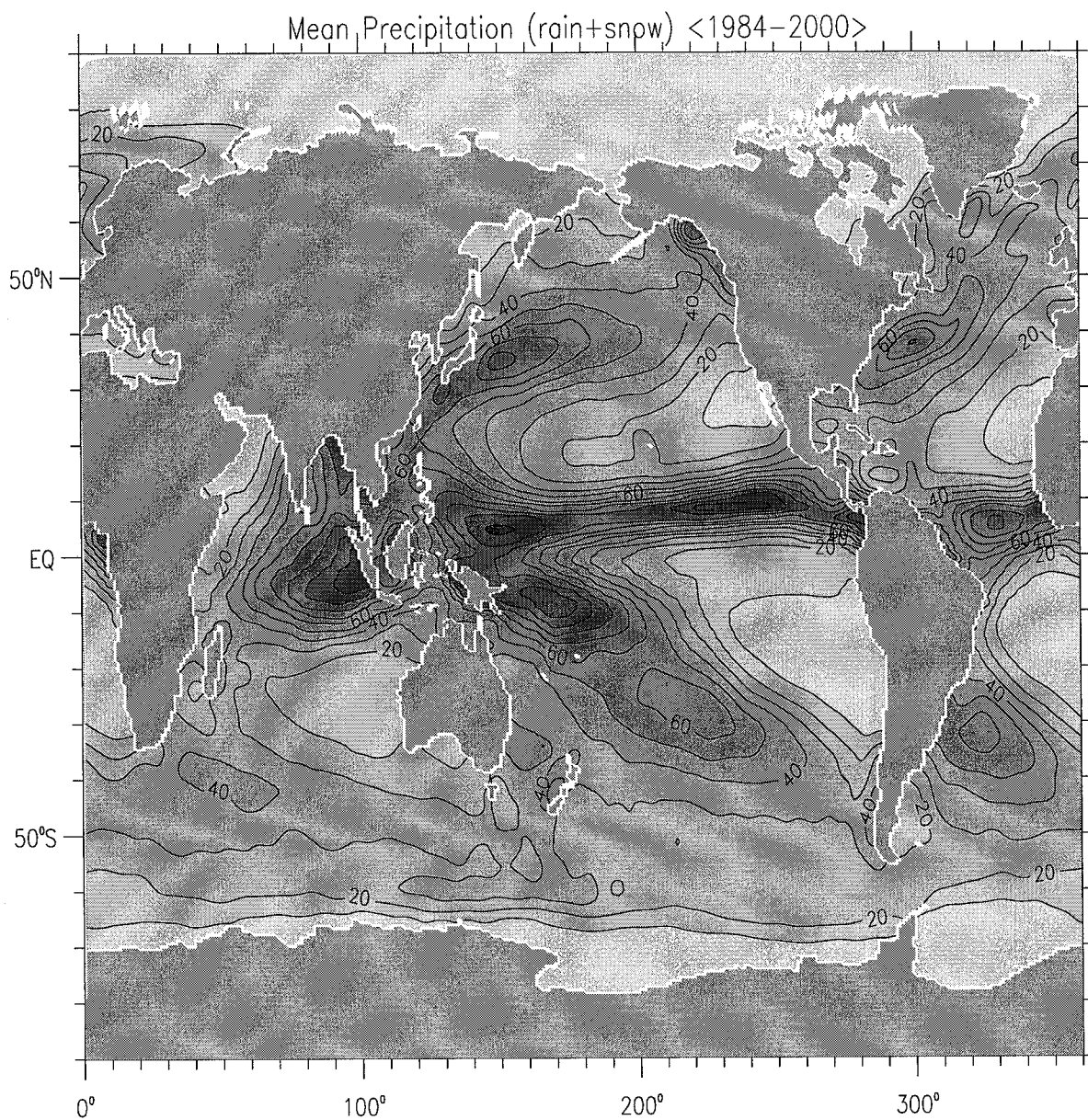
Figure 16: a) Climatological (1984-2000) mean precipitation flux (rain+snow). Contour interval is 10 $mg/s/m^2$. A boxcar smoother has been applied twice. Darker shading indicates more positive flux.
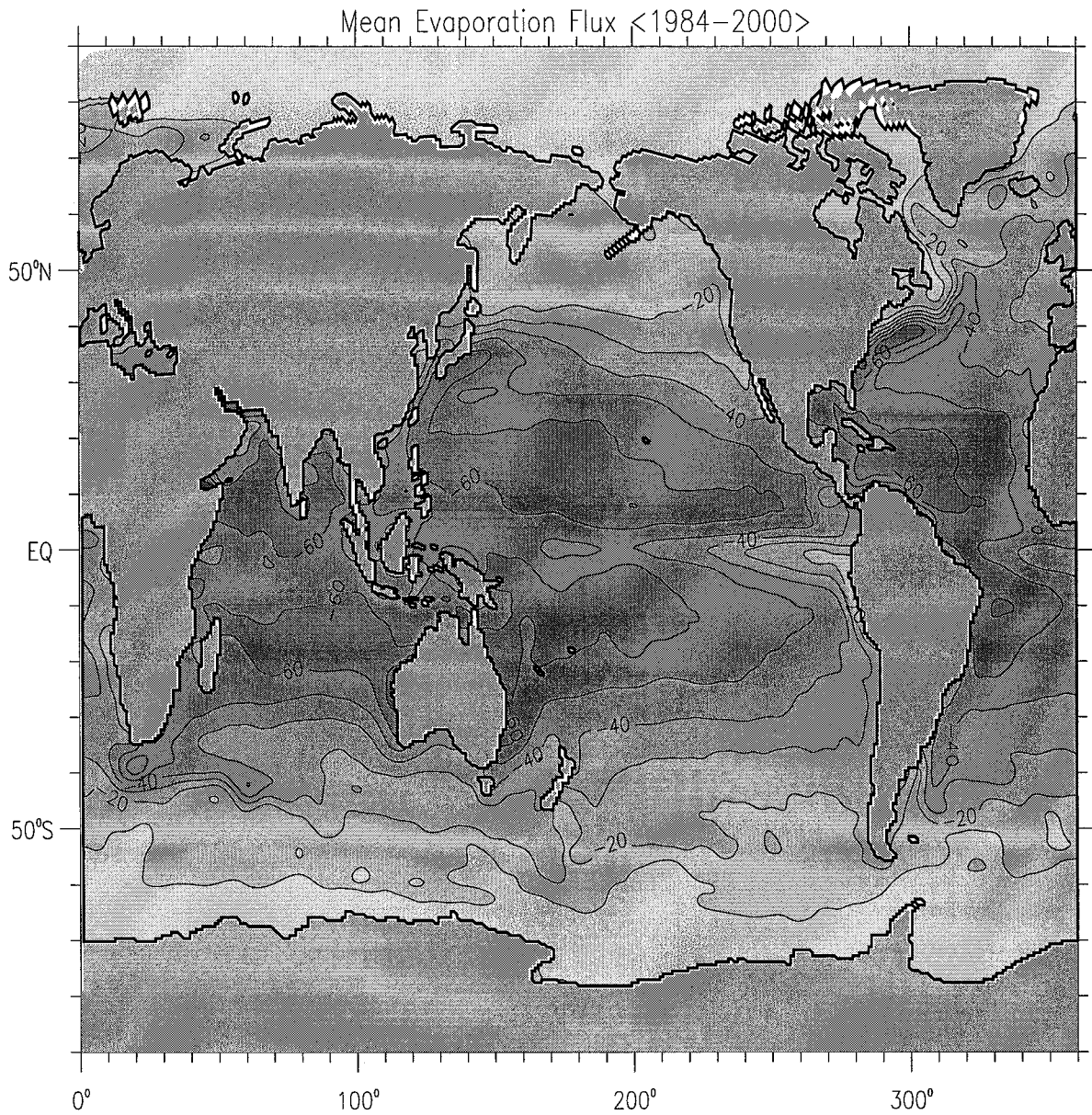
Figure 16: b) Climatological (1984-2000) mean evaporation flux in $mg/s/m^2$, which differs from the latent heat flux in W/m^2 by about a factor of 2.5. The contour interval is 10 $mg/s/m^2$, so the contours nearly align with the $25W/m^2$ contours of the latent heat flux. A boxcar smoother has been applied twice. Darker shading indicates more negative flux.
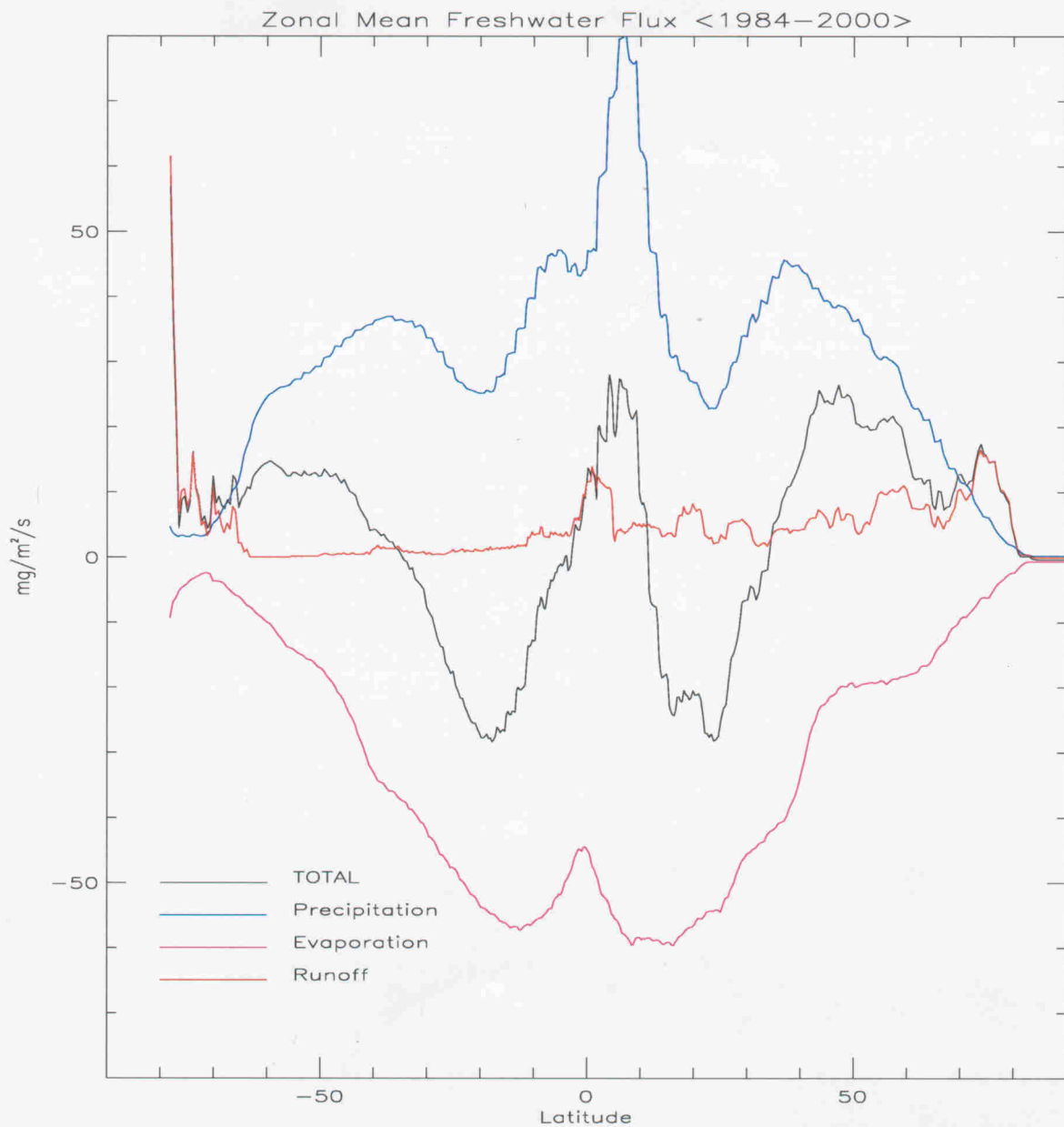
Figure 17: Climatological (1984-2000) zonal mean air-sea freshwater flux and its components: precipitation (rain+snow), evaporation, and river runoff.
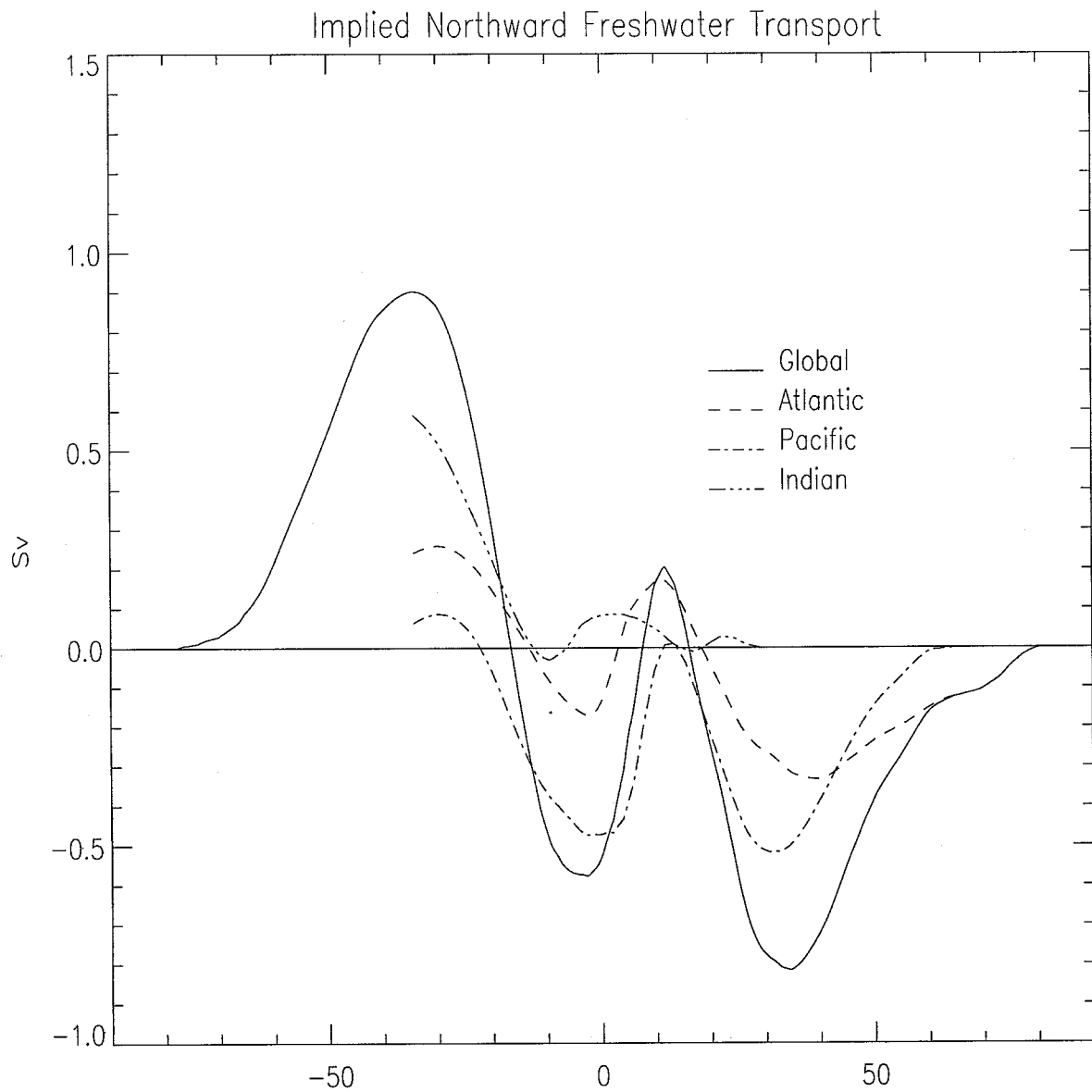
Figure 18: Climatological (1984-2000) mean northward freshwater transport implied from the net surface freshwater flux (assuming zero ocean salinity trend).
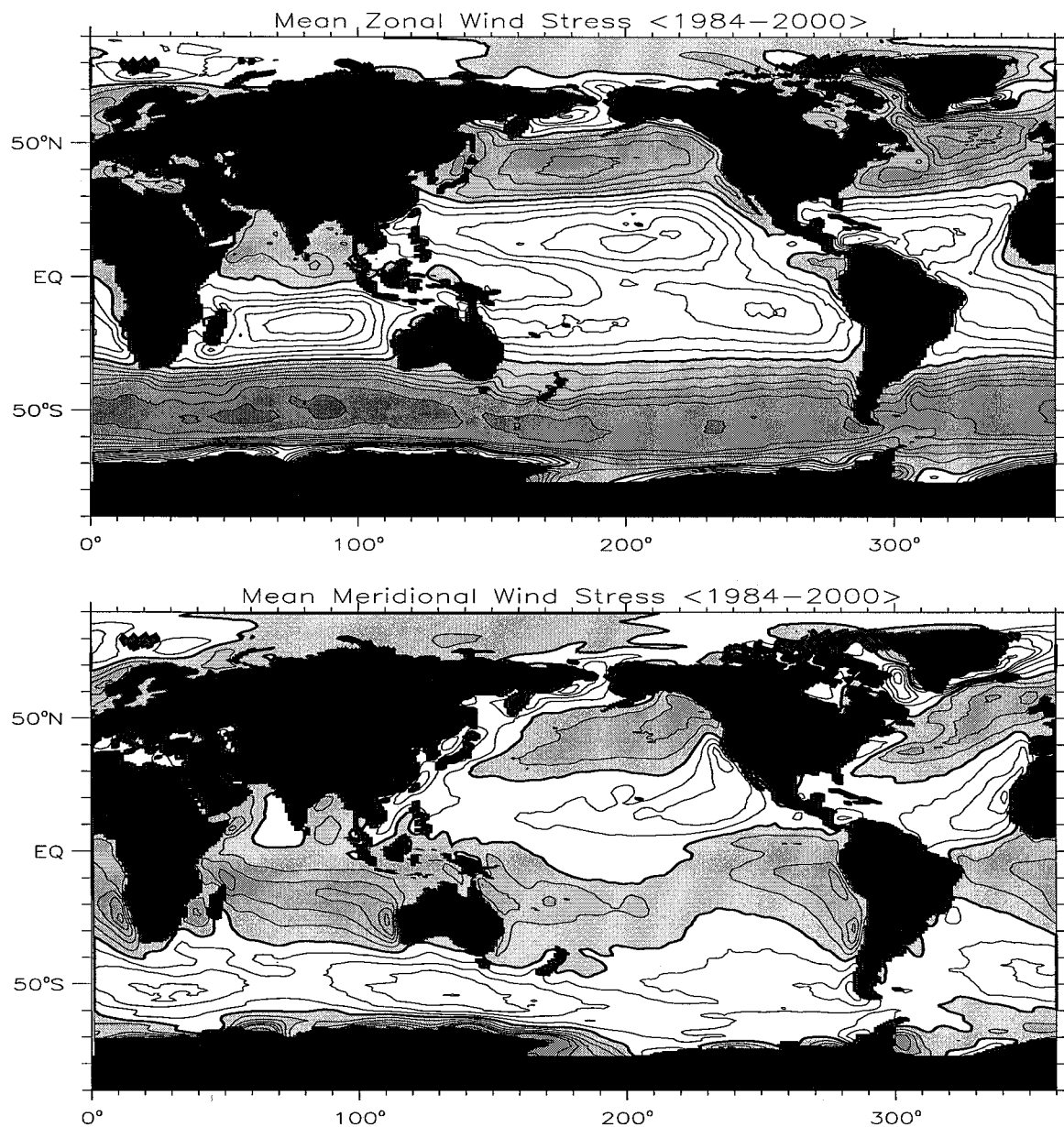
Figure 19: Climatological (1984-2000) mean zonal wind stress (top) and mean meridional wind stress (bottom) in N/m^2. Contour intervals are $\pm(.02,.04,.06,.08,.1,.15,.2,.3)$ with a thick contour at 0. Positive stress values are shaded.
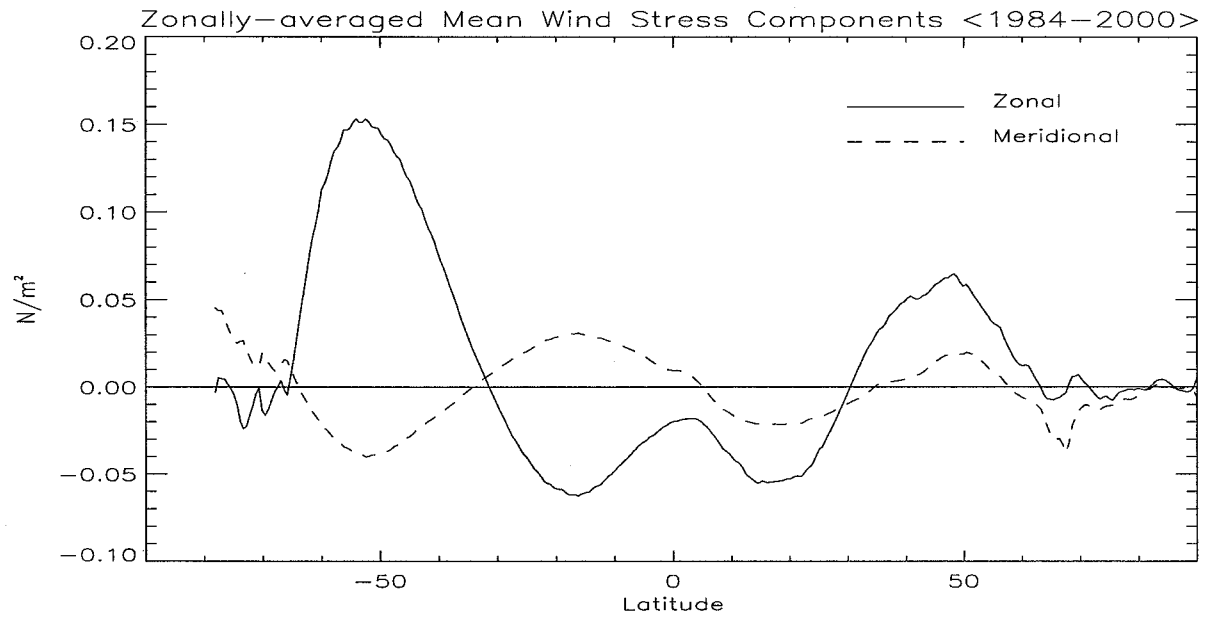
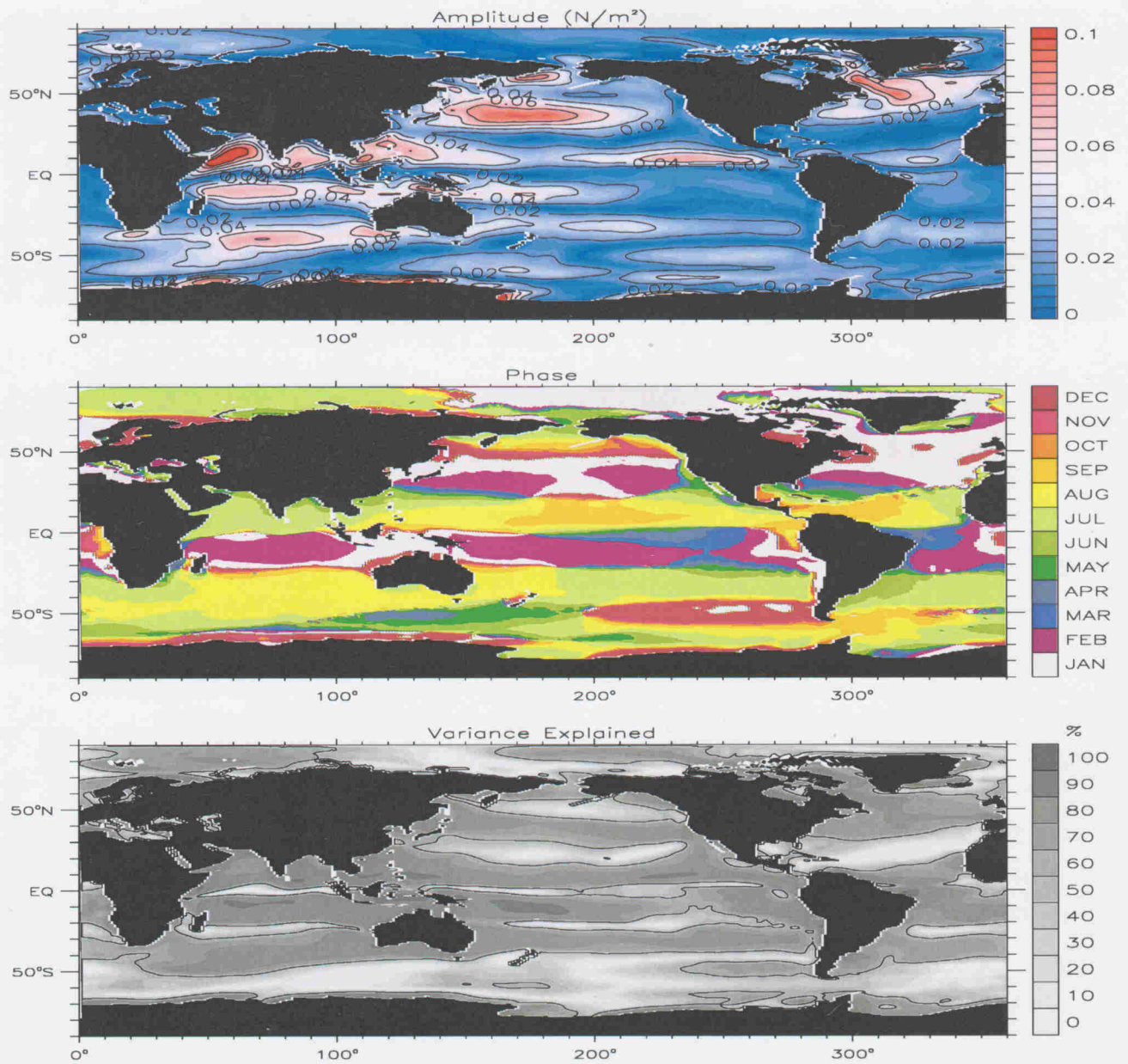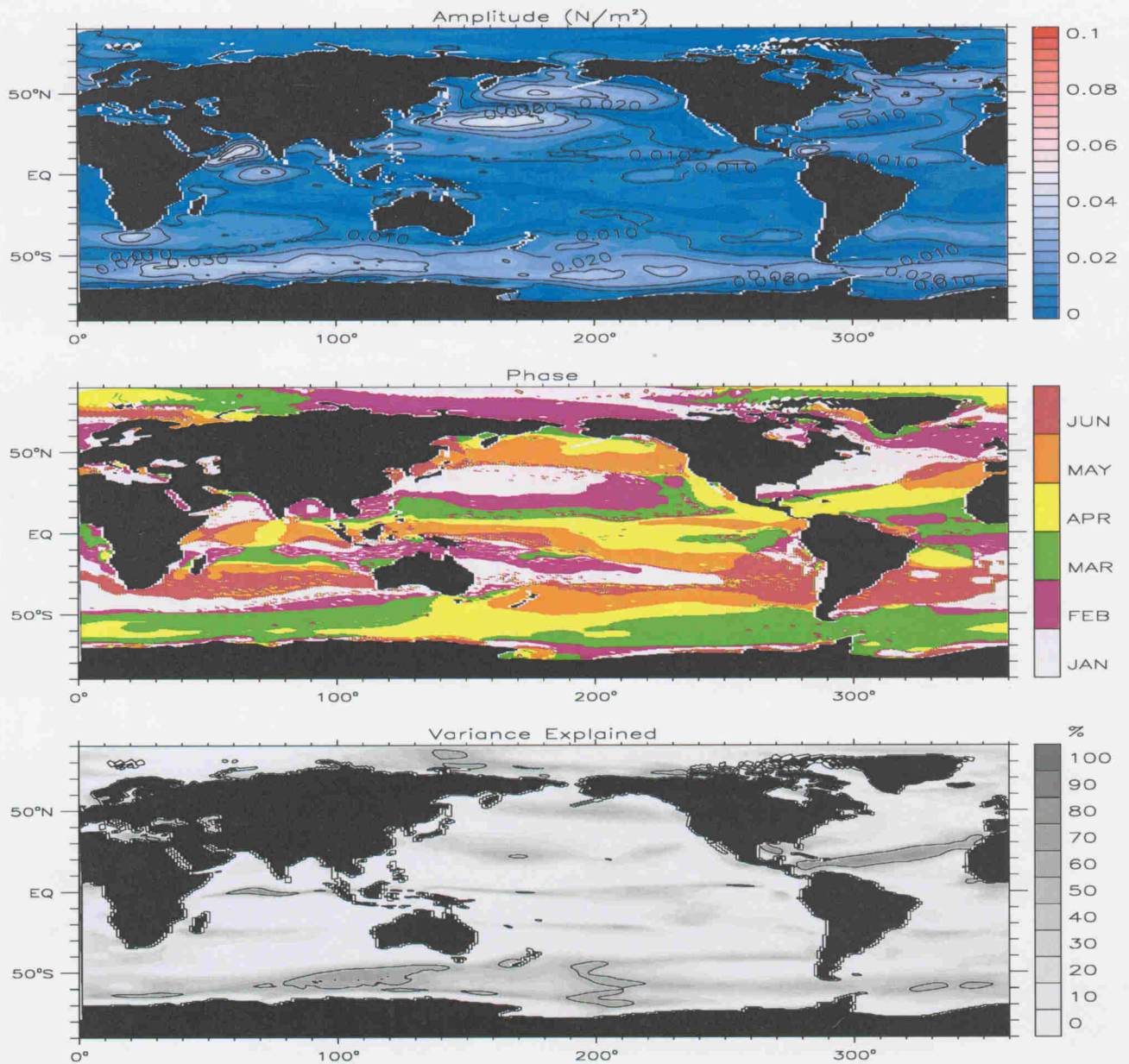Figure 20: Climatological (1984-2000) zonally-averaged zonal and meridional wind stress.
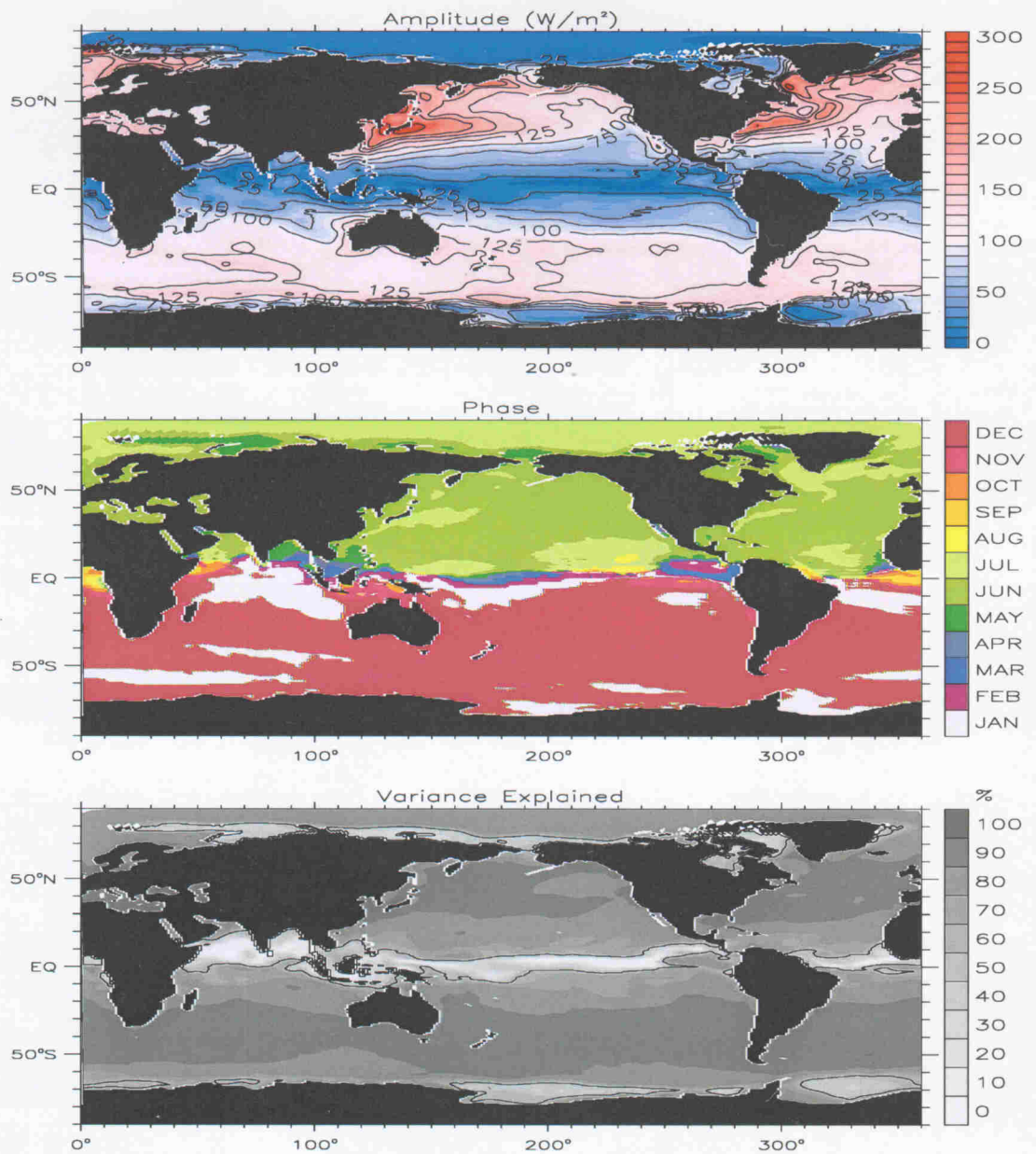
Figure 21: a) Amplitude (top panel) and phase (middle panel) of the first harmonic fit to the climatological (1984-2000) seasonal cycle of net heat flux. The percentage of seasonal variance explained by the sinusoid fit is shaded (bottom panel) with contour level 60% plotted.
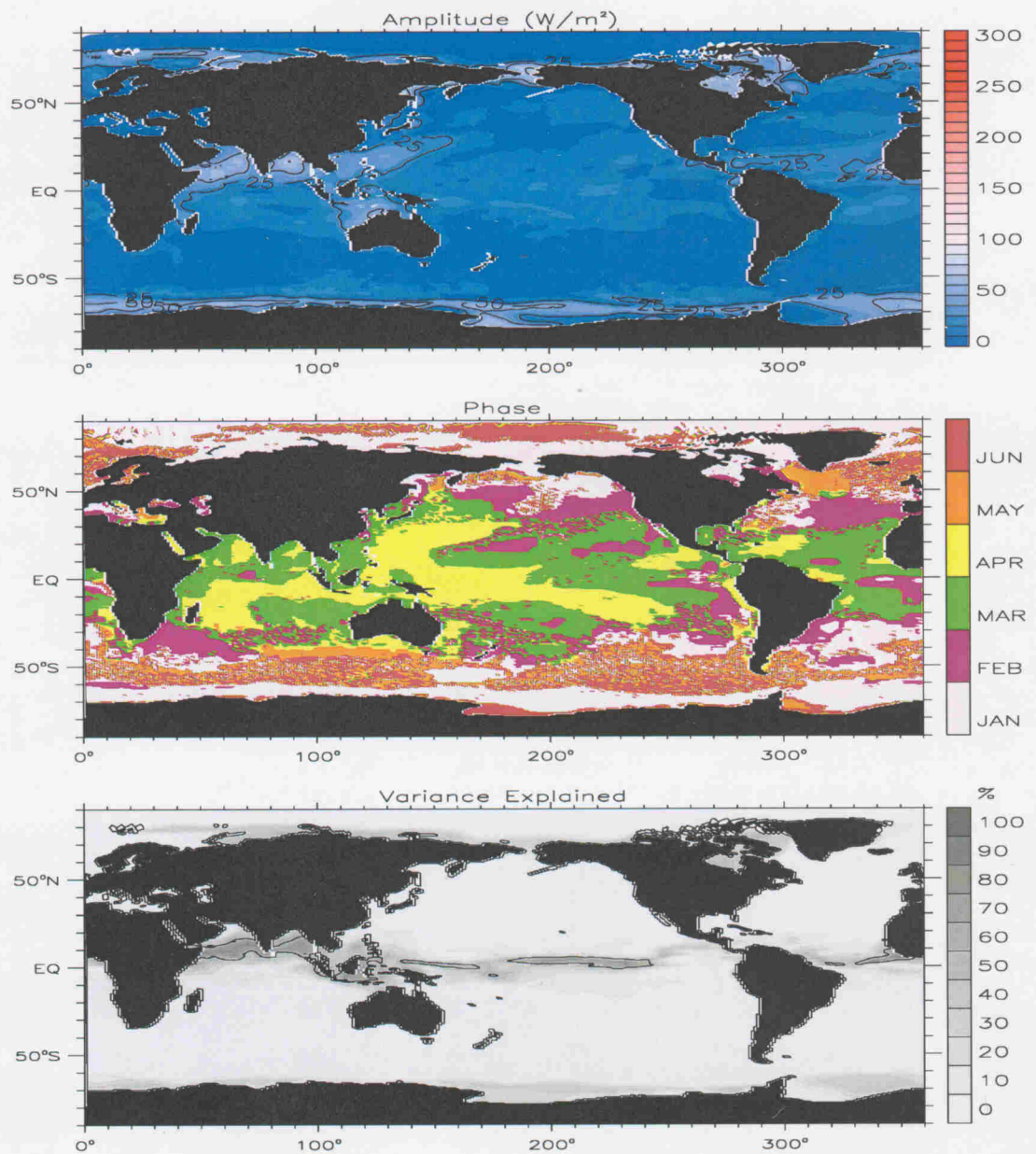
Figure 21: b) Amplitude (top panel) and phase (middle panel) of the second harmonic fit to the climatological (1984-2000) seasonal cycle of net heat flux. The percentage of seasonal variance explained by the sinusoid fit is shaded (bottom panel) with contour level 60% plotted.
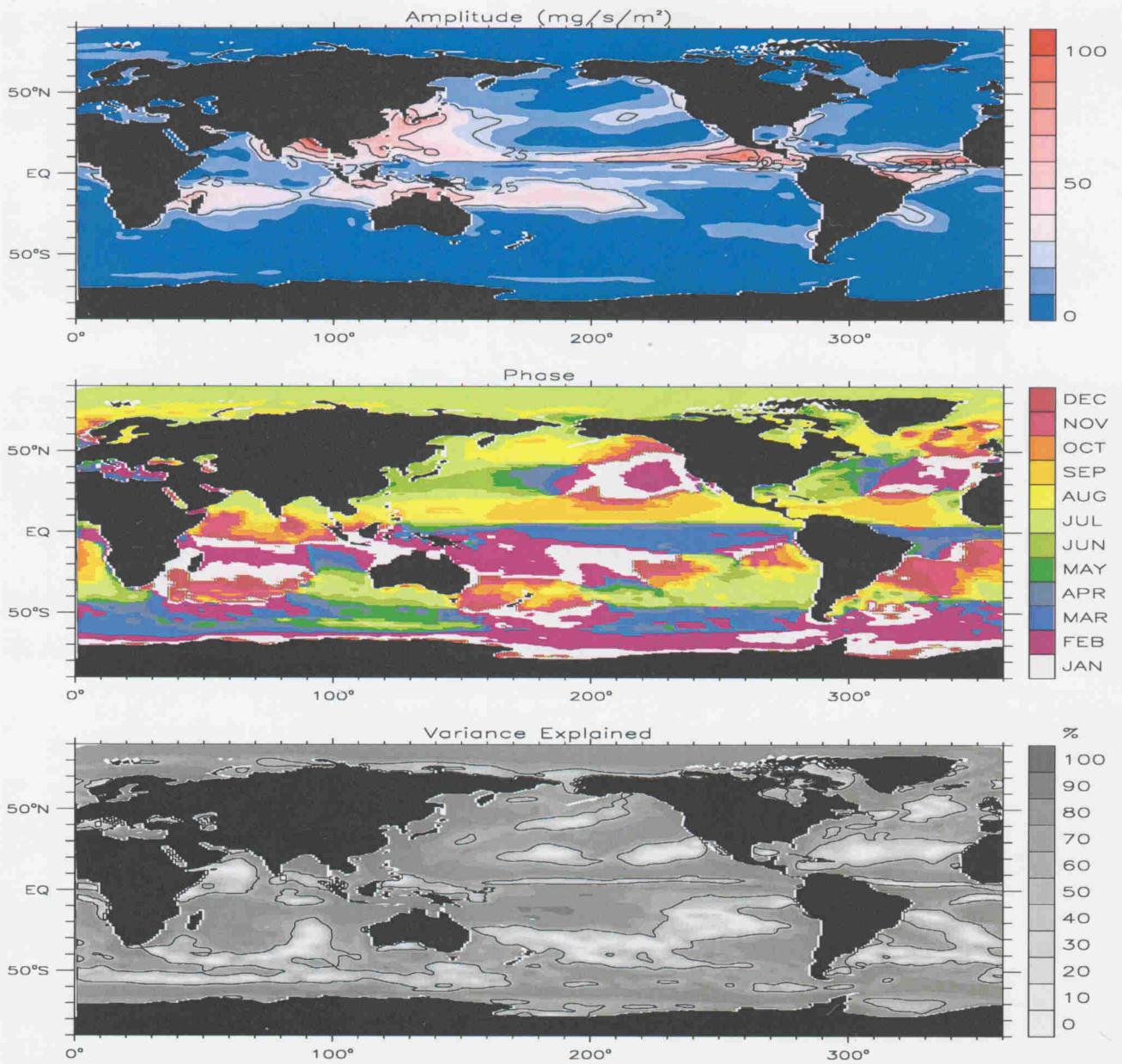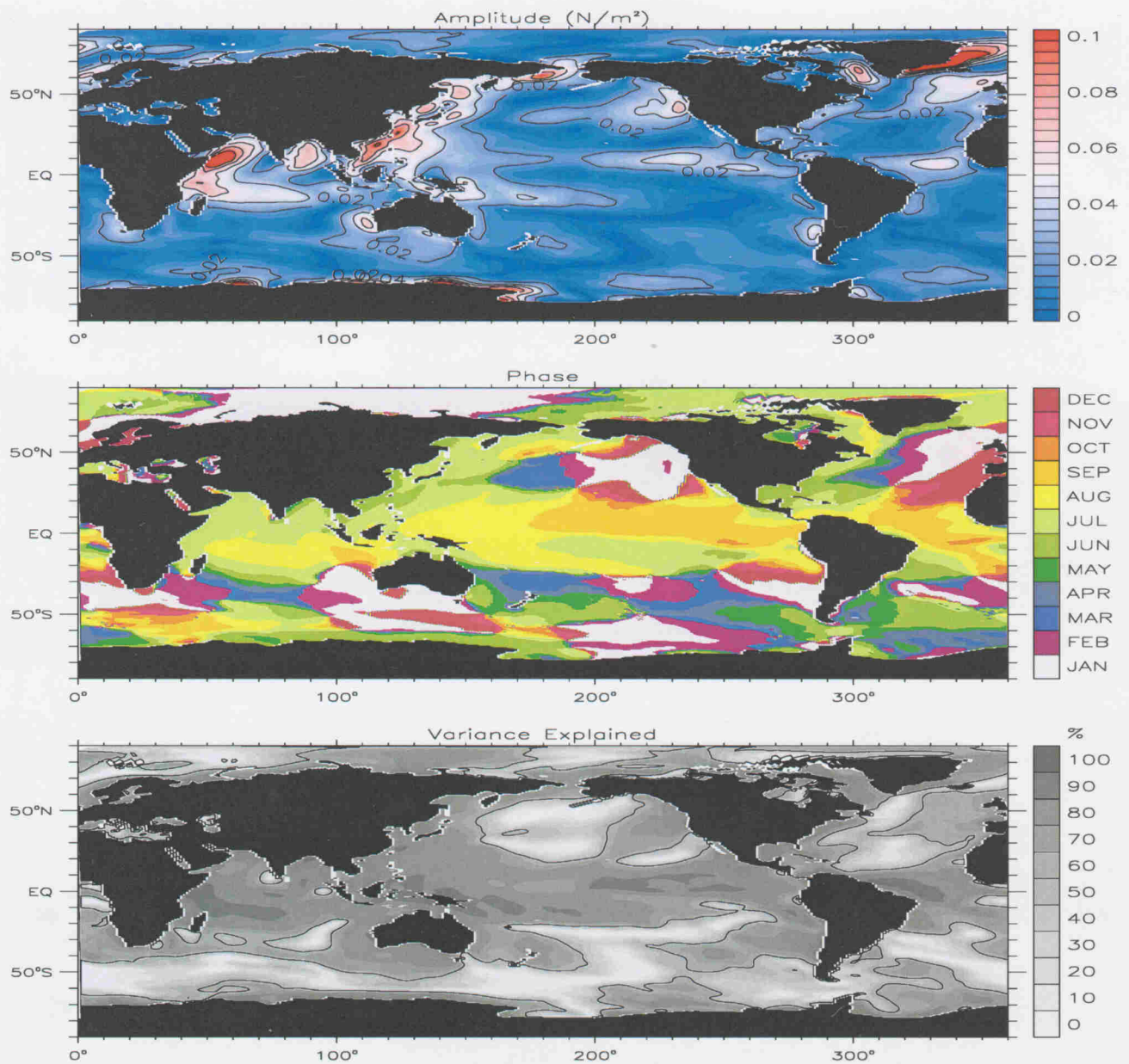
Figure 22: a) Amplitude (top panel) and phase (middle panel) of the first harmonic fit to the climatological (1984-2000) seasonal cycle of net freshwater flux. The percentage of seasonal variance explained by the sinusoid fit is shaded (bottom panel) with contour level 60% plotted.
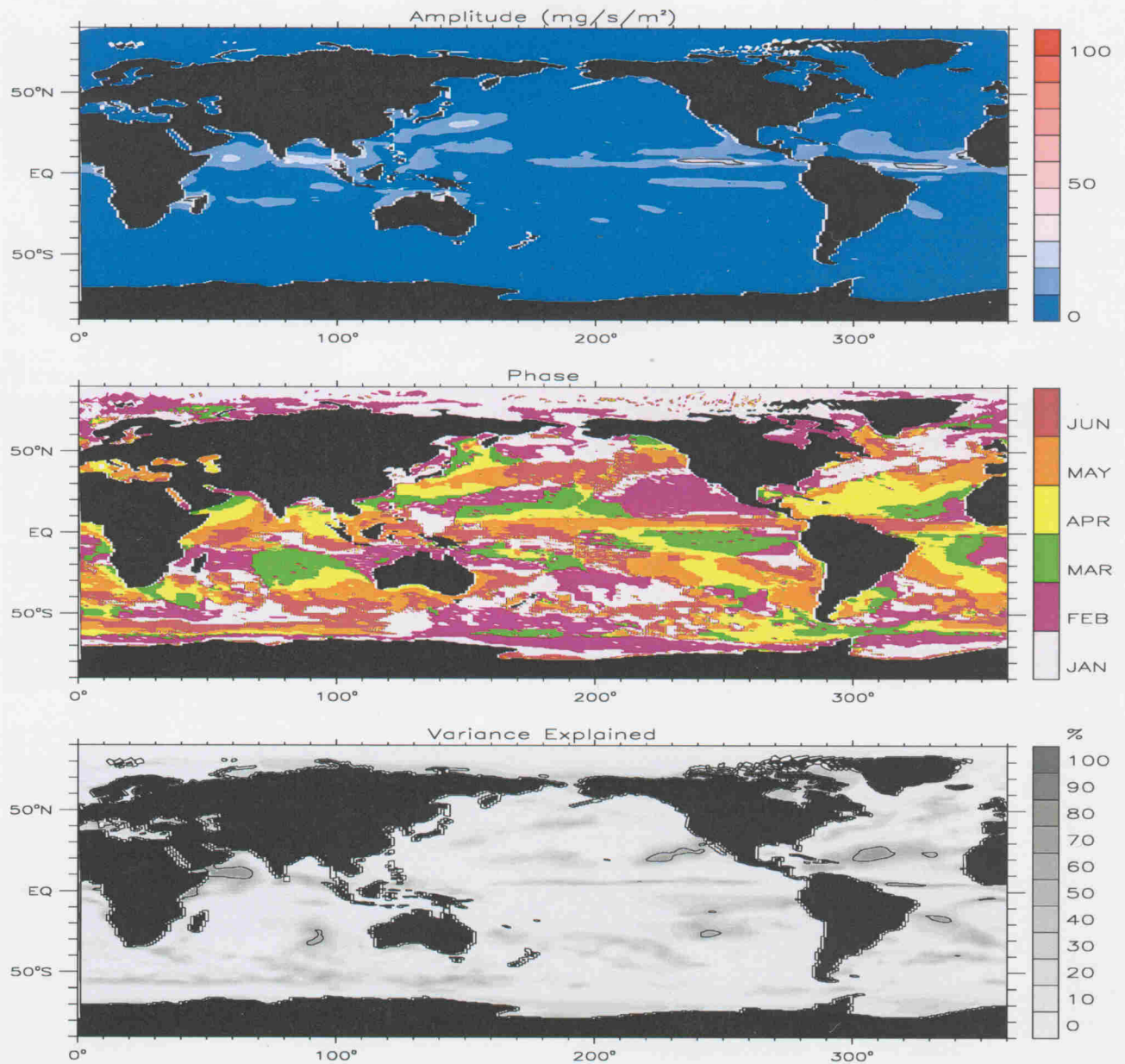
Figure 22: b) Amplitude (top panel) and phase (middle panel) of the second harmonic fit to the climatological (1984-2000) seasonal cycle of net freshwater flux. The percentage of seasonal variance explained by the sinusoid fit is shaded (bottom panel) with contour level 60% plotted.

Figure 23: a) Amplitude (top panel) and phase (middle panel) of the first harmonic fit to the climatological (1984-2000) seasonal cycle of zonal wind stress. The percentage of seasonal variance explained by the sinusoid fit is shaded (bottom panel) with contour level 60% plotted.
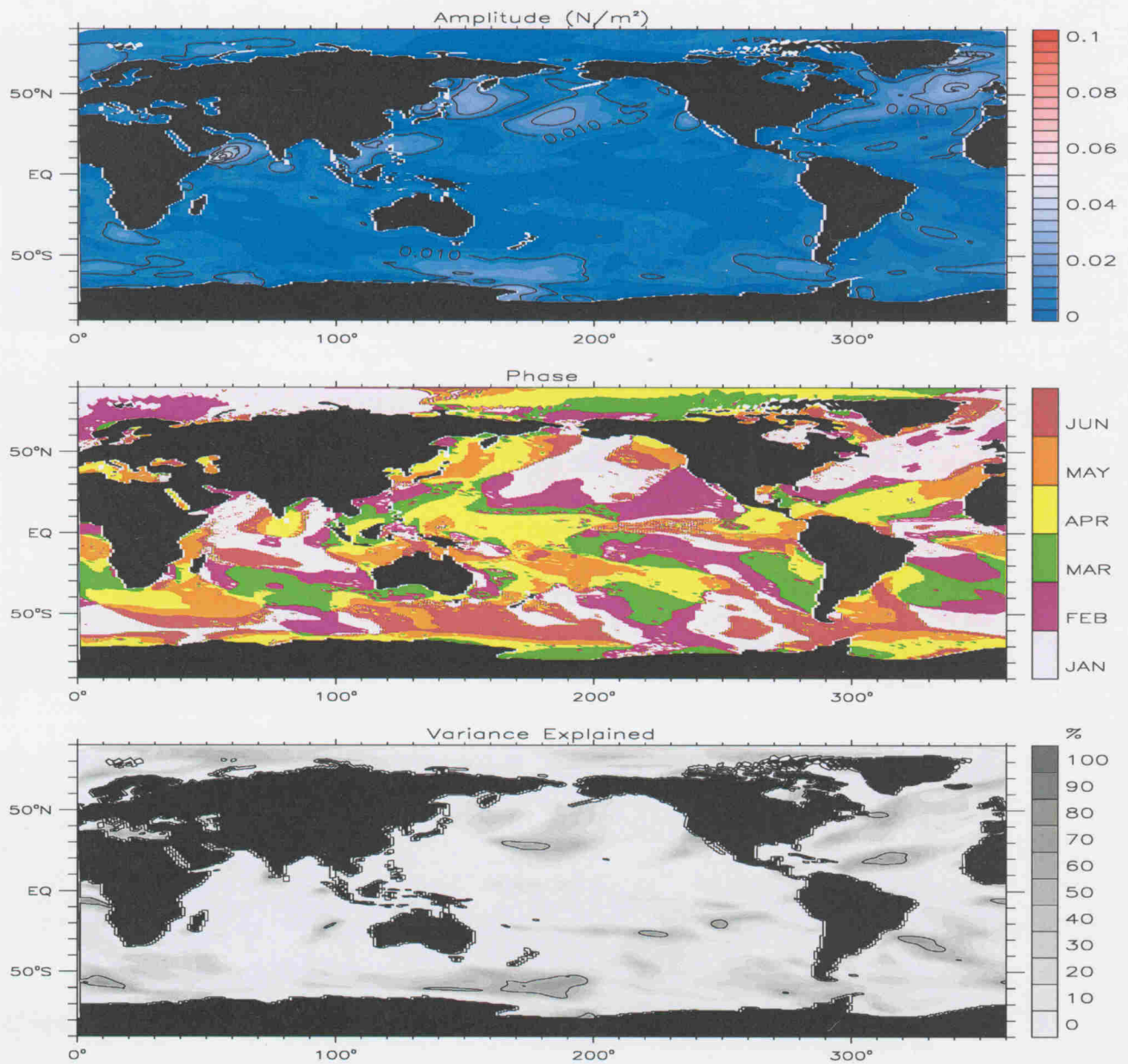
Figure 23: b) Amplitude (top panel) and phase (middle panel) of the second harmonic fit to the climatological (1984-2000) seasonal cycle of zonal wind stress. The percentage of seasonal variance explained by the sinusoid fit is shaded (bottom panel) with contour level 60% plotted.

Figure 24: a) Amplitude (top panel) and phase (middle panel) of the first harmonic fit to the climatological (1984-2000) seasonal cycle of meridional wind stress. The percentage of seasonal variance explained by the sinusoid fit is shaded (bottom panel) with contour level 60% plotted.

93

Figure 24: b) Amplitude (top panel) and phase (middle panel) of the second harmonic fit to the climatological (1984-2000) seasonal cycle of meridional wind stress. The percentage of seasonal variance explained by the sinusoid fit is shaded (bottom panel) with contour level 60% plotted.
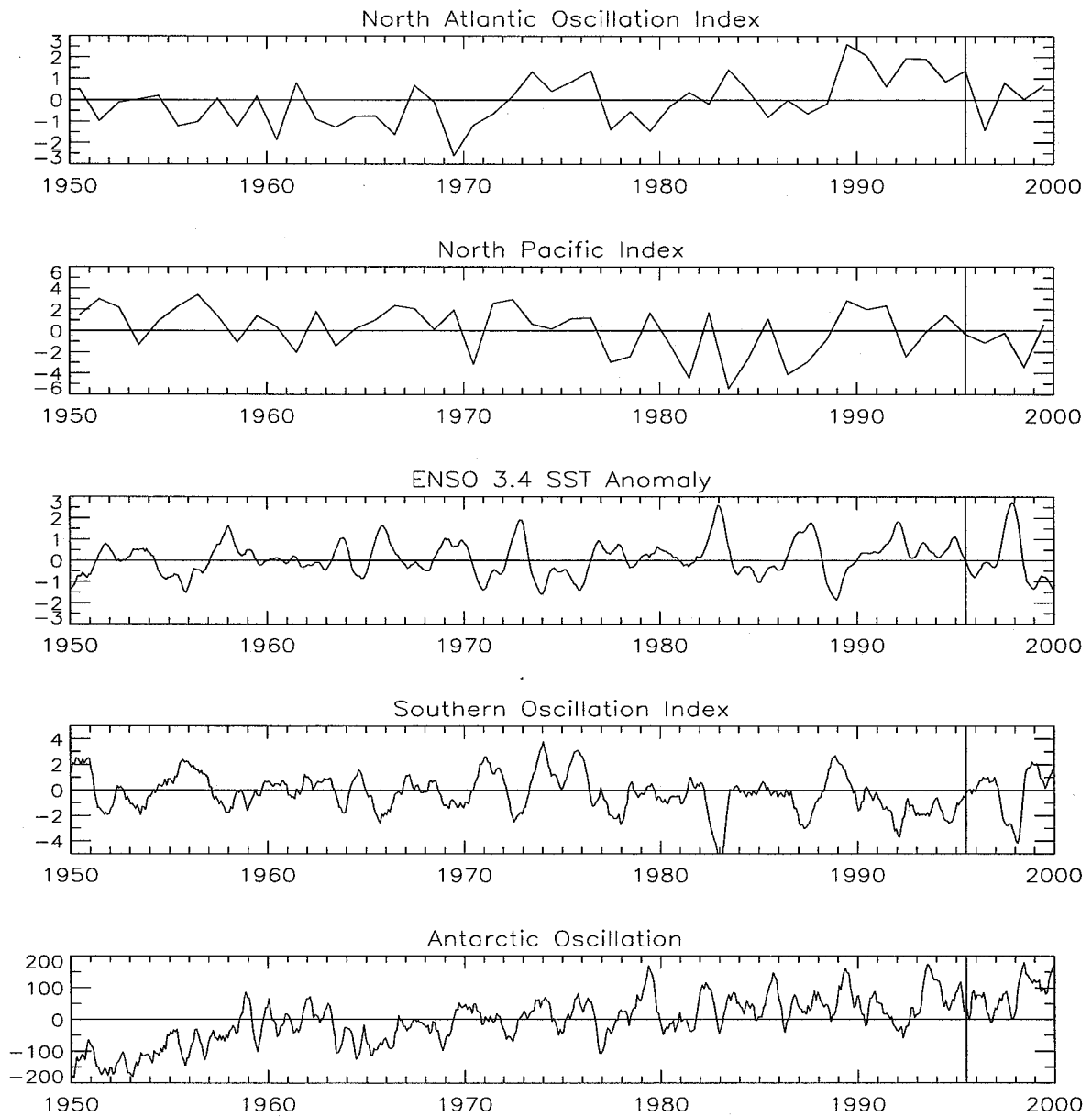
Figure 25: Interannual variability (1950–2000) of large scale climate indices.
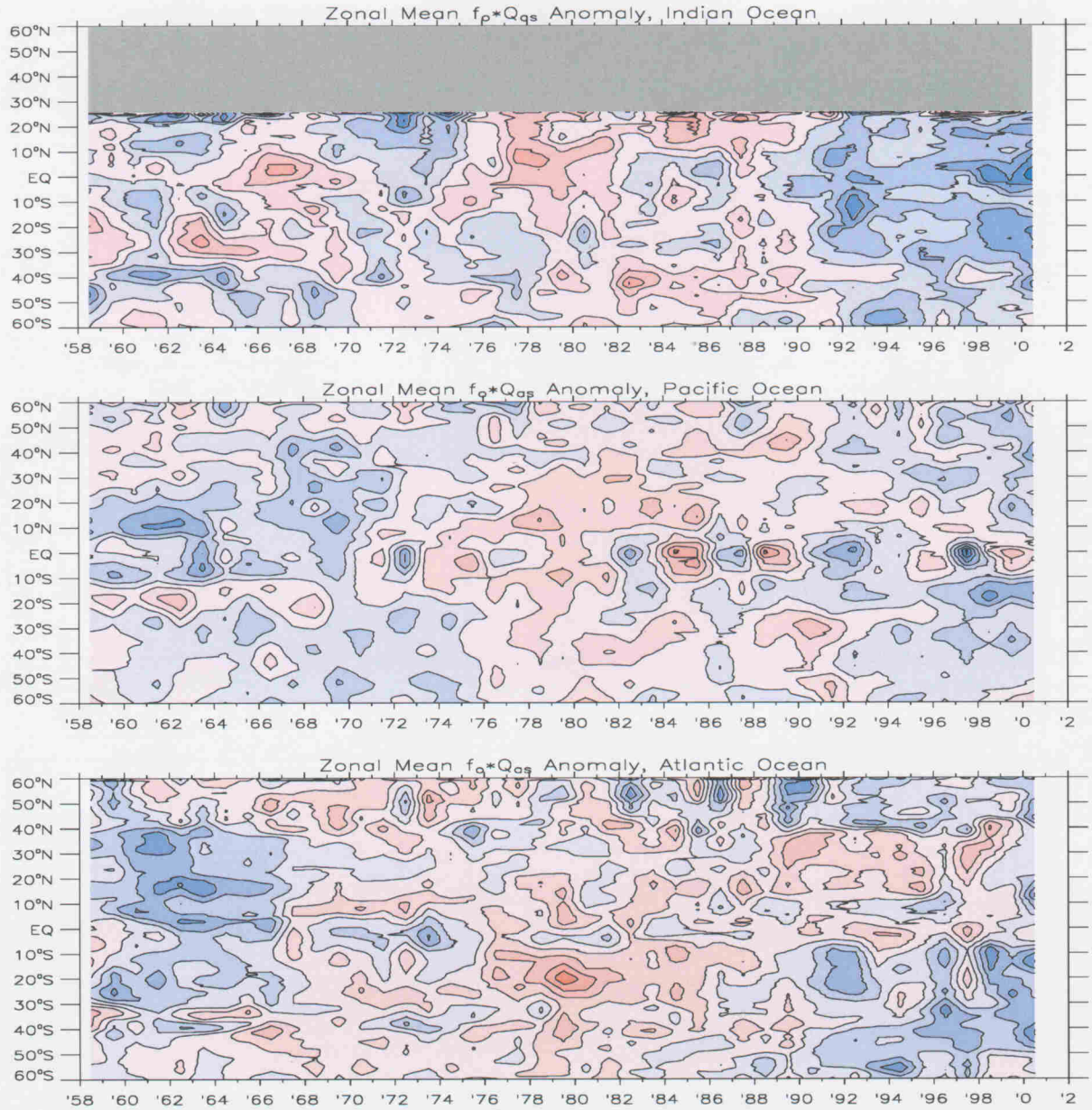
Figure 26: Yearly zonal average net heat flux anomaly for the Indian (top panel), Pacific (middle panel), and Atlantic (bottom panel) basins. The Atlantic basin does not include the Labrador Sea. Contour interval is 5 W/m^2.
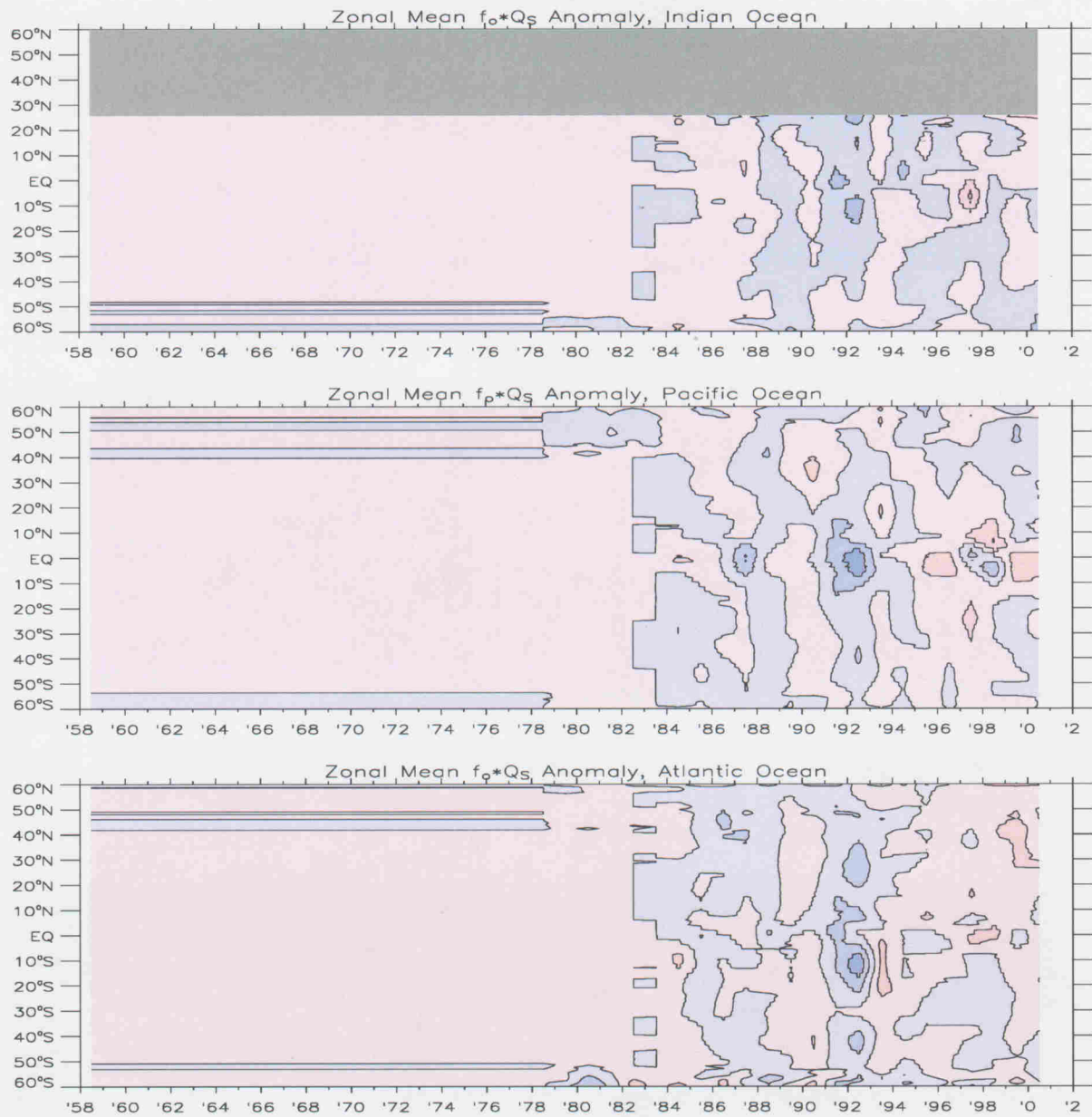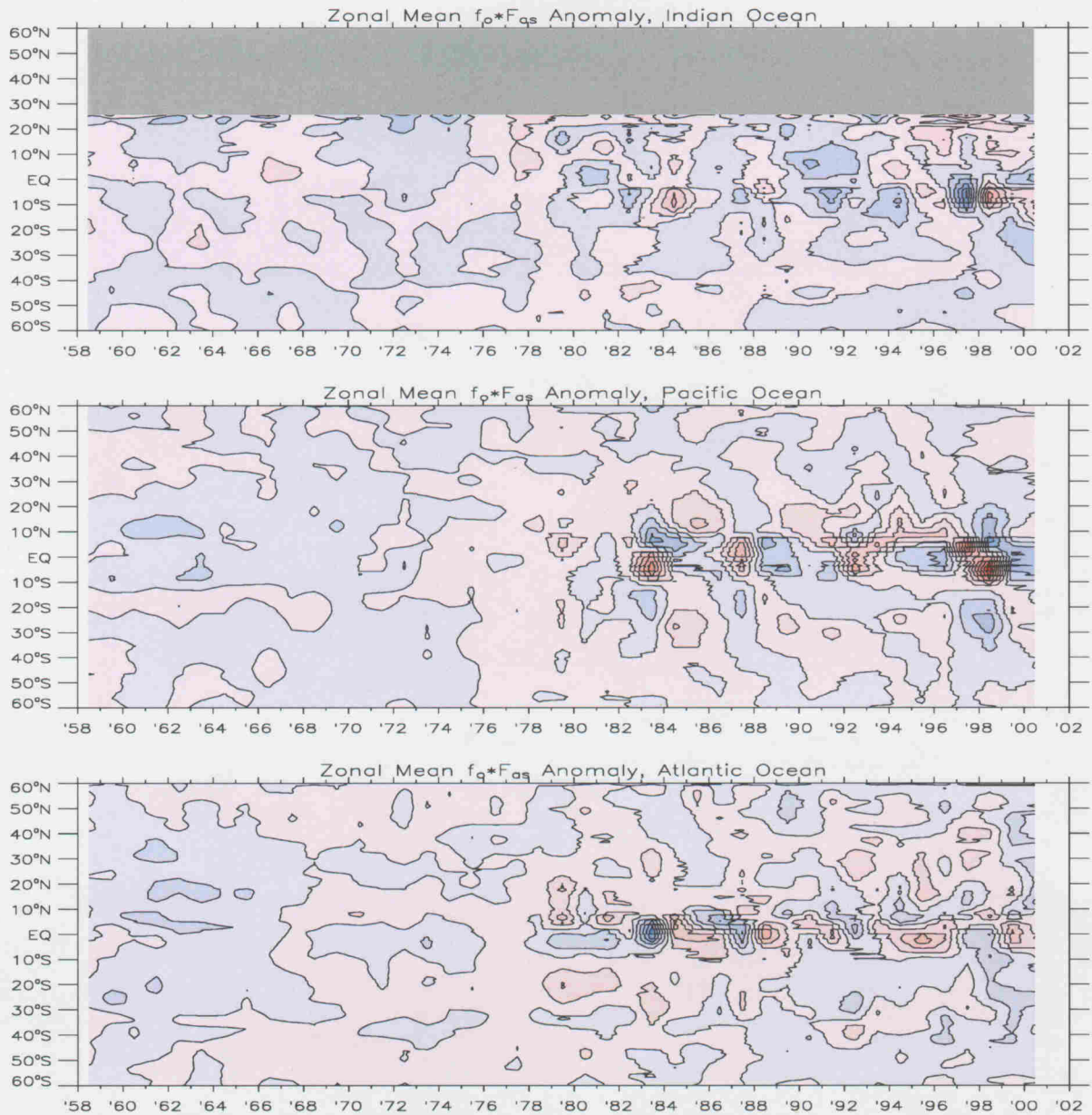
Figure 27: Yearly zonal average net shortwave flux anomaly for the Indian (top panel), Pacific (middle panel), and Atlantic (bottom panel) basins. The Atlantic basin does not include the Labrador Sea. Contour interval is 5 W/m^2.

Figure 28: Yearly zonal average net freshwater flux anomaly for the Indian (top panel), Pacific (middle panel), and Atlantic (bottom panel) basins. The Atlantic basin does not include the Labrador Sea. Contour interval is 4 $mg/m^2/yr$.
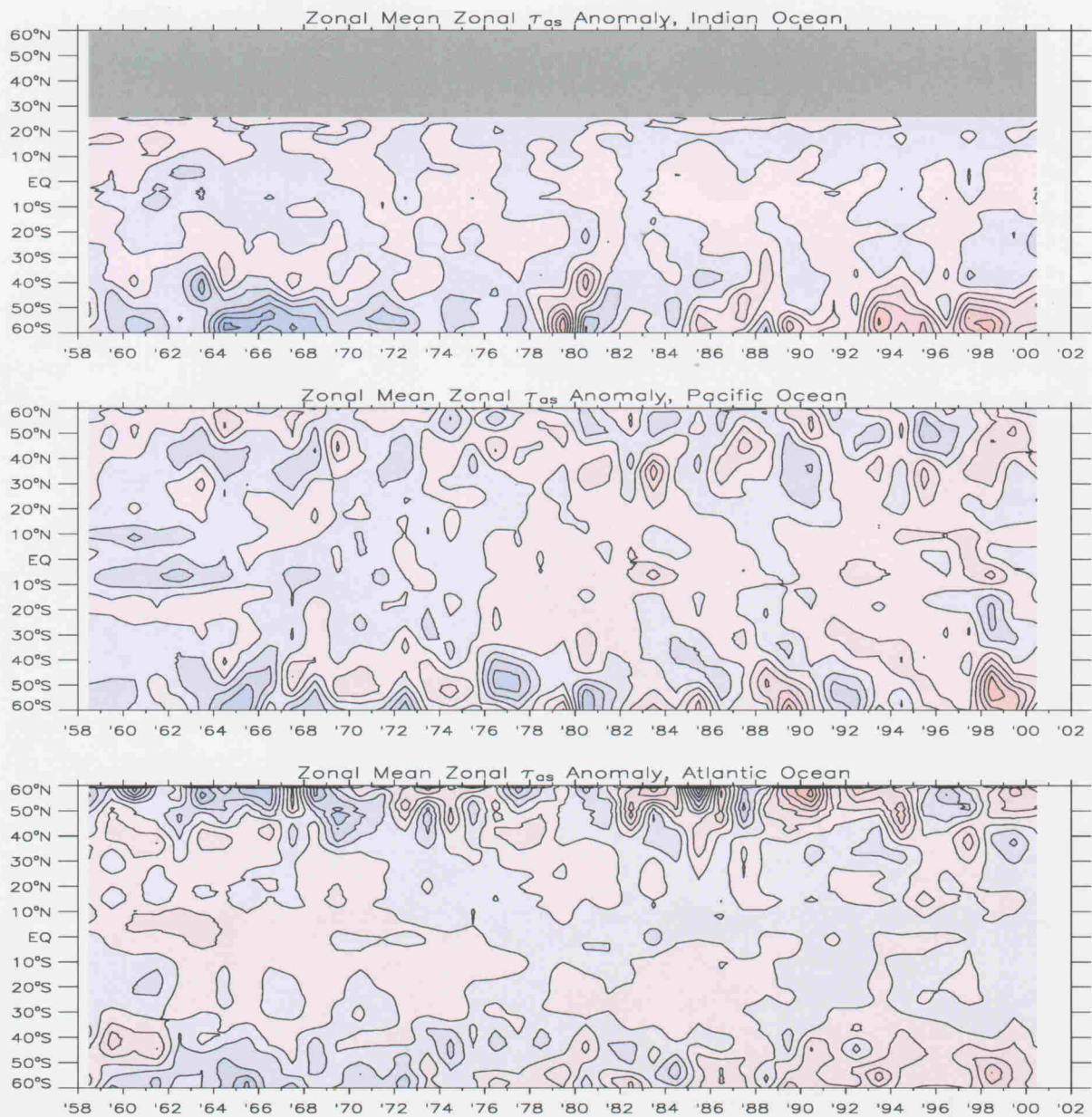
Figure 29: Basin averages of the annual mean zonal air-sea wind stress anomaly from 1958 – 2000 for the Indian (top panel), Pacific (middle panel), and Atlantic (bottom panel) basins. The Atlantic basin does not include the Labrador Sea. Contour interval is .01 N/m^2.
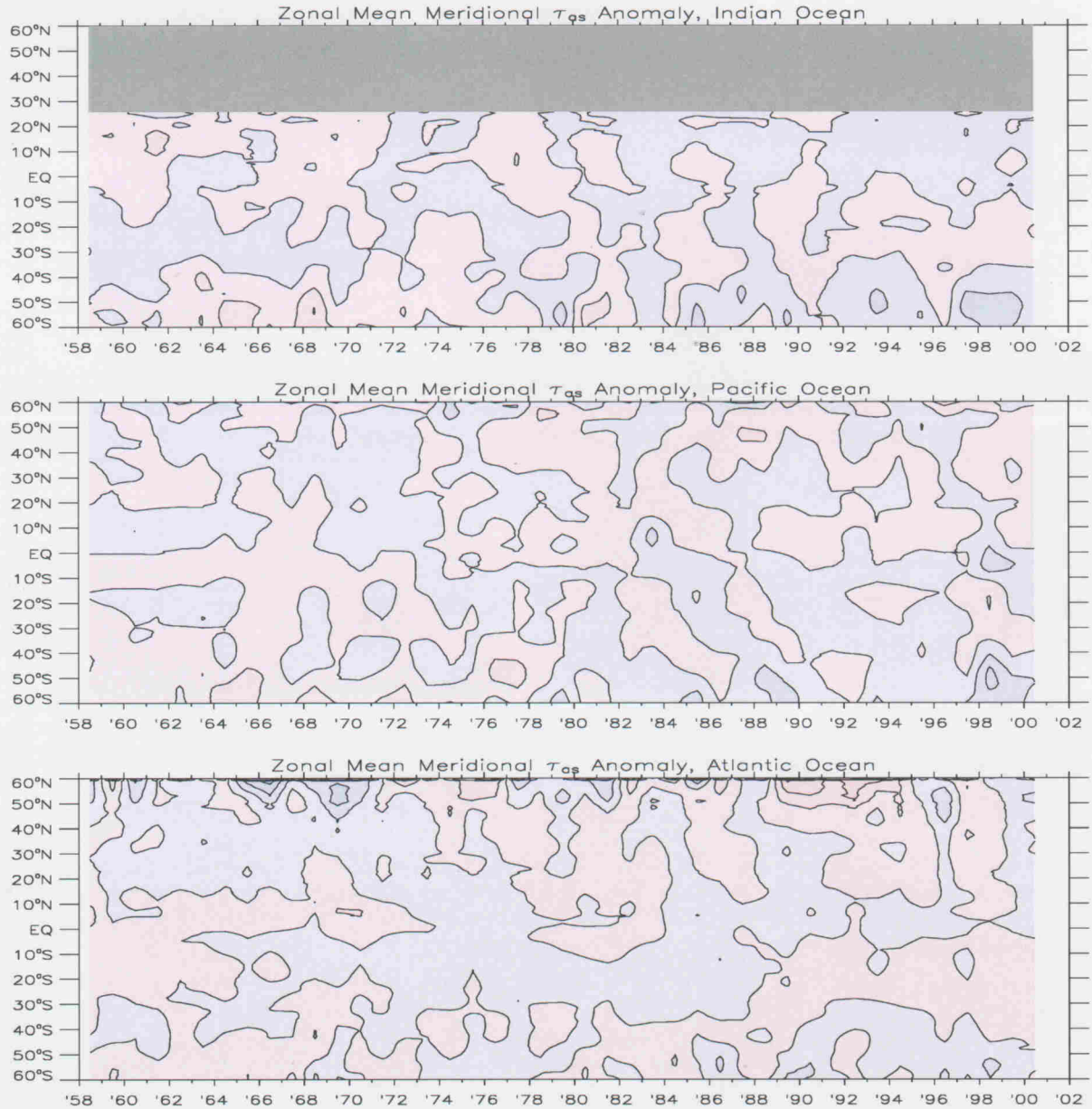
Figure 30: Yearly zonal average meridional air-sea wind stress anomaly for the Indian (top panel), Pacific (middle panel), and Atlantic (bottom panel) basins. The Atlantic basin does not include the Labrador Sea. Contour interval is .01 N/m^2.
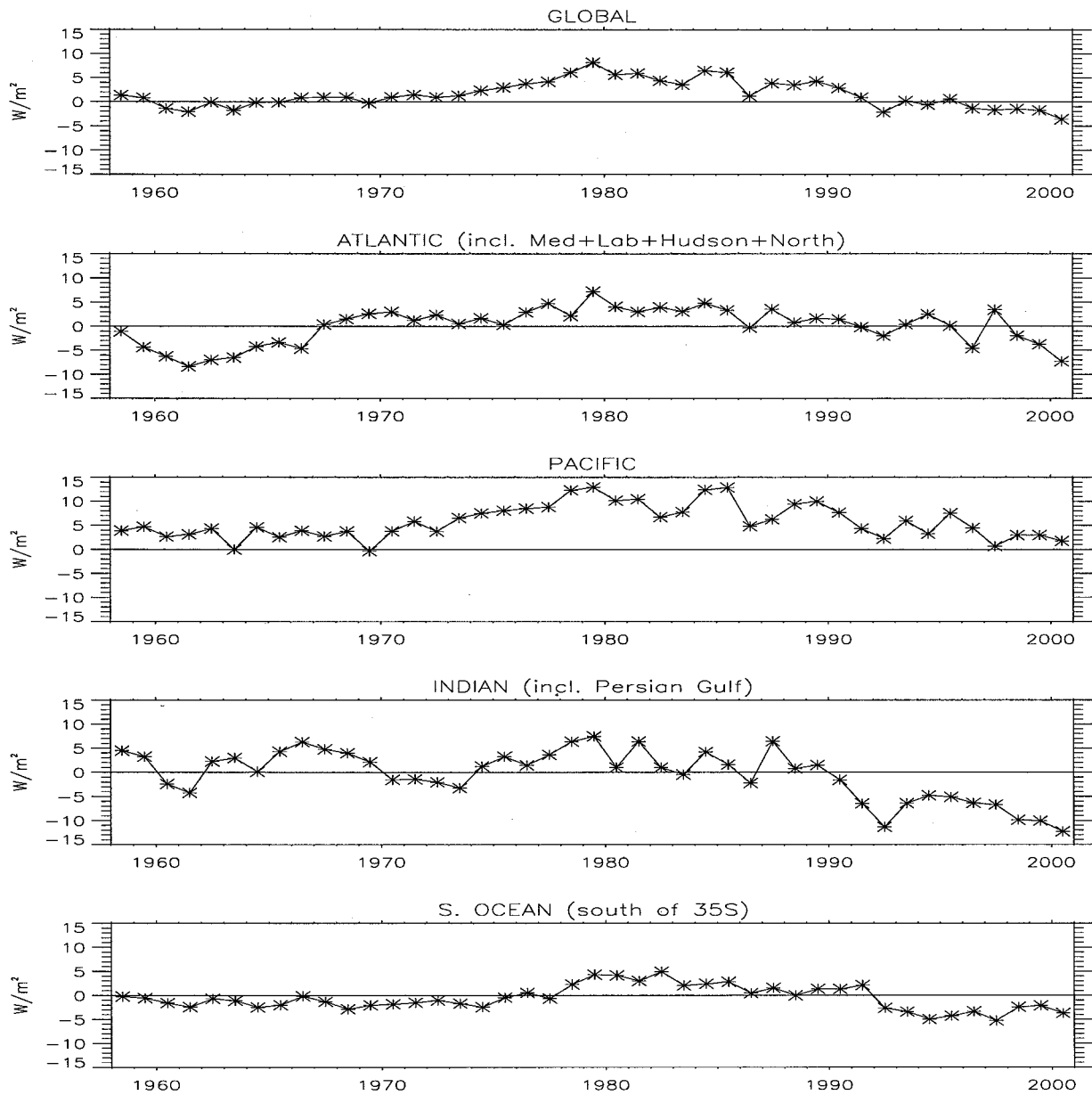
100

Figure 31: Time series of yearly mean net heat flux imbalance as a global mean and by basin. The 43 year mean global heat flux imbalance is 1.6 W/m^2.
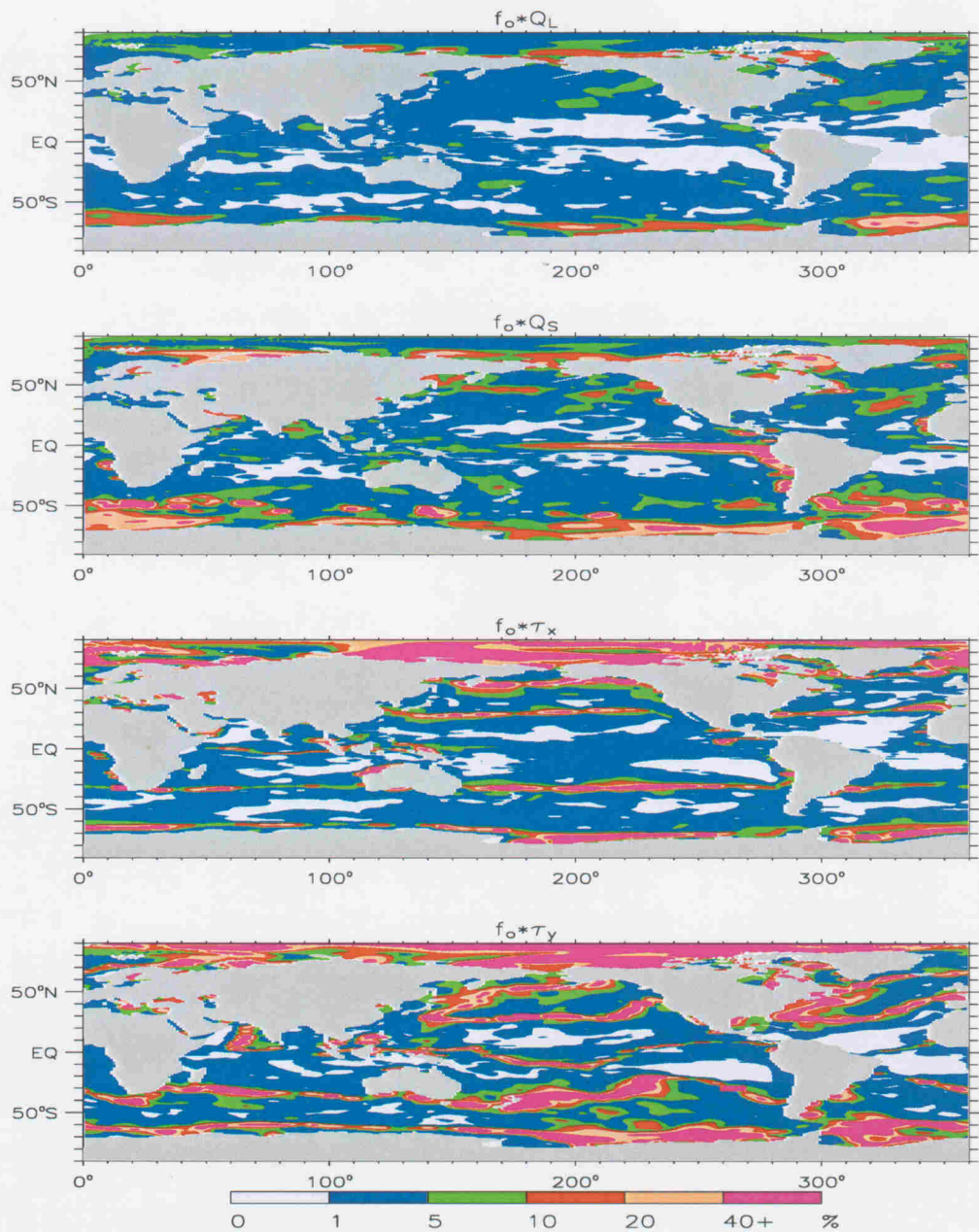
Figure 32: Difference, in percent, of 43-year mean normal year fluxes relative to the 43-year mean of interannually-varying fluxes. Both atmospheric state datasets (normal and interannually-varying) were coupled to the same interannually-varying SST dataset, with interannually-varying ice fraction.
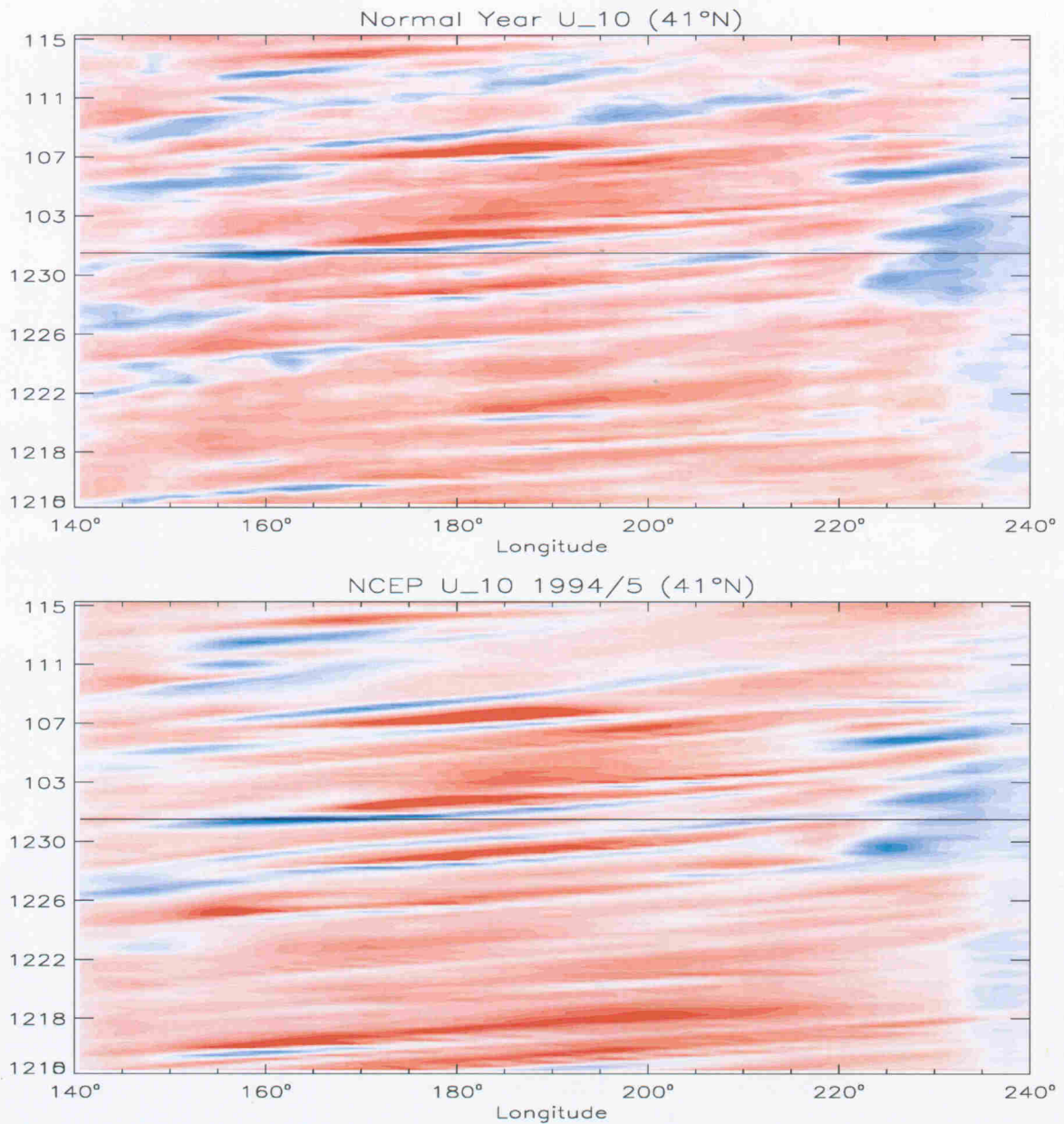
Figure 33: Comparison of the normal year endofyear to beginningofyear transition to that of of the actual 1994 to 1995 transition of NCEP 10m zonal wind speed for a longitude strip in the Northern Pacific. The normal year forcing transitions smoothly across year boundary with phasing that matches that of the chosen phase year.

103

BASIN	RUNOFF (1000 kg/s)	NUMBER OF RIVERS	RIVER RUNOFF	COASTAL RUNOFF
Eurasia - Arctic	138574	17	65216	53%
N. America - Arctic	52441	4	9014	83%
N. America- Atlantic	81114	51	37686	53%
Europe - Atlantic	50593	21	4115	5%
S. America- Atlantic	280381	20	266948	5%
Africa - Atlantic	91538	17	54249	41%
Africa - Indian	15146	9	5202	64%
Asia - Indian	87443	13	72781	16%
Asia - Pacific	153972	26	95286	38%
N. America - Pacific	35587	19	24730	31%
S. America - Pacific	59591	16	5860	90%
Australia - Southern	75000	28	1721	98%
Antarctica - Southern	73000	0	0	100%
Mediterranean	12840	4	5689	56%
Caspian Sea	14301	0	0	100%
Black Sea	9425	3	7996	16%
Persian Gulf/Red Sea	2486	1	1445	42%
Baltic Sea	4669	9	2524	54%
Hudson Bay	20883	17	10027	52%

Table 1: Climatological runoff from 19 continental drainage basins, including the guaged flow from a number of major rivers, and the percentage of the total attributed to coastal, or other rivers. The total runoff is $1.26x10^9 kg/s = 1.26 Sv$.

	CORRECTIONS			
	NONE	WIND	HUMIDITY	ALL
$f_o\,Q_S$	173	173	173	165
$f_o\,Q_L$	-52	-52	-52	-52
$f_o\,Q_E$	-76	-84	-89	-97
$f_o\,Q_H$	-13	-14	-13	-14
$f_o(Q_{as} - Q_P)$	31	23	18	1
$f_o\,E$	-30.5	-33.4	-35.6	-39.0
$f_o\,P$	30.4	30.4	30.4	35.4
R	3.5	3.5	3.5	3.5
$f_o\,F_{as} + R$	3.4	0.5	-1.7	-0.1

Table 2: Global mean air-sea fluxes 1984–2000 and continental runoff. Heat fluxes are in W/m^2, and freshwater fluxes are in $mg/m^2/s$ ($0.0864mm/day \approx 31mm/year$). If instead of model area, the true ocean area of $3.523 \times 10^8 km^2$ is used to divide the sum of all runoff in Table 1, the Runoff becomes, R = 3.574 $mg/m^2/s$.